CHARGE COMPENSATION MECHANISMS AND TWINNING IN DOPED SnO_2-BASED CERAMICS

Sara Tominc

Doctoral Dissertation
Jožef Stefan International Postgraduate School
Ljubljana, Slovenia

Supervisor: Prof. Dr. Aleksander Rečnik, Jožef Stefan International Postgraduate School and Jožef Stefan Institute, Ljubljana, Slovenia
Co-Supervisor: Asst. Prof. Dr. Nina Daneu, Jožef Stefan International Postgraduate School and Jožef Stefan Institute, Ljubljana, Slovenia

Evaluation Board:
Prof. Dr. Slavko Bernik, Chair, Jožef Stefan International Postgraduate School and Jožef Stefan Institute, Ljubljana, Slovenia
Doc. Dr. Srečo Davor Škapin, Member, Jožef Stefan International Postgraduate School and Jožef Stefan Institute, Ljubljana, Slovenia
Dr. Goran Branković, Member, Institute for Multidisciplinary Research (IMSI), University of Belgrade, Belgrade, Serbia

MEDNARODNA PODIPLOMSKA ŠOLA JOŽEFA STEFANA
JOŽEF STEFAN INTERNATIONAL POSTGRADUATE SCHOOL

Sara Tominc

CHARGE COMPENSATION MECHANISMS AND TWINNING IN DOPED SnO_2-BASED CERAMICS

Doctoral Dissertation

MEHANIZMI KOMPENZACIJE NABOJA IN DVOJČENJE V DOPIRANI KERAMIKI NA OSNOVI SnO_2

Doktorska disertacija

Supervisor: Prof. Dr. Aleksander Rečnik

Co-Supervisor: Asst. Prof. Dr. Nina Daneu

Ljubljana, Slovenia, July 2021

"Nothing in life is to be feared, it is only to be understood. Now is the time to understand more, so that we may fear less." (Marie Curie)

To my Family.

Acknowledgments

"I would maintain that thanks
are the highest form of thought,
and that gratitude is happiness
doubled by wonder."

-G.K. CHESTERON-

First, I would like to thank my supervisor **Prof. Aleksander Rečnik** for a kind acceptance to the world of science and for giving me the opportunity to work with him. Thanks for all the help, support, ideas and discussions during my doctoral study. Thank you for introducing the "world of atoms" to me, for spending hours with me on the microscope, and especially thanks for all your patience and the knowledge you shared with me. I am proud to have a mentor like you.

At the same time, I would like to thank my co-supervisor, **Asst. Prof. Nina Daneu** for all the excellent tips, ideas and guidance at work. Thank you for joining me in the national project no. J1-9177 entitled: "Nanostructured investigations of diffusion-controlled processes between topotaxial phase transformations in rutile-corundum type." It was my pleasure to work with you.

I would like to thank Prof. Slavko Bernik for all the warm tips and explanations in the field of ceramics and varistors, Prof. Goran Dražić for twin boundary analysis on transmission electron microscope (ARM200F), Dr. Zoran Samardžija for an excellent EBSD study of twins in SnO_2, Edi Kranjc (KI, Slovenia) for X-ray powder diffraction measurements, Dr. Matjaž Mazaj (KI, Slovenia) for Rietveld analysis, and Dr. Matejka Podlogar for all the assistance in the preparation of ceramics samples and the characterization of varistor properties. A great thank you also goes to Medeja Gec, a great teacher of the SEM and TEM specimen preparation. You proved that nothing is impossible to prepare. I would like to thank Maja Koblar for the pleasant and instructional education on the scanning electron microscope and her generous help in dealing with any type of problems. Tina Radošević, thank you for all your help in the laboratory work. I would also like to thank Asst. Prof. Matjaž Spreitzer for his friendly advice on dielectric measurements, Silvo Zupančič for recording densification characteristics on heating-stage microscope and David Fabjan for dielectric measurements (all from the Advanced Materials Department (K9), IJS).

I sincerely thank the entire Department for Nanostructured Materials (K7), the members of the Evaluation Board for their effort in the evaluation of this doctoral thesis, and the Slovenian Research Agency (ARRS) for financing my doctoral study under Project No. J1-6742, Program P2-0084 and Contract No. 0106/37484.

Sandra, Nadežda and Vanja (later also Bojan), thanks for the pleasant atmosphere in our office. Especially thanks to **Vanja** for all the hours we spent together at lunch and your sincere friendship.

And finally, the greatest thank you goes to my family: **Mom, Dad, Mark** ... Thank you for all the support during my study, the encouraging words and the unwavering trust in me.
Thank you, **Rene**, for your heartfelt and sincere love, and especially thanks to my little boys **Lukas** and **Teo** who gave my life a new meaning. You mean the world to me.

And at the end, I sincerely thank my best friends: **Maja**, **Tina, Sara** and **Tadeja**. Thank you for all our adventures, for always standing by my side and believing in me. Love you!

Abstract

Tin (IV) oxide, SnO_2 (cassiterite), is an *n*-type semiconductor with an advantageous combination of chemical, electric and optical properties that make it suitable for a range of applications, from solid-state gas sensors, transparent conductive coatings, oxidation catalysts and varistors. In varistor ceramics, grain growth studies are of particular interest, because understanding the growth process can be beneficially used for controlling the microstructure development and for tailoring grain size-dependent electrical properties, such as the threshold voltage. Unlike in ZnO varistor ceramics, where the role of dopants on microstructure evolution is well understood, these effects have not yet been fully examined in SnO_2 ceramics.

In my doctoral thesis, I focused on the synthesis of various compositions of two varistor systems: SnO_2-CoO-Nb_2O_5 and SnO_2-CoO-Ta_2O_5, and suggested ionic charge compensation mechanism for both systems. In CoO–Nb_2O_5–doped SnO_2 ceramics, I have shown that Nb^{5+} ions compensate for Co^{2+} and Sn^{2+} ions according to the following charge compensation mechanism:

$$6\ \mathrm{Sn(IV)}^{\times}_{\mathrm{Sn\,(IV)}} \rightleftharpoons\ \mathrm{Sn(II)}^{''}_{\mathrm{Sn\,(IV)}} +\ \mathrm{Co(II)}^{''}_{\mathrm{Sn\,(IV)}} + 4\ \mathrm{Nb(V)}^{\cdot}_{\mathrm{Sn\,(IV)}}$$

Important distinction between Ta_2O_5 and Nb_2O_5 addition is considerably lower solid solubility of Ta in SnO_2 and two times higher Co:Ta ratio, suggesting that Co^{2+} is the only divalent cation that compensates the charge of Ta^{5+} on Sn–sites obeying the following compensation mechanism:

$$3\ \mathrm{Sn(IV)}^{\times}_{\mathrm{Sn\,(IV)}} \rightleftharpoons\ \mathrm{Co(II)}^{''}_{\mathrm{Sn\,(IV)}} + 2\ \mathrm{Ta(V)}^{\cdot}_{\mathrm{Sn\,(IV)}}.$$

The second part of my doctoral thesis is focused on twinning of SnO_2. This otherwise quite common phenomenon in SnO_2 has not yet been clarified, while in structurally related rutile TiO_2, the mechanism of twinning is well understood. I tried to determine how specific dopants influence the formation of twin boundaries, and in turn, how they affect SnO_2 grain growth, microstructure development, and the electrical properties of the material. I have shown that twinning in SnO_2 is not chemically induced, but it is probably a result of topotaxial recrystallization process in the initial stages of SnO_2 grain growth.

Povzetek

Kositrov (IV) oksid, SnO_2 (kasiterit), je polprevodnik tipa n z ugodno kombinacijo kemičnih, električnih in optičnih lastnosti, zaradi česar je primeren za različne aplikacije, od trdnih plinskih senzorjev, transparentnih prevodnih prevlek, v procesih oksidacije katalizatorjev kot tudi za varistorje. V varistorski keramiki ima posebno vlogo študija rasti zrn, saj je razumevanje procesa rasti lahko koristno za nadzor razvoja mikrostrukture, kot tudi za optimizacijo električnih lastnosti, ki zavisijo od velikosti zrn, kot je prebojna napetost. Za razliko od ZnO varistorske keramike, kjer je vloga dopantov v razvoju mikrostrukture dobro raziskana, ti učinki v SnO_2 keramiki še niso povsem jasni.

V svojem doktorskem delu sem se osredotočila na sintezo različnih končnih sestav dveh varistorskih sistemov, SnO_2-CoO-Nb_2O_5 in SnO_2-CoO-Ta_2O_5, ter predlagala dva mehanizma kompenzacije naboja za oba sistema. V CoO-Nb_2O_5-dopirani SnO_2 keramiki smo pokazali, da Nb^{5+} ioni kompenzirajo Co^{2+} in Sn^{2+} ione po naslednjem mehanizmu:

$$6\ \mathrm{Sn(IV)}^{\times}_{\mathrm{Sn\,(IV)}} \rightleftharpoons\ \mathrm{Sn(II)}^{''}_{\mathrm{Sn\,(IV)}} +\ \mathrm{Co(II)}^{''}_{\mathrm{Sn\,(IV)}} + 4\ \mathrm{Nb(V)}^{\cdot}_{\mathrm{Sn\,(IV)}}$$

Pomembna razlika med Ta_2O_5 in Nb_2O_5 sistemom je znatno nižja trdna topnost Ta v SnO_2 in posledično dvakrat višje razmerje Co:Ta, kar kaže, da je Co^{2+} edini dvovalentni kation, ki kompenzira Ta^{5+} naboj na Sn-mestih po naslednjem kompenzacijskem mehanizmu:

$$3\ \mathrm{Sn(IV)}^{\times}_{\mathrm{Sn\,(IV)}} \rightleftharpoons\ \mathrm{Co(II)}^{''}_{\mathrm{Sn\,(IV)}} + 2\ \mathrm{Ta(V)}^{\cdot}_{\mathrm{Sn\,(IV)}}$$

V drugem delu mojega doktorskega dela sem se posvetila dvojčenju SnO_2, ki je zelo pogosto, vendar še nepojasnjeno, medtem ko je v strukturno sorodnem rutilu TiO_2 mehanizem dvojčenja dobro raziskan. Z dodatkom specifičnih dopantov k SnO_2 keramiki sem skušala ugotoviti, kako prisotnost dvojčičnih mej vpliva na rast zrn, razvoj mikrostrukture ter električne lastnosti materiala. Pokazala sem, da dvojčenje v SnO_2 v ni kemijsko inducirano, ampak je najverjetneje posledica topotaksialnega rekristalizacijskega procesa v začetni stopnji rasti zrn.

Contents

List of Figures **xv**

List of Tables **xix**

Abbreviations **xxi**

Symbols **xxiii**

Chemical Symbols **xxv**

Glossary **xxvii**

1 Introduction **1**
1.1 Tin (IV) Oxide ... 2
1.1.1 Specifics of the rutile-type structure ... 3
1.1.2 Point defects ... 4
1.1.2.1 Point defects in pure stoichiometric compounds ... 6
1.1.3 Line defects ... 8
1.1.4 Planar defects ... 9
1.1.4.1 Twinning ... 9
1.1.4.2 Other types of planar defects ... 10
1.1.4.3 Twinning in compounds with the rutile-type structure ... 11
1.2 SnO_2-Based Ceramics ... 14
1.2.1 Sintering techniques ... 14
1.2.1.1 Conventional and advanced sintering techniques ... 14
1.2.1.2 Densificatio process ... 15
1.2.2 Electrical characteristics of SnO_2 ... 16
1.2.2.1 Varistor applications ... 16
1.2.2.1.1 Point defects in SnO_2-based ceramics ... 19
1.2.2.1.2 Atomic defect model for SnO_2 varistor ... 21
1.2.2.1.3 SnO_2-CoO-Nb_2O_5 ceramic system ... 21
1.2.2.1.4 SnO_2-CoO-Ta_2O_5 ceramic system ... 22
1.2.2.2 Dielectric properties ... 23

2 Aims and Hypothesis **25**
2.1 Objectives ... 25
2.2 Outline of Results ... 26

3 Twinning and Charge Compensation in Nb_2O_5–Doped SnO_2–CoO Ceramics Exhibiting Promising Varistor Characteristics **29**

4 Charge Compensation and Electrical Characteristics of Ta_2O_5-Doped SnO_2-CoO Ceramics 45

5 Microstructure Development in (Co,Ta)-Doped SnO_2-Based Ceramics with Promising Electric and Dielectric Properties 55

6 Conclusions 63

Appendix A Twinning and Charge Compensation in Nb_2O_5–Doped SnO_2–CoO Ceramics Exhibiting Promising Varistor Characteristics 65
A.1 Article`s Supporting Information 65

Appendix B Charge Compensation and Electrical Characteristics of Ta_2O_5-Doped SnO_2-CoO Ceramics 71
B.1 Article`s Supporting Information 71

References 73

Bibliography 85

Biography 87

List of Figures

Figure 1.1: a) Tetragonal unit cell of SnO_2 rutile structure, where each Sn^{4+} ion is coordinated by six O^{2-} ions, and each O^{2-} ion is in planar trigonal coordination with the nearest Sn^{4+} ions, and b) tetragonal unit cell of SnO litharge structure, where Sn^{2+} is in regular square-pyramidal coordination with four O^{2-} ions.....2
Figure 1.2: Isometric (left) and prismatic (right) habit of cassiterite crystals with main crystallographic planes (100), (010), (001), (110), (101) and (111), drawn in the Eric Dowty Shape program.....3
Figure 1.3: a) Distorted hexagonal (*AB-AB*) stacking along a- and b-axes in [001] projection with rectangular channels along the c-axis. The cations occupy one-half of the available octahedral sites, forming chains of edge-sharing octahedra along the [001] direction. (b) The projection of SnO_2 in the [010] direction with outlined unit cell. 4
Figure 1.4: Schematic representation of vacant atomic site (vacancy) and interstitial atom (interstitial), where an atom sits in an interstice instead of a normal lattice site [79].....5
Figure 1.5: Energy band gap diagram for semiconductor SnO_2 [82]. In a semiconductor, the highest occupied band is called the valence band (VB) and the lowest unoccupied band is called the conduction band (CB). The figure shows that the electrons can jump from VB into CB when they are excited (electron holes are formed in VB). The state-free energetic region between the valence band maximum and the conduction band minimum is called the band gap (E_{bg}) and is indicative of the electrical conductivity of a material. The Fermi level (E_F) is the highest energy occupied electron orbital at zero temperature (T=0) [83]..6
Figure 1.6: a) Schottky defect pair: cation and anion vacancy, and b) cation Frenkel defect pair: cation vacancy and cation interstitial ion. 7
Figure 1.7: Schematic presentation of a slip, caused by the movement of an **a)** edge dislocation, where Burgers vector **b** is perpendicular to the dislocation line, and **b)** screw dislocation, where **b** is parallel to the dislocation line. 8
Figure 1.8: a) Schematic representation of microscopic twinning [76]. b) Atomic configuration around the (101) twin boundary viewed from the common [010] direction in the boundary plane. Purple circles are for tin and red for oxygen atoms, respectively. ...10
Figure 1.9: Schematic representation of a) exaggerated grain growth in low-voltage ZnO-based varistor ceramics, with the addition of TiO_2, caused by the presence of IBS in some ZnO grains. Here, spinels are overgrown [95], and b) initial stages of IB nucleation in the ZnO-SnO_2 system, where we can clearly see the difference between normal (isometric) ZnO grains and anisotropic ZnO(IB) grains [106].....10
Figure 1.10: Schematic presentation of (101) and (301) rutile twins from Diamantina (Brazil), nucleated from the same precursor material (Al-rich hydroxylian pseudorutile-HPR). The formation of both types of twins is apparently related to the exolution of corundum-type phases, where corundum segregates to {101} planes of rutile and ilmenite to {301} planes of rutile [98].....12
Figure 1.11: SEM images of SnO_2 crystals grown (a) without any addition in SnO_2-Cu_2O flux system, (b) with the addition of trivalent dopant In_2O_3, (c) with the addition of trivalent dopant Fe_2O_3, which is showing slightly lower growth rates along c-axis, and (d)

with the addition of pentavalent dopant Nb_2O_5, where the number of twinned crystals (indicated by arrows) drastically increased [46]..... 13
Figure 1.12: Schematic representations of (a) compact powder, (b) partial densification of neck growth, and (c) fully densified neck growth with occlusion of a pore [109]. 15
Figure 1.13: Typical characteristic current-voltage curve of varistor [95]. 17
Figure 1.14: Schematic presentation of a) a coarse-grained microstructure for low-voltage varistor application, and b) a fine-grained microstructure for high-voltage applications [95]..... 18
Figure 1.15: Typical microstructures of ZnO-based and SnO_2-based varistor ceramics: a) a complex microstructure of ZnO grains, assisted by Bi-rich phase and spinel particles [95], b) a simple microstructure of SnO_2 grains without any secondary phase..... 19
Figure 1.16: Atomic defect model for Schottky barrier at the SnO_2 grain boundaries [39]..... 21
Figure 3.1: Linear shrinkage ($\Delta L/L$) with respect to temperature for different dopant concentrations in SnO_2 ceramics. Curve **a** shows SnO_2 sample doped with Co only, starting to densify at ~1200 °C. With the addition of 0.1 mol% Nb_2O_5, the onset of densification appears at ~ 1230 °C (curve **b**), while with the addition of 1 mol% of Nb_2O_5 (curve **c**), densification starts at ~ 1315 C, with the maximum rate achieved at 1430 °C. With higher addition of Nb_2O_5 (2 mol%), densification appears at even higher T (curve **d**), but due to the limitation of the heating-stage microscope (its use is restricted to T up to 1450 °C) cannot be determined precisely. 30
Figure 3.2: FEG-SEM image of thermally etched cross-sections of SnO_2-1 mol% CoO-1 mol% Nb_2O_5 ceramics, sintered at 1430 °C for 5 h. (a) In this sample, multiple (cyclic) and single twin boundaries are present. (b) Misorientation angle between twin individuals A and B: measured misorientation angle across twin boundary of **67.8° ± 0.2°** is the complementary angle of (101) twin boundary in cassiterite, which is 112.2°. 31

Appendix A. **Twinning and Charge Compensation in Nb_2O_5–doped SnO_2–CoO Ceramics Exhibiting Promising Varistor Characteristics:** *Article`s Supporting Information.*

Figure A1: Conventional sintering of ceramic materials. 66
Figure A2: Temperature sintering regime for sintering SnO_2-based ceramics. 67
Figure A3: Linear shrinkage rate as a function of temperature (T) for **(a)** SnO_2-1 mol% CoO and **(b)** SnO_2-1 mol% CoO- 1 mol% Nb_2O_5..... 68
Figure A4: EBSD area analysis about grain orientation in SnO_2-1 mol% CoO-1 mol% Nb_2O_5 ceramics. **(a)** EBSD map of the selected area. Yellow lines indicate TBs, where the grains are met in {101} twin orientation. **(b)** The inverse pole figure diagram revealed random spatial distribution of the crystallographic orientations of SnO_2 grains..... 69
Figure A5: (a) Dielectric permittivity versus frequency with a different content of the Nb_2O_5 dopant. (b) Dielectric loss vs. frequency for SnO_2–1 mol% CoO–x mol% Nb_2O_5 samples..... 70

Appendix B. **Charge Compensation and Electrical Characteristics of Ta_2O_5-Doped SnO_2-CoO Ceramics:** *Article`s Supporting Information.*

Figure B1: Sintering behavior of (Co,Ta)-doped SnO_2: temperature (*see* the blue curve) and displacement (*see* the red curve) as a function of sintering time 72
Figure B2: SEM images of thermally etched cross-sections of the SnO_2-1 mol% CoO-1 mol% Ta_2O_5 composition after SPS sintering at 900 °C/5 min: **(a)** Highly dense ceramics is obta by SPS, however the uniformity of ceramics is structural inhomogeneous (marked by red lines). (b) Unlike CS, a metastable compound $Sn_2Ta_2O_7$ is produced by the SPS.....72

List of Tables

Table 1.1: Crystallographic, physical and electrical properties of stannic oxide (SnO_2) and stannous oxide (SnO) [29], [50], [56]–[58].....3
Table 1.2: Description of sintering stages [121].....15

Appendix A. **Twinning and Charge Compensation in Nb_2O_5–doped SnO_2–CoO Ceramics Exhibiting Promising Varistor Characteristics:** *Article`s Supporting Information.*

Table A1: Molar ratios of input oxides for the synthesis of SnO_2-based ceramics.....66
Table A2: Dielectric permittivity ε at a fixed frequency 1 kHz with dielectric losses tan δ of the Nb_2O_5-doped SnO_2–CoO samples.....70

Abbreviations

AC	. . . Alternating Current
ARM	. . . Atomic Resolution Microscope
BSE	. . . Backscattered Electrons
CB	. . . Conduction Band
ccp	. . . cubic close packing
CS	. . . Conventional Sintering
DC	. . . Direct Current
EDS	. . . Energy Dispersive X-ray Spectroscopy
e.g.	. . . exempli gratia – for example
et al.	. . . et alii – and others
etc.	. . . et cetera - and so on
FEG-SEM	. . . Field Emission Gun - Scanning Electron Microscopy
FFT	. . . Fast Fourier Transform
FTO	. . . Fluorine-doped Tin Oxide
GB	. . . Grain Boundary
HAADF-STEM	. . . High-Angle Annular Dark-Field Scanning Transmission Electron Microscopy
hcp	. . . hexagonal close packing
HRTEM	. . . High Resolution Transmission Electron Microscopy
i.e.	. . . id est – that is
IB	. . . Inversion Boundary
ITO	. . . Tin-doped Indium Oxide
PIPS	. . . Precision Ion Polishing System
RT	. . . Room Temperature
SAED	. . . Selected Area Electron Diffraction
SPS	. . . Spark Plasma Sintering
STEM	. . . Scanning Transmission Electron Microscopy
TaTO	. . . Tantalum-doped Tin Oxide
TB	. . . Twin Boundary
TCO	. . . Transparent Conducting Oxide
TEM	. . . Transmission Electron Microscopy
VB	. . . Valence Band
XRD	. . . X-Ray powder Diffraction

Symbols

a	...	unit cell parameter
A	...	a base densely packed layer of anions
A	...	surface of the sample
ABA	...	sequence in hexagonal close-packed structure
A/cm^2	...	unit of electric current density
Å	...	Ångström; a metric unit of length, equal to 0.1 nm
b	...	unit cell parameter
b	...	Burgers vector
B	...	close-packed layer of anions, positioned between interstitials
c	...	unit cell parameter
C	...	capacitance
cm	...	unit of length in the metric system (a centimeter)
d	...	thickness of the sample
e	...	electron
eV	...	unit of energy (electron volt)
f_{TB}	...	frequency of twinning
g	...	metric system unit of mass (the gram)
F	...	unit of electrical capacitance (Farad)
F/m	...	unit for dielectric permittivity (Farad per meter)
h	...	electron hole
$h\nu$	...	photon energy
Hz	...	unit of frequency, defined as one cycle per second (Hertz)
i	...	interstitial
I	...	electrical current through the varistor
I_L	...	leakage current
J	...	current density
k	...	constant related to material microstructure
kHz	...	unit of frequency, equal to 10^3 Hz
K	...	the base unit of temperature (Kelvin)
$\frac{L_0 - L_1}{L_0}$	...	relative linear shrinkage
mA	...	physical unit for electrical current, the equivalent of 10^{-3} ampere (milliampere)
mm	...	unit of length in the metric system (a millimeter)
M	...	an atom of electropositive element (metal)

M_i	...	metal interstitial
MPa	...	unit of pressure, equal to 10^6 Pa
nm	...	unit of length in the metric system, equal to 10^{-9} m
N	...	number of grain boundaries
Pa	...	unit of pressure (Pascal)
$P4_2/mnm$	...	primitive tetragonal space group
R	...	electrical resistance
tan δ	...	dielectric loss
T	...	temperature
U	...	applied voltage
U_{GB}	...	voltage drop per grain boundary
U_N	...	nominal voltage
U_T	...	threshold voltage
V	...	vacancy
V_M	...	metal (cation) vacancy
V_O	...	oxygen vacancy
V_X	...	anion vacancy
V/mm	...	unit of measurement for threshold voltage (volt per millimeter)
X	...	an atom of electronegative element (anion)
X_i	...	anion interstitial
Z^2	...	dependency of atomic-column intensity
( )	...	planes of crystal structures
[ ]	...	plane directions
$^{\cdot}$	...	effective positive charge
$'$	...	effective negative charge
$^\circ$	...	the degree symbol
$\times$	...	zero (null) charge
Ω	...	unit of electrical resistance (the ohm)
α	...	nonlinear coefficient
α	...	angle in the unit cell (alfa)
β	...	angle in the unit cell (beta)
γ	...	angle in the unit cell (gama)
δ	...	phase angle between the signal of the sample and the signal, expected for an ideal lossless capacitor
ε	...	dielectric permittivity
ε_0	...	vacuum permittivity
ε_r	...	relative permittivity
μm	...	unit of length, equal to 10^{-6} m (a micrometer)
ρ_{rel}	...	relative density
ρ_v	...	electrical resistivity
ϕ_B	...	potential barrier height
ω	...	potential barrier width

Chemical Symbols

BaO	...	Barium (II) oxide
$BaTiO_3$	...	Barium titanate
Bi_2O_3	...	Bismuth (III) oxide
CeO_2	...	Cerium (IV) oxide
Co	...	Cobalt
CoO	...	Cobalt (II) oxide
Co^{2+}	...	Cobalt (II) ion
CrO_2	...	Chromium (IV) oxide
Cr_2O_3	...	Chromium (III) oxide
CuO	...	Copper (II) oxide
F	...	Fluor
Fe_2O_3	...	Iron (III) oxide
Ga_2O_3	...	Gallium (III) oxide
La_2O_3	...	Lanthanum (III) oxide
Nb	...	Niobium
Nb_2O_5	...	Niobium (V) oxide
Nb^{5+}	...	Niobium (V) ion
M_aO_b	...	Metal oxide with atoms in the ratio a:b
MnO	...	Manganese (II) oxide
MnO_2	...	Manganese (IV) oxide
MO	...	Metal oxide
O^{2-}	...	Oxygen (II) ion
O_2	...	Oxygen molecule
PbO	...	Lead (II) oxide
Pr_2O_3	...	Praseodymium (III) oxide
Pr_6O_{11}	...	Praseodymium (III, IV) oxide
Sb_2O_3	...	Antimony (III) oxide
Sb_2O_5	...	Antimony (V) oxide
Sm_2O_3	...	Samarium (III) oxide
Sn^{2+}	...	Tin (II) ion
Sn^{4+}	...	Tin (IV) ion
SnO	...	Tin (II) oxide
SnO_2	...	Tin (IV) oxide, stannic oxide
SnO_6	...	Octahedron in tetragonal unit cell of SnO_2 structure
$SnTa_2O_7$	...	Thoreaulite
$SrTiO_3$	...	Strontium titanate
Ta_2O_5	...	Tantalum (V) oxide
Ta^{5+}	...	Tantalum (V) ion
TiO_2	...	Titanium (IV) oxide, titanium dioxide
VO_2	...	Vanadium (IV) oxide
ZnO	...	Zinc oxide
$ZnSnO_3$	...	Zinc stannate
WO_3	...	Tungsten (IV) oxide

Glossary

acceptor (dopant) – dopant with lower oxidation state

anisotropy – difference in properties (chemical or physical) in different crystallographic directions

anthropogenic – caused by humans or their activities

band gap/energy gap – is an energy band in a solid where no electronic states can exist

conduction band – the band of electron orbitals that electrons can jump up into from the valence band when excited

dislocation – a linear crystallographic defect or irregularity within a crystal structure that contains an abrupt change in the arrangement of atoms

degradation – phenomenon of changing the voltage-current characteristics of varistors by increasing the current under operating voltage

donor (dopant) – dopant with lower oxidation state

dopants – foreign atoms, usually introduced into the crystal lattice of a semiconductor to modify its electrical properties

granite – coarse-grained igneous (magmatic) rock

halogens – are a group in the periodic table consisting of five chemically related elements: fluorine (F), chlorine (Cl), bromine (Br), iodine (I), and astatine (At)

hydrothermal vein – it forms when a hydrothermal solution flows through an open fissure and deposits its dissolved load

intragranular – occurring within a grain

isometric – property of a material with identical physical or mechanical properties along all crystallographic directions

n-type semiconductor – semiconductor, which has been doped with donor atoms; the majority of charge carriers in the crystal are (negative) electrons

pegmatite – an igneous (magmatic) rock, formed by slow crystallization at high temperatures and pressure at depth

pyrochlore group – complex oxide minerals with a composition of $A_2Nb_2(O,OH)_6Z$

spinel group – double oxide minerals with a composition of AB_2O_4

topotaxy – replacement reactions in solid state leading to a new phase with crystallographic orientations coherently adopting the orientations of the parent phase

transparency – the physical property of allowing the transmission of light through a material

twinning – when two crystals or crystal domains are in a special crystallographic setting that can be reproduced by a simple symmetry operation

valence band – the outermost electron orbital of an atom of any specific material that the electrons actually occupy

Chapter 1

Introduction

Tin dioxide (SnO_2) is a wide band gap (3.6 eV at RT) *n*-type semiconductor with a tetragonal rutile-type structure and an advantageous combination of chemical, electric and optical properties which makes it favorable in many applications. Due to its physical properties, such as transparency and semi-conductivity, it is one of the most used metal oxides for gas sensors [1]–[5], lithium batteries [6]–[8], transparent conductive coatings [9], [10], as catalytic support materials [11]–[14], for solar cells application [15]–[19] and also surge arrestors (varistors) [20]–[28]. SnO_2 belongs to the important family of transparent conducting oxide (TCO) materials that combine low electrical resistance with high optical transparency. An additional property of SnO_2 is that although it is transparent in the visible spectrum, it is highly reflective for infrared light and this property is responsible for today's predominant use of SnO_2 as an energy conserving material [29]. Tin-doped indium oxide (ITO) is often used to make transparent conductive coatings for displays such as flat panel display, liquid crystal displays, and plasma displays. Less expensive than ITO is the fluorine-doped tin oxide (FTO), which is ideal for use in a wide range of devices, including touch screen displays and energy-saving windows [9], [29]–[31]. Recently, Ta-doped tin oxide (TaTO) has shown high performance and the possibility of replacing FTO due to its low resistivity and better infrared transparency [32], [33].

SnO_2 is rarely used in its pure form since it exhibits poor sinterability and rather high electrical resistivity ($\rho_v \sim (0.5\text{–}1)10^{12}\ \Omega\ \mathrm{cm}$) [34]–[38]. The electrical conductivity of SnO_2 can be greatly enhanced by adding small amounts of dopants, which act as donors or acceptors [21], [39]–[43]. In terms of crystal growth, it is important to know whether the dopants promote (*e.g.* Co) or inhibit the grain growth (*e.g.* Nb) [20], [28], [41], [44], [45]. Doping tin oxide with tri- (Fe_2O_3) or pentavalent (Nb_2O_5, Ta_2O_5) oxides [24], [46]–[48] as well as with halogens (*e.g.* F) [30], [49] produced twin-like planar defects. The origin of twinning of synthetic or natural SnO_2 [50], which could give us important insights into their role in microstructure development and related physical properties, has so far not been studied.

Doctoral dissertation entitled "*Charge compensation mechanism and twinning in doped SnO_2-based ceramics*" focuses on low- and high-voltage SnO_2-based varistor ceramics with the emphasis on studying the influence of specific dopants (Co, Nb/Ta) on grain growth, microstructure development and related electrical properties. Based on targeted sample preparation and electron microscopy studies of SnO_2-CoO-Nb_2O_5 and SnO_2-CoO-Ta_2O_5 systems, I proposed novel charge compensation mechanisms that describe the solid-state reactions in the two systems. The doctoral topic also extends to the field of nanostructured research of planar defects (*i.e.* twin boundaries).

1.1 Tin (IV) Oxide

Owing to two valence states of tin, +2 and +4, there are two main oxides of tin: stannic oxide (SnO_2) and the less common stannous oxide (SnO). They both have a tetragonal structure. The stannic oxide (SnO_2) has a characteristic rutile structure (*see* Subchapter *1.1.1. Specifics of the rutile type structure*) as many other metal oxides (TiO_2, MnO_2, VO_2, CrO_2, etc.), while the stannous oxide has less common litharge structure (Figure 1.1), isostructural to α-PbO [52]. It consists of Sn-O-Sn layers stacked along the [001] direction with weak Van der Waals interactions between the layers. In this layered structure, Sn atoms are at the top of a square pyramid, based on O atoms. Both, SnO_2 and SnO, have two formula units per unit cell [51] - [54]. A summary of crystallographic, physical and electrical properties of SnO_2 and SnO is given in Table 1.

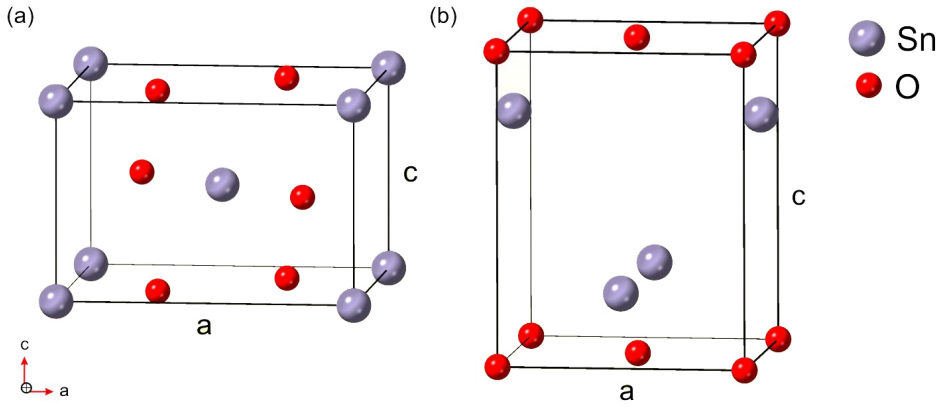

Figure 1.1: a) Tetragonal unit cell of SnO_2 rutile structure, where each Sn^{4+} ion is coordinated by six O^{2-} ions, and each O^{2-} ion is in planar trigonal coordination with the nearest Sn^{4+} ions, and b) tetragonal unit cell of SnO litharge structure, where Sn^{2+} is in regular square-pyramidal coordination with four O^{2-} ions.

SnO is metastable at ambient conditions and decomposes to Sn and SnO_2 above ~330°C [51], [52] while SnO_2 is reduced to SnO at high temperatures above 1300 °C [34]–[37] (more in Subchapter *1.2.2.1.1. Point defects in SnO_2-based ceramics*). SnO_2 is the most common form of tin oxide used in various technological applications [1]-[31], while SnO is also receiving considerable attention as an anode material in lithium rechargeable batteries, coating materials and as effective catalyst [53]–[55]. SnO occurs as a rare mineral romarchite, which is anthropogenic, as it was found on tin artifacts and is the product of tin corrosion in a cold freshwater environment [56], [57], while SnO_2 occurs as a mineral cassiterite and is the primary source of tin. As such, cassiterite has been found in economic concentrations in only few locations in the world (Australia, Brazil, Bolivia, China, England, Democratic Republic of the Congo, Peru, Portugal, Russia, Rwanda, Serbia, Spain and South-East Asia). Primary deposits of cassiterite are almost always linked to high-temperature hydrothermal veins and pegmatites that accompany granitic intrusions. However, most of the world's cassiterite is produced from secondary deposits, where cassiterite is concentrated in placers, such as stream valleys and shoreline sediments from granitic backgrounds [50], [58]. In a laboratory, SnO_2 can be synthesized using various techniques, including thermal decomposition [59], [60] hydrothermal synthesis [61]–[65], sol-gel [66]–[68], flux method [46], [47] and solid state processing [24], [42], [69]–[75], where the size, morphology and crystal habit of the particles depends on the synthesis technique.

Table 1.1: Crystallographic, physical and electrical properties of stannic oxide (SnO_2) and stannous oxide (SnO) [29], [50], [56]–[58].

	SnO_2	**SnO**
Chemical name	tin(IV) oxide, tin dioxide, stannic oxide	tin (II) oxide, tin monoxide, stannous oxide
Mineralogical name	cassiterite	romarchite
Sn oxidation state	+4	+2
Crystal structure	tetragonal, rutile	tetragonal, litharge
Space group	$P4_2/$ mnm	P4/nmm
Lattice constants [nm]	a = b = 0.474, c = 0.319 $\alpha = \beta = \gamma = 90°$	a = b= 0.380, c = 0.484 $\alpha = \beta = \gamma = 90°$
Molar mass [g mol^{-1}]	150.71	134.71
Density [g cm^{-3}]	6.95	6.45
Melting point [°C]	1630	1080
Hardness- Mohs	6-7	4
Band gap [eV]	3.6	2.5-3.0

1.1.1 Specifics of the rutile-type structure

SnO_2 crystallizes in the rutile-type structure with a tetragonal (*see* Table 1) unit cell. SnO_2 (cassiterite) crystals have either isometric or prismatic habit (Figure 1.2.), with the most common crystallographic forms (110), (111), (100), and (101).

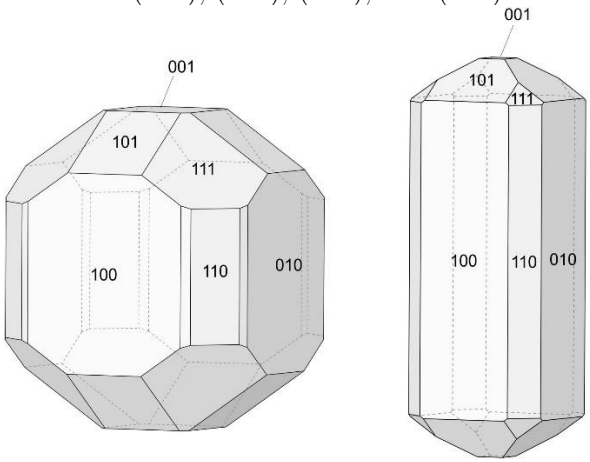

Figure 1.2: Isometric (left) and prismatic (right) habit of cassiterite crystals with main crystallographic planes (100), (010), (001), (110), (101) and (111), drawn in the Eric Dowty Shape program.

In the cassiterite structure, eight Sn^{4+} ions are located at the corners and one at the center of the unit-cell. They are octahedrally coordinated by O^{2-} ions, of which two are fully inside and the other four are ½ shared by the neighboring unit-cells across the cell faces. SnO_6 octahedra are the basic structural element, which is repeated throughout the structure. Along the crystallographic c-axis, SnO_6 octahedra are interconnected by their edges, forming endless chains, linked to neighboring chains through corners. In this arrangement, rectangular channels along the c-axis are the main characteristic of the rutile-type structure as illustrated in Figure 1.3 a. In this structure, SnO_6 octahedra are slightly distorted through compression of the equatorial four anions producing a tetragonal

bipyramid with four short Sn-O bonds and two long ones. This structure is in fact derived from hexagonal close-packed (*hcp*) O-sublattice, where Sn^{4+} cations fill only one-half of the available octahedral sites, whereas the other half remains empty. In the hexagonal close-packed (*hcp*) rutile structure, the repeat sequence consists of two anionic layers, A and B, stacked in a hexagonal manner, where the cations occupy half of the octahedral sites. The anionic stacking can be written as: *A-B-A-B-A-B-....* The tetragonal distortion of the rutile structure causes undulation in the O-sublattice, so we can refer to it as a distorted, pseudo-hexagonal oxygen network [76]. This pseudo-hexagonal arrangement can be seen along both crystallographic a- (and b)-axes of the structure (Figure 1.3 b). Any deviation from the standard stacking of SnO_6 octahedra, or different occupancy of the available interstitials, results in a planar defect.

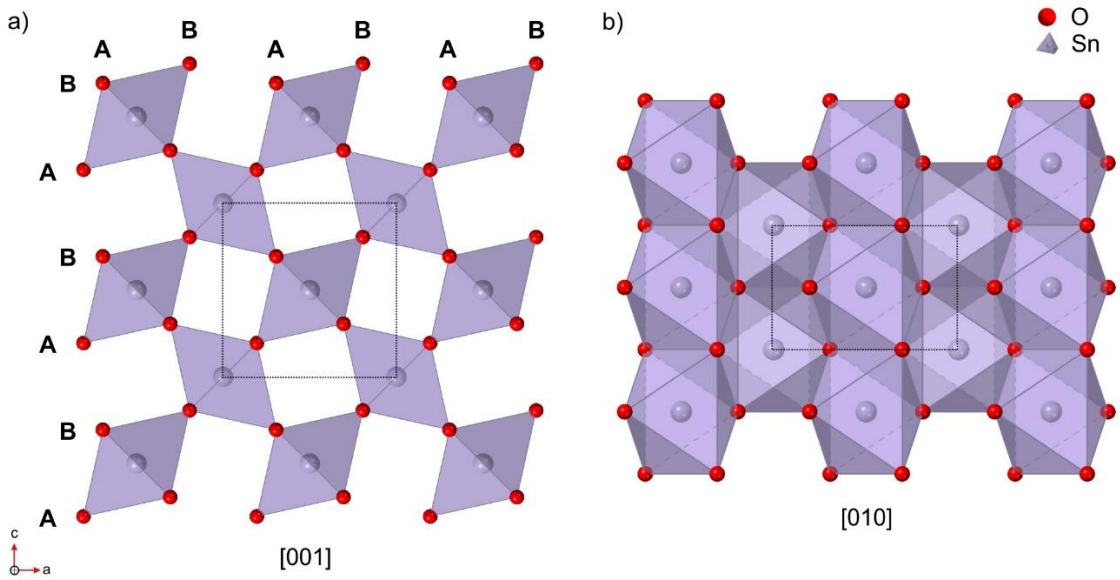

Figure 1.3: a) Distorted hexagonal (*AB-AB*) stacking along a- and b-axes in [001] projection with rectangular channels along the c-axis. The cations occupy one-half of the available octahedral sites, forming chains of edge-sharing octahedra along the [001] direction. (b) The projection of SnO_2 in the [010] direction with outlined unit cell.

1.1.2 Point defects

During the 19th century, the crystallographers believed that the atoms in crystals were always perfectly arranged, until the 1930s when Wagner and Schottky [77] showed through statistical thermodynamic treatments of mixed phases that the crystal structures are not ideal. Imperfections inside otherwise ideal structure are called defects. If the imperfection is limited to one structural or lattice site and its immediate vicinity, it is called a zero-dimensional (0D) or point defect. Point defects can be either vacant atomic sites (vacancies), interstitial atoms (interstitials) or impurity atoms that occupy regular structural or interstitial sites (Figure 1.4) [78], [79]. Related to structural imperfections, the crystals can also contain electronic defects, *i.e.* defect electrons and electron holes, which move relatively freely in the crystal. The electronic defects can be generated by the internal excitation of valence electrons or may be formed in connection with point defects. If electronic defects are trapped at regular sites in the structure, they are called valence defects [78].

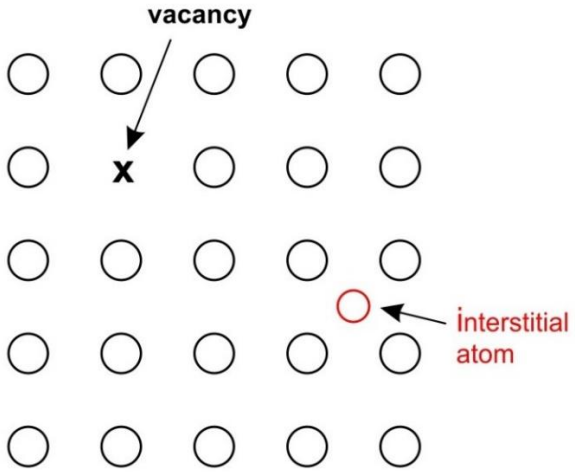

Figure 1.4: Schematic representation of vacant atomic site (vacancy) and interstitial atom (interstitial), where an atom sits in an interstice instead of a normal lattice site [79].

To describe point defects, various notations have been proposed. Out of these, Kröger-Vink notation is the most commonly used [80]. In a generic discussion of defect reactions, M and X are often used, where M is an atom of an electropositive element and X is an atom of an electronegative element. Vacancies are denoted by "V" and interstitial sites with "i". Different symbols are used for the effective charges relative to the actual charges (+ or -): dot ($^{\cdot}$) for the effective positive charge, slash ($'$) for the effective negative charge and $^{\times}$ is used to indicate the zero charge. In the semiconduction field, the principles are the same, however extra electrons in the normally empty conduction band (defect electrons) are written as e' with effective negative charge and lacking electrons in the valence band (electron holes) are written as $h^{\cdot}$ and have an effective positive charge (Figure 1.5).

To apply the thermodynamics of chemical reactions that involve defects, the following three rules must be satisfied [78], [81]:

I. Mass balance – (vacancies and electronic defects do not affect the mass balance) the total number of atoms must be the same on both (on the left and right) sides of the defect formation reaction.

II. Charge balance – (electroneutrality)-the resulting state must remain neutral; the charge neutrality is preserved.

III. Site balance – (ratios of regular lattice sites are conserved)-proportion of M and X sites stays unchanged if they are occupied or not.

When the M_aO_b oxides have atoms in the exact a:b ratio, we have a stoichiometric composition.

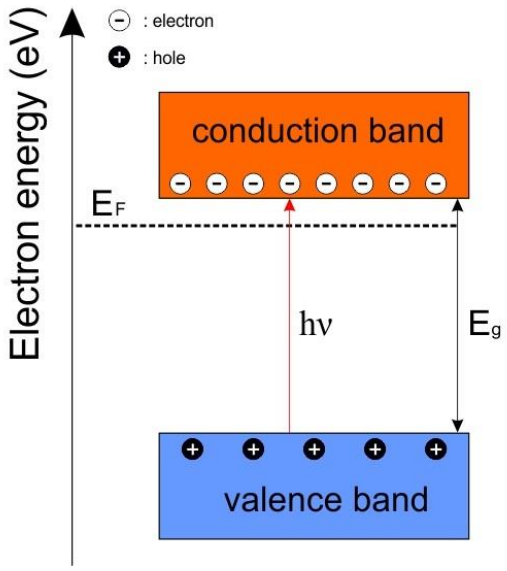

Figure 1.5: Energy band gap diagram for semiconductor SnO_2 [82]. In a semiconductor, the highest occupied band is called the valence band (VB) and the lowest unoccupied band is called the conduction band (CB). The figure shows that the electrons can jump from VB into CB when they are excited (electron holes are formed in VB). The state-free energetic region between the valence band maximum and the conduction band minimum is called the band gap (E_{bg}) and is indicative of the electrical conductivity of a material. The Fermi level (E_F) is the highest energy occupied electron orbital at zero temperature (T=0) [83].

1.1.2.1 Point defects in pure stoichiometric compounds

In a stoichiometric crystal with composition MX, five primary types of atomic disorder can be distinguished [78], [80], [81]:

I. Schottky disorder (Figure 1.6 a): forming equal concentration of vacant M sites (V_M) and vacant X sites (V_x)

$$\emptyset \rightleftharpoons V'_M + V^{\cdot}_X \tag{1.1}$$

In stoichiometric oxide MO there are also equal concentrations of metal and oxide ion vacancies:

$$M^{\times}_M + O^{\times}_O \rightleftharpoons V''_M + V'_O + M^{\times}_M + O^{\times}_O \tag{1.2}$$

$$\emptyset \rightleftharpoons V''_M + V^{\cdot\cdot}_O \tag{1.3}$$

Charged Schottky disorder: forming an electron-hole pair

$$\emptyset \rightleftharpoons e' + h^{\cdot} \tag{1.4}$$

II. Frenkel disorder (cation Frenkel pair, shown in Figure 1.6 b): forming equal concentrations of metal (cation) vacancies (V_M) and metal interstitial ions (M_i)

$$\emptyset \rightleftharpoons V'_M + M_i^{\cdot} \tag{1.5}$$

III. Frenkel disorder (anion Frenkel pair): forming equal concentrations of anion vacancies (V_x) and anion interstitials (X_i)

$$\emptyset \rightleftharpoons V_X^{\cdot} + X'_i \tag{1.6}$$

IV. Anti-structure disorder: where part of atoms M occupies X positions (M_x) and an equal number of X atoms occupy M positions (X_M). This disorder is ordinary in intermetallics and between anions or cations on different sites.

V. Very rare disorder: forming electropositive interstitial atoms (M_i) together with an equal concentration of electronegative interstitial atoms (X_i).

Schottky defects can only occur on surfaces and other extended defects (such as grain boundaries and dislocations), since the atoms at vacated sites must escape, while, conversely, Frenkel defect pairs can form directly inside the crystal by the atoms going directly into interstitial sites (from the normal sites). In crystals where cations and anions are of a comparable size and the structure is effectively packed, Schottky defects are common, but when the sizes of the cations and anions are significantly different, Frenkel defect pairs predominate [78].

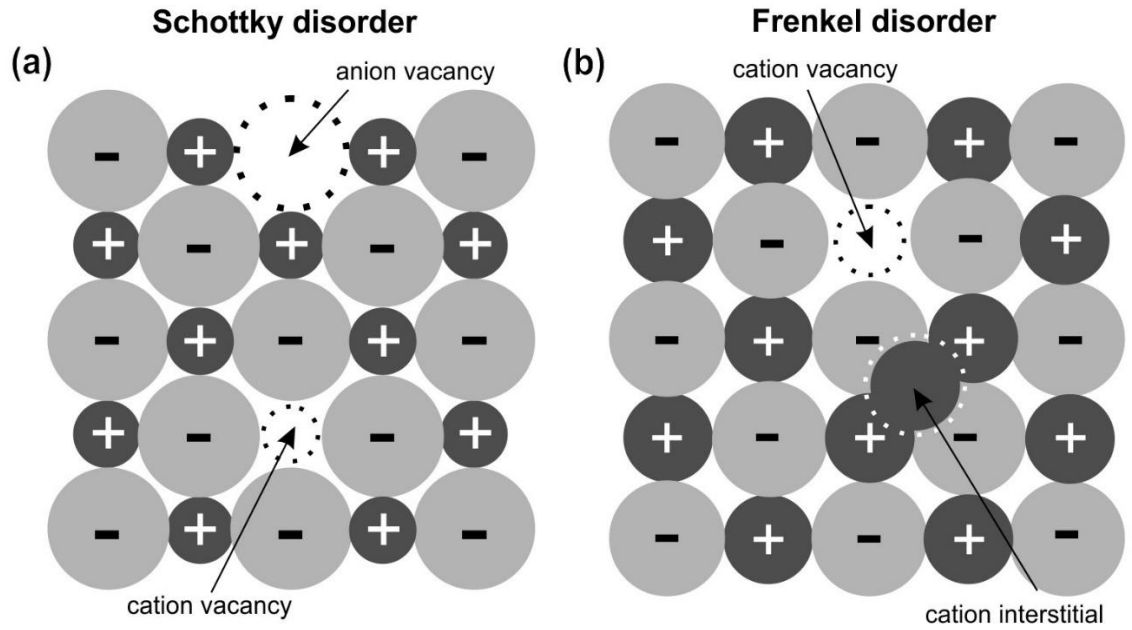

Figure 1.6: a) Schottky defect pair: cation and anion vacancy, and b) cation Frenkel defect pair: cation vacancy and cation interstitial ion.

1.1.3 Line defects

In addition to zero dimensional defects (point defects), structural defects also include line and planar defects. Line defects or one-dimensional (1D) defects are termed *dislocations*, and they are characterized by displacements in the structure in certain directions. Dislocations allow materials to deform without destroying the basic crystal structure, but during deformation due to the slipping of atomic layers one above the other, the crystal changes its shape. The slip plane may be divided into two regions: slipped and unslipped, where a boundary between these two regions is referred to as a dislocation line. Dislocation as a line discontinuity, forms a closed loop in the interior of the crystal and the difference in the amount of slip across the dislocation line is constant. The direction and magnitude of the lattice distortion, caused by a dislocation, is expressed in terms of a Burgers vector, **b** [78], [79].

There are two basic types of dislocations:

- Edge dislocations, where an extra half-plane of atoms is inserted in a crystal structure and **b** is directed perpendicular to the dislocation line.
- Screw dislocation is parallel to the direction in which the crystal is being displaced and **b** is parallel to the dislocation line.

Mixed dislocations that combine aspects of both types (edge and screw dislocations) are also common.

Dislocations are commonly described in HRTEM studies of wurtzite structures (ZnO, GaN), as well as in rutile structures (TiO_2, SnO_2) [84]–[90]. In SnO_2, the occurrence of dislocations is often associated with twinning. Iwanaga *et al.* [86] observed dislocations in the end part of twinned SnO_2 whiskers, Zheng *et al.* [87] reported a large number of twins and dislocations in the SnO_2 films, while Tseng *et al.* [88], [89] reported on edge dislocations near the TBs in polysynthetically twinned SnO_2. Similar edge dislocations are also discussed in isostructural TiO_2 [90].

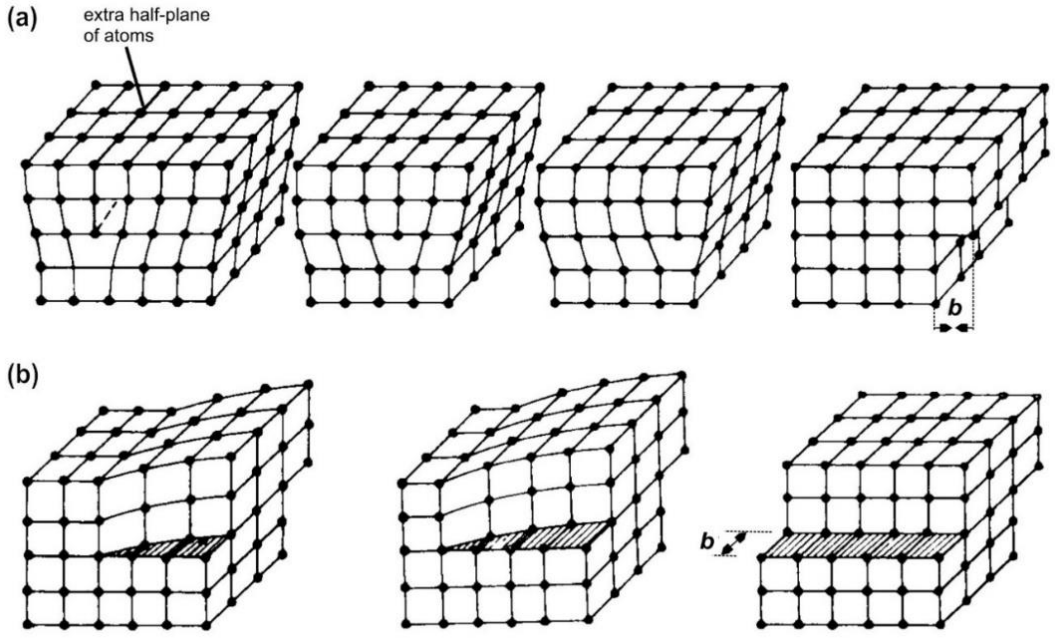

Figure 1.7: Schematic presentation of a slip, caused by the movement of an **a)** edge dislocation, where Burgers vector **b** is perpendicular to the dislocation line, and **b)** screw dislocation, where **b** is parallel to the dislocation line.

1.1.4 Planar defects

Significant defects in crystalline engineering materials are two-dimensional (2D) or planar defects, involving internal interfaces (general grain boundaries, twin boundaries, inversion boundaries, stacking faults) or external interfaces (surfaces). While plastic deformation occurs in the material due to the movement of dislocations (*see* Figure 1.7), any defect in the regular lattice structure disturbs the movement of dislocations, which makes a slip or plastic deformation more difficult [91].

Grain boundaries are often classified as low angle, special or general based on their structure and/or properties. A general grain boundary (GB) usually separates crystals which differ in orientation by large angles. In the case of a twin boundary, however, the boundary is between two orientations of the same phase, where grains are in a special, coincident site lattice (Σ=3) relationship and the orientations are not random since they are related by mirror or 180° rotation operation across the twin-plane. Twinning is the dominant deformation mechanism in materials with low stacking fault energy. Stacking faults are planar defects in which the regular order of stacking planes is interrupted in a close-packed crystal structure. For example, if the cubic close packed (*ccp*) stacking sequence is A-B-C, the stacking fault occurs if the plane of atoms is missing from the normal sequence, *e.g.* A-C-A-B-C-... causing a local *hcp* stacking, or the plane of atoms is inserted, *e.g.* A-B-C-B-A-B-C-... similarly producing a local *hcp* sequence [79], [91], [92]. In order to distinguish whether a planar defect is a stacking fault or an inversion boundary (IB), it is necessary to determine the absolute orientation of the polar axis, when crystals are noncentrosymmetric, on both sides of the planar fault. In the case of IB, inversion of polarity takes place over the fault plane, while in the case of stacking faults there is no polarity inversion [93].

1.1.4.1 Twinning

Twin boundaries are a common type of planar defects that can be introduced in a perfect crystal by simple crystallographic operation, as shown in Figure 1.8 a. The translation of the crystal structure is (mirror) symmetric across the boundary and there is no loss of the lattice continuity (Σ=3) [76]. In rutile (cassiterite) twins, only the cation sublattice is mirrored, while the oxygen sublattice is continuous. Periodically repeated twinning across the structure leads to the formation of modulated polytypic structures with elements of the twin boundary as well as the elements of the bulk crystal phase. The origin of such defects can be kinetic or thermodynamic. Kinetic defects are stacking faults and deformation twins. These defects can be annealed from crystals by appropriate thermal treatment. On the other hand, thermodynamic defects are irreversible and are more stable than the parent crystal [94]–[96]. Among these, the most common are growth twins, which are chemically triggered by a specific dopant that stabilizes the twin boundary structure.

The theory of tropochemical twinning was established in the 1970s in the study of modulated structures in minerals [97]. The basic assumption of this theory is that during crystal growth incorporation of certain dopants stabilizes some new, structurally related interstitials incurred as a result of specific crystallographic operations in the defect plane. In the nucleation stage of twin formation, dopant atoms chemisorb to specific crystallographic planes of the host in a highly ordered manner. In effect, chemically stabilized twin boundary lowers the total energy of the system causing anisotropic growth of the affected crystals along the twin plane. In the later stages, crystal domains develop characteristic twin-plane re-entrant angles [30], [31]. In order to identify the elements that trigger twinning, new techniques that enable atomic scale determination of the interfacial

crystal chemistry were developed [94]–[96], [98], [99]. Apart from this mechanism, twins can be a result of more complex replacement reactions, as explained in Section 1.1.4.2. One of the future objectives in materials design, however, involves twinning that offers a wide range of possibilities to grow complex branched architectures with tunable physical properties [100].

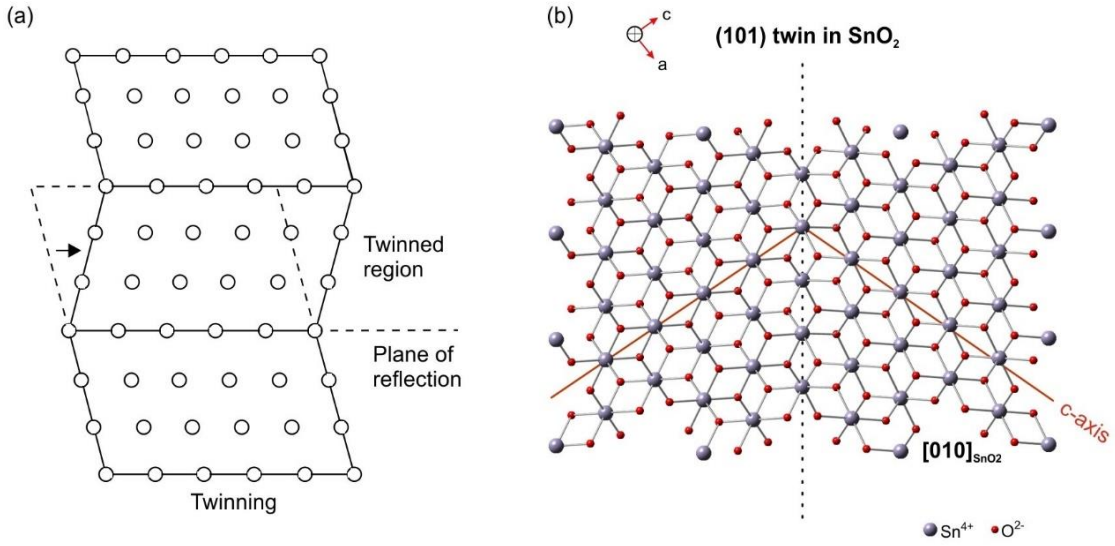

Figure 1.8: a) Schematic representation of microscopic twinning [76]. b) Atomic configuration around the (101) twin boundary viewed from the common [010] direction in the boundary plane. Purple circles are for tin and red for oxygen atoms, respectively.

1.1.4.2 Other types of planar defects

Other types of chemically-induced 2D structural defects are known in wurtzite materials, such as ZnO. Makovec *et al.* [101], [102] reported exaggerated growth of ZnO grains, caused by the occurrence of liquid phase and accompanied by the formation of Ti-rich inversion boundaries (IBs) in some ZnO grains. IBs are the most common type of planar faults in ZnO structure, which intersect ZnO grains and can be triggered by the addition of specific spinel-forming additives. Owing to rapid growth of grains with IBs in TiO_2-doped ZnO, voids and spinel particles are overgrown, producing coarse-grained microstructures, suitable for low-voltage varistor applications (Figure 1.9 a). Daneu *et al.* [103] later studied microstructural development in SnO_2-doped ZnO ceramics. They showed that in the early stages of sintering, the formation of inversion boundaries is triggered by the addition of SnO_2 causing anisotropic grain growth parallel to the fault plane. Exploiting this mechanism, they demonstrated that it is possible to control the microstructure development of varistor ceramics. They showed that in samples with a lower SnO_2 content, the grains are larger and fewer, while with larger additions of SnO_2, more nuclei are formed, leading to an increase of grains with IBs and formation of finer-grained microstructures. ZnO grains that contain IBs grow exaggeratedly, at the expense of normal grains, until they dominate (in a truly short time) the microstructure via the so-called IB-induced exaggerated grain growth mechanism. As a result, the grains become highly anisotropic (Figure 1.9 b) [103], [104]. Further, Sb_2O_3 is also a common dopant in high-voltage ZnO varistor ceramics that triggers the formation of IBs in ZnO grains [105], [106].

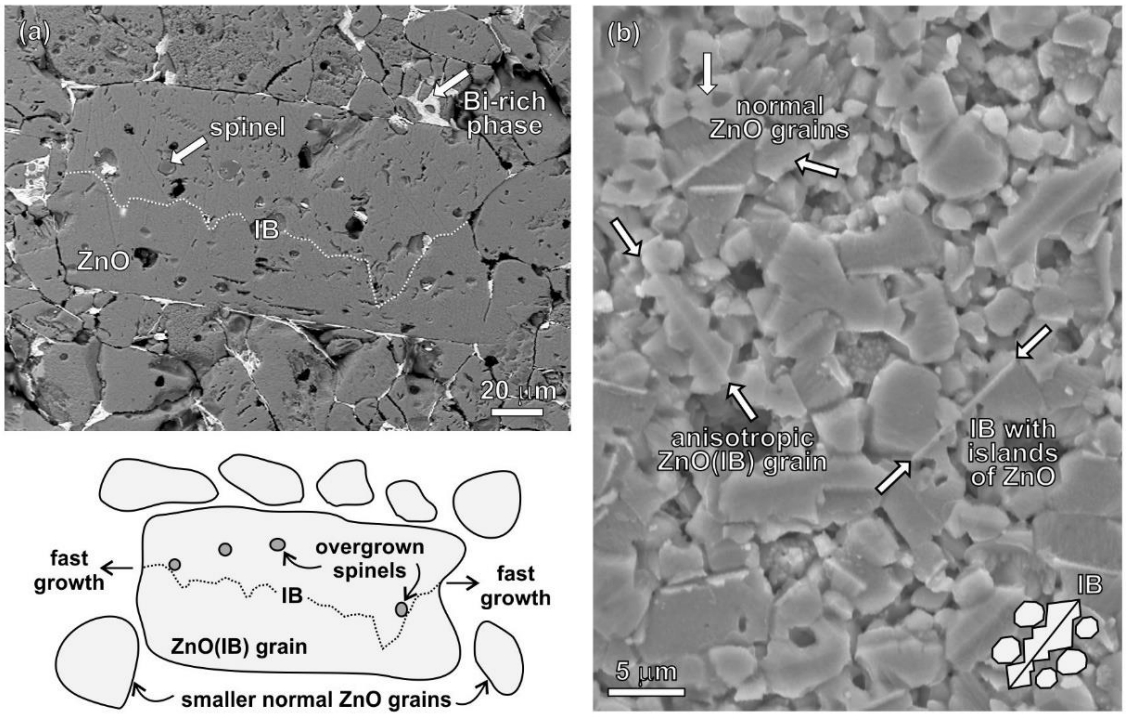

Figure 1.9: Schematic representation of a) exaggerated grain growth in low-voltage ZnO-based varistor ceramics, with the addition of TiO_2, caused by the presence of IBs in some ZnO grains. Here, spinels are overgrown [95], and b) initial stages of IB nucleation in the ZnO-SnO_2 system, where we can clearly see the difference between normal (isometric) ZnO grains and anisotropic ZnO(IB) grains [106].

1.1.4.3 Twinning in compounds with the rutile-type structure

In structurally related mineral rutile [98], [99], the mechanisms of twinning are well-studied, while the origin of twinning in SnO_2 is poorly understood. The {101} and {301} twins of rutile were demonstrated to be a consequence of complex topotaxial replacement reactions (Figure 1.10). (301) twins of rutile from Diamantina in Brazil [99] were shown to contain a few nanometers thick lamella of a corundum-type phase, consisting of Al-rich ilmenite ($FeTiO_3$). This lamella formed by thermally-induced dehydration of twinned tivanite-like Fe-Ti-Al oxy-hydroxide precursor. The study of (101) twins in rutile, also from Diamantina [98], showed a similar origin, with the main difference in the interface composition, which was decorated by Ti-rich corundum (Al_2O_3) precipitates that formed by dehydration of diaspore.

Like in rutile [96], [98], [99], topotaxial mechanism could also be responsible for twin formation in SnO_2. Namely, rutile (TiO_2) and cassiterite (SnO_2) are isostructural and show identical types of twins [58], [107]. In SnO_2, {101} twin boundaries are very common, recently studied by Nespolo & Souvignier [107], and like in rutile, twinning on {301} was also reported [86]. In SnO_2, the twinning is present in both pure and doped SnO_2 [30], [34], [46]–[48], [86]–[88], [90]. In 1965, Nagasawa *et al.* [34] determined {101} twin planes in SnO_2 crystals, which were grown by the vapor reaction method. Iwanaga *et al.* [86] identified two types of mirror twins, (301) and (121), in SnO_2 whiskers produced by oxidizing metallic tin, while Suzuki and co-workers [90] studied deformation twins in polycrystalline SnO_2. Furthermore, Zheng *et al.* [87] reported on multiple twins grown from

amorphous SnO_{2-x} films, which differed from those in SnO_2 whiskers. Polysynthetic twins are reported, when SnO_2 was transformed from orthorhombic $CaCl_2$-type structure [88].

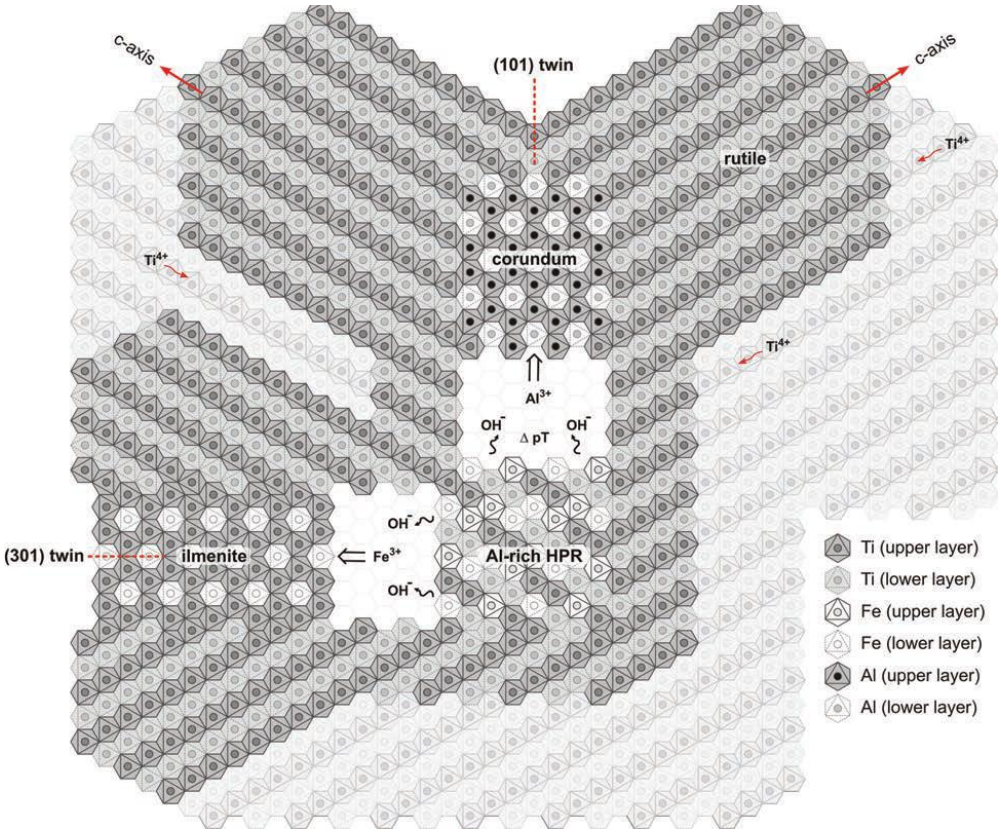

Figure 1.10: Schematic presentation of (101) and (301) rutile twins from Diamantina (Brazil), nucleated from the same precursor material (Al-rich hydroxylian pseudorutile-HPR). The formation of both types of twins is apparently related to the exolution of corundum-type phases, where corundum segregates to {101} planes of rutile and ilmenite to {301} planes of rutile [98].

Using the SnO_2-Cu_2O flux system, Kawamura *et al.* [46], [47] systematically investigated growth of SnO_2 and showed that trivalent dopants (Fe_2O_3, Sb_2O_3 and Ga_2O_3) accelerated SnO_2 growth along its c-axis and triggered abundant twinning of SnO_2. They also showed that the presence of trivalent dopants lowers the activation energy for nucleation, reduces the critical driving force to form twin nuclei and consequently increases the possibility of twin formation. Furthermore, pentavalent dopants, such as Nb_2O_5, Ta_2O_5 and Sb_2O_5, suppressed the growth and also caused heavy twinning of SnO_2 (Figure 1.11). Similar observations were made by Tomaev and Glazov [48], who investigated the morphology of polycrystalline SnO_2 films, grown on corundum substrates and suggested that doping can be used to control the concentrations of twins. They reported that doping SnO_2 films with trivalent metal oxides (Sb_2O_3 and Yb_2O_3) triggered abundant twinning. Also in (Co,Nb)-doped varistor ceramics, to which La_2O_3 was added, the formation of twins was observed [24]. Besides the doping with oxides, Cachet [30] reported the formation of twin-like planar defects on doping with halogens, like fluorine. Doping with fluorine had no influence on grain growth nor on the grain size. Commercially available F-doped SnO_2 (FTO) films also contain planar defects (twins) [30], [49]. The large number of reports on twinning of SnO_2 under various conditions and with different dopants shows that twins are easily produced in SnO_2, but nevertheless the mechanism of their formation has not been explained yet.

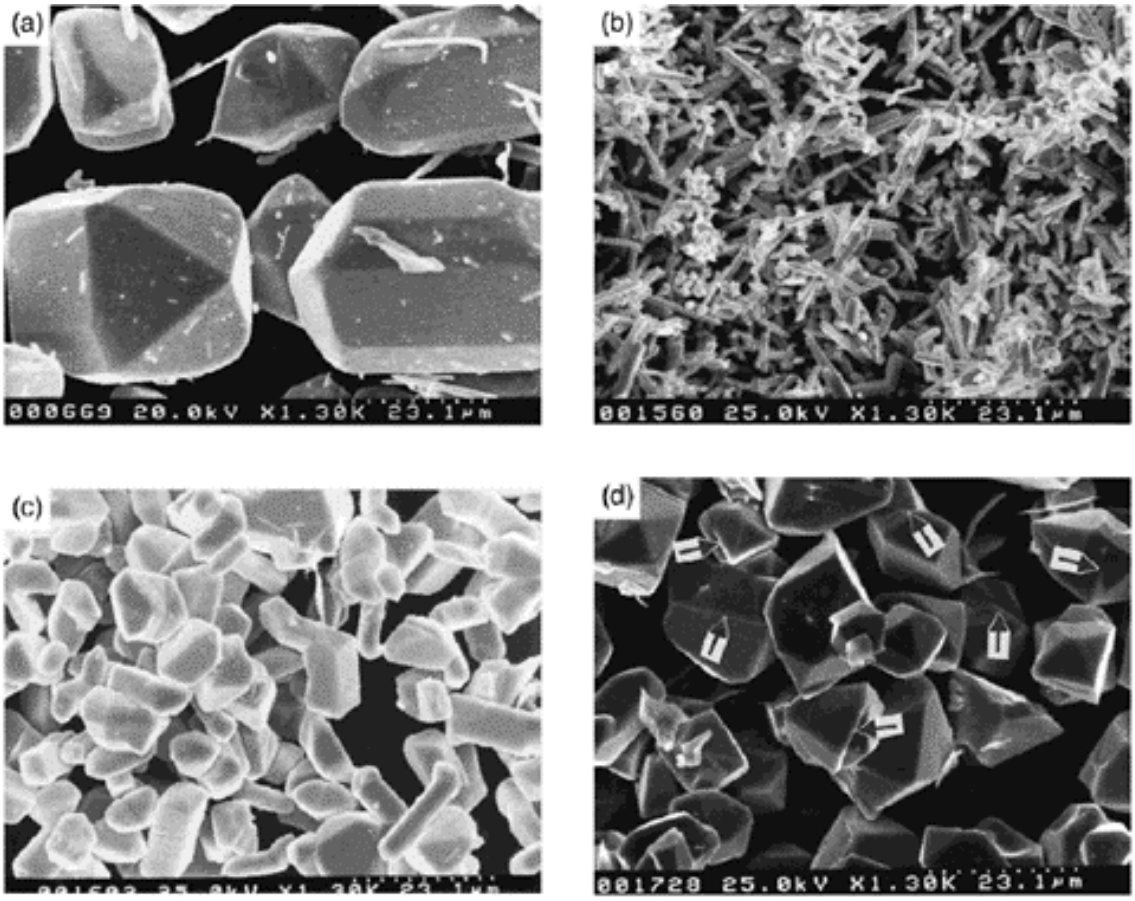

Figure 1.11: SEM images of SnO_2 crystals grown (a) without any addition in SnO_2-Cu_2O flux system, (b) with the addition of trivalent dopant In_2O_3, (c) with the addition of trivalent dopant Fe_2O_3, which is showing slightly lower growth rates along c-axis, and (d) with the addition of pentavalent dopant Nb_2O_5, where the number of twinned crystals (indicated by arrows) drastically increased [46].

Based on microstructural studies of IBs in ZnO-based ceramics, where grain growth is entirely controlled by IBs, I aimed to apply a similar approach to SnO_2 ceramics. The challenge was to identify whether the twin boundaries (TBs) have a decisive role in grain growth and microstructure development of SnO_2-based ceramics like IBs in ZnO-based ceramics. Motivated by the study of Kawamura *et al.* [46], [47], who reported of heavy twinning in SnO_2 with the addition of Nb_2O_5 and Ta_2O_5, and unusual effects of pentavalent dopant addition on microstructure development in SnO_2-based ceramics [44], I chose these two ceramic systems: SnO_2-CoO-Nb_2O_5 and SnO_2-CoO-Ta_2O_5 for our twin formation studies. The key objective was to determine how these dopants influence the twin formation in SnO_2.

1.2 SnO_2-Based Ceramics

In recent years, SnO_2-based ceramic materials have been extensively studied due to their special optical and electrical properties, making them attractive for a wide range of applications, including varistors. High density in polycrystalline ceramics and control of crystal growth and morphology are essential for the good varistor properties that occur in the region of the materials grain boundaries. The main limitation of the wider use of SnO_2-based ceramics is poor sinterability, associated with the low diffusivity of the SnO_2 structure and the predominance of non-densifying mechanisms. The sintering problem is further complicated by the high vapor pressure of SnO, therefore dense SnO_2-based materials are obtained either by using dopants or high pressures.

1.2.1 Sintering techniques

Sintering is one of the oldest, simplest and fastest techniques, where unique, multiple-phase microstructures can be produced by mixing different powders, and it holds an important place in materials processing technology. It is a process, in which the porous material passes through a heat treatment and densifies into a solid compact with largely reduced porosity [108], [109]. The process usually begins by setting a specific ratio of starting powders (mixtures of different oxides) with high purity. The simplest functional method for homogenization of the mixed oxide powders is the use of an agate-mortar [42], [75]. Alternatively high energy ball milling is also common in the varistor ceramic preparation [24], [38], [60], [70], [71], [110]–[113], however, contamination from the milling media often occurs [114]. After homogenization, the mixed powder is pressed into pellets or disks and sintered in the optimum range of temperature to achieve dense ceramics with the desired mechanical properties and density. Sintering temperature is usually estimated on the basis of the material melting point. The closer is the sintering temperature to the melting point, less strong are the bonds in the crystal lattice and the number of surface defects increases. Sintering of ceramics is accelerated if a small amount of melt is present during sintering (often 1 vol% of melt is sufficient), as the diffusion processes and consequently the densification in the presence of melt is faster. An important parameter is also the solubility of solid components in the melt, the data of which are obtained from phase diagrams [108].

1.2.1.1 Conventional and advanced sintering techniques

Conventional (or pressureless) sintering (CS) is the simplest approach, where the compact is heated without external pressure applied during the process. Compared to advanced sintering, this approach involves lower processing costs, making it more attractive for mass production of ceramic products. On the other hand, advanced sintering involves additional external power such as hot-pressing, microwave or spark plasma (SPS). When using the hot pressing method of sintering, ceramic materials usually densify at lower temperatures than in CS, have improved densification kinetics and limited grain growth. The main disadvantages of this process are limited geometry of the final product and higher investment and maintenance cost. Microwave sintering usually produces samples with better mechanical properties than CS, provides great microstructure control and reduced manufacturing costs due to low temperature, processing time and energy used [115], [116]. However, more recently, spark plasma sintering (SPS) hot pressing technique has been

developed, in which a graphite die that contains the powder is directly heated by pulsed electrical current under compressive stress with very fast sintering rates (up to 1273 K/min) [117]. It has been successfully used for producing dense SnO_2 materials at lower temperatures and significantly shorter sintering times [113], [117]–[119]. However, even if high densification for SnO_2-based ceramics is achieved by SPS, uniformity of the ceramics would not be sufficient for most of the applications. In addition, considerable amounts of carbon remain infiltrated in ceramic samples due to the use of graphite die, even after post-annealing [113]. Pressure-assisted sintering methods have, despite the rapid kinetics, several serious limitations reducing their ability to produce components of various shapes and sizes, which are required in industry [38].

1.2.1.2 Densification process

Sintering by solid-state diffusion consists of three stages as detailed in Table 2. In the initial sintering stage, the powder particles are exposed to sintering forces, so they begin to oscillate and slide into more stable arrangements. Due to the movement of the particles, the entire microstructure shrinks, which contributes to the overall increase in density. Moreover, necks start to form between the particles, as shown in Figure 1.12, while significant grain growth is not yet involved. In the intermediate stage, individual particles begin to evolve due to the Oswald ripening mechanism, but the overall density is still low due to the high fraction of pores, which are connected with each other. At this stage, the grain growth is still slow, sometimes negligible, as the grains are mostly separated by the pores. Locally, linked pores are separated, and so-called closed pores are formed. In the final stage, the reduction of pores increases the total density approaching a theoretical value. Grain growth reaches a crucial step, when larger grains grow exponentially at the expense of smaller grains [108], [109], [115], [120]. For the products used in electronics, very dense materials are desirable to achieve the properties such as high dielectric permittivity and low dielectric losses, which largely depend on the density of the material.

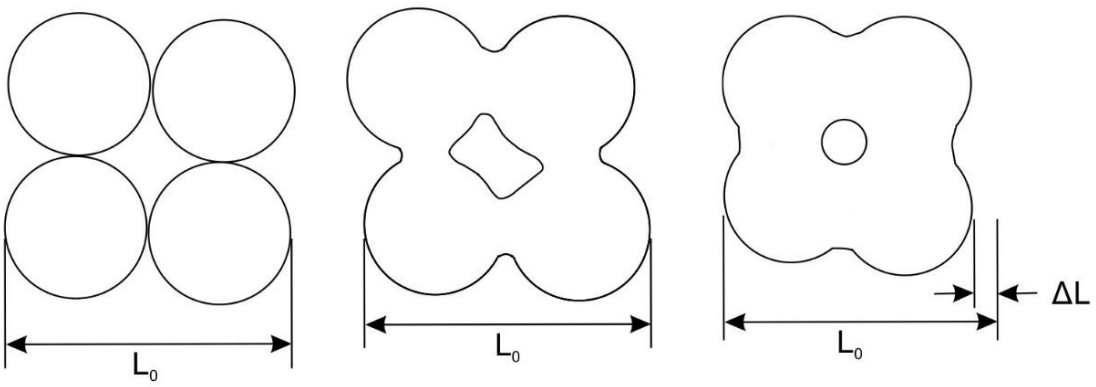

Figure 1.12: Schematic representations of (a) compact powder, (b) partial densification of neck growth, and (c) fully densified neck growth with occlusion of a pore [109].

Table 1.2: Description of sintering stages [121].

Stage	Process	Densification	Coarsening
Initial	neck growth	small at first	minimal
Intermediate	pore rounding and elongation	overall density is still low	increase in grain growth and pore size
Final	pore closure, final densification	total density advance toward a theoretical value	extensive grain and pore growth

Furthermore, the densification process during heating can be followed by measuring dimensions or density. The simplest way is to heat the compressed sample to the sintering temperature at a constant rate (usually 5 or 10 °C/min), heat it for a certain time and then cool it quickly. Following the procedure, a change in dimensions (*i.e.* relative linear shrinkage, ΔL/L; Figure 1.14) or density between the green sample (*i.e.* pre-sintering sample) and the sintered sample could be determined using a dilatometer or a heating-stage and optical microscope. The sintering diagram allows us to estimate the temperature at which sintering begins, the maximum densification rate and the optimal sintering temperature, which is usually at 75% of the maximum shrinkage [108], [122].

Density is defined by the ratio of mass to volume, $\rho = m/V$ (g/cm^3), where mass is easily measured by weighting of the sample and volume can be calculated geometrically from its dimensions or determined by displacement of liquids by the Archimedes method [27], [28], [38], [44], [123]–[127]. The ratio of measured density to theoretical density is defined as the relative density [128]:

$$\rho_{rel} = \frac{\rho}{\rho_{teor.}} \cdot 100\% \tag{1.7}$$

1.2.2 Electrical characteristics of SnO_2

1.2.2.1 Varistor applications

Varistors are the dominant components in surge protector devices. They are characterized by exceptional current-voltage nonlinearity (I-U) and the ability to absorb energy [129]. Varistors behave like insulators until the nominal breakdown voltage is reached and then suddenly (in ns) they become orders of magnitude more conductive than the electronic device they protect [95]. Their nonlinear characteristic is expressed by the equation:

$$I = K \cdot U^{\alpha} \tag{1.8}$$

where I is the electric current through the varistor, U is the applied voltage, K is the material constant and α is the nonlinear coefficient that characterizes the varistors response. Typical characteristic current-voltage curve of varistor ceramics has three important regions (Figure 1.13):

- PRE-BREAKDOWN REGION (linear, ohmic, low voltage) is the region under the breakdown voltage of the varistor. Here, the varistor has high resistance due to grain boundaries (GBs), while grains are conductive. The low current flowing through the varistor in this region is so-called leakage current (I_L) and increases linearly with voltage.
- NONLINEAR REGION is the region, where the varistor has no ohmic properties and the current increases exponentially with the voltage. Already a small change in voltage causes a large change in the current through the varistor. The nonlinearity is denoted by the nonlinear coefficient α, which is the reciprocal of the slope of the I-U curve. The greater is α, the flatter is the I-U curve in this region and the better is device. The coefficient of nonlinearity α is defined by the equation:

$$\alpha = \frac{d \log I}{d \log U} \tag{1.9}$$

- UPTURN REGION is the region of high currents ($> 10^3$ A/cm^2), where dependency between current and voltage is again linear (ohmic).

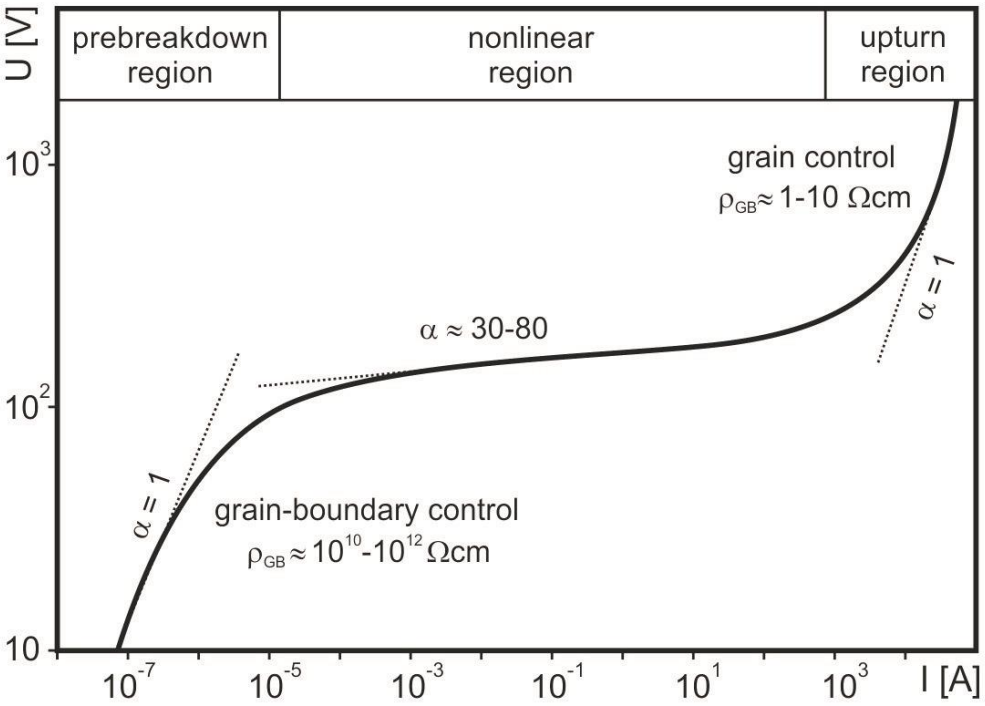

Figure 1.13: Typical characteristic current-voltage curve of varistor [95].

The typical value of nonlinear coefficient of commercial varistors is between 30 and 80, which depends on the chemical composition, temperature and process of the varistor fabrication [130]. In addition to the nonlinearity coefficient, varistors are also characterized by the nominal voltage U_N, defined as a voltage drop at 1 mA [129] which indicates a transition to the nonlinear region of the varistor. If the nominal voltage U_N(V) is divided by the thickness of the sample d (mm), the threshold voltage U_T (V/mm) of varistor ceramics is obtained. Also important is the leakage current I_L; the electrical current that flows through the varistor at the operating voltage of the device that the varistor protects. At operating voltage, the varistor should behave like an ideal resistor. The leakage current is important because of the loss of power ($I_L^2 \cdot R$), which is reflected in the elevated temperature of the varistor and in determining the voltage range of operation at which the varistor does not heat up [129].

Commercial varistors are commonly based on ZnO ceramics, first recognized by Matsouka *et al.* in Japan, early in the 1970s [131]. Microstructurally, ZnO varistors consist of highly conductive uniformly sized ZnO grains, separated by highly nonconductive nonlinear varistor-type GBs to produce the so-called varistor effect [95], [129]–[131]. In ZnO-based varistors, ZnO is predominantly with small additions of other oxides, like Bi_2O_3, Sb_2O_3, CoO, Cr_2O_3 and MnO, whose overall additions are usually 3-5 mol% [42], [70], [131], [132]. For varistor properties (I-U nonlinearity) Bi_2O_3 is crucial (also Pr_6O_{11} or BaO), which causes the formation of electrostatic Schottky barriers at the boundaries between ZnO grains. At the same time, Bi_2O_3 causes the formation of a liquid phase, which greatly influences the growth of ZnO grains and the development of a microstructure of varistor ceramics. ZnO doped with Bi_2O_3 already has varistor properties, other oxides further improve the nonlinear properties. In general, varistors with a larger average grain size are used for low-voltage applications, when those with a smaller average grain size are used for high-voltage applications as seen in Figure 1.14 [95].

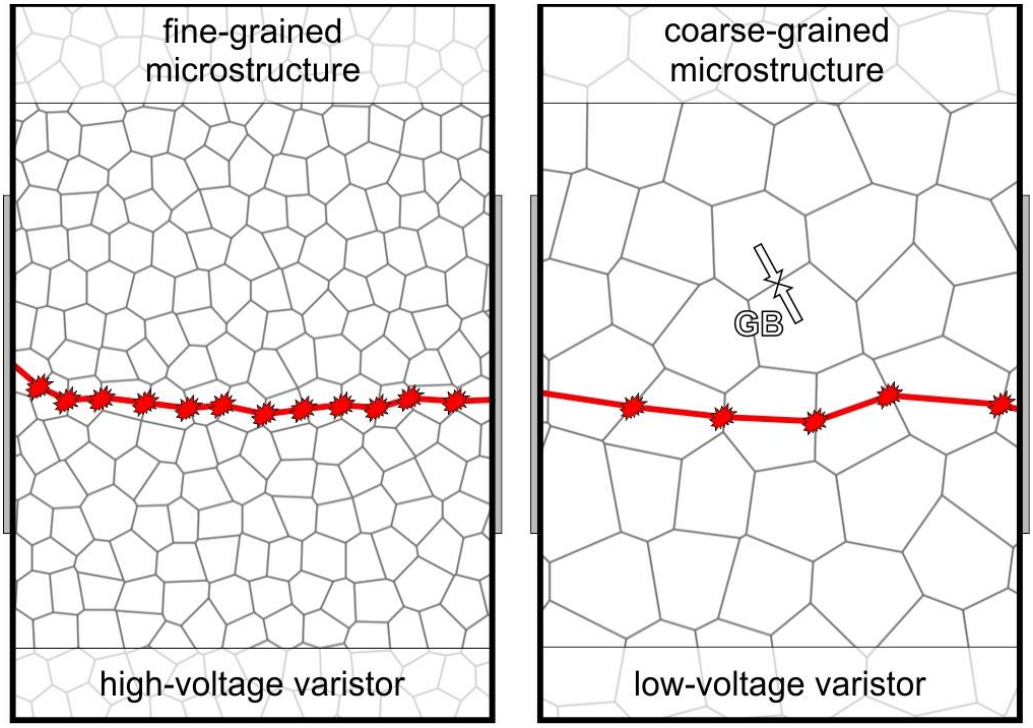

Figure 1.14: Schematic presentation of a) a coarse-grained microstructure for low-voltage varistor application, and b) a fine-grained microstructure for high-voltage applications [95].

With respect to alternative ceramic systems, studies of several oxides such as TiO_2, $SrTiO_3$, CeO_2, WO_3, $ZnSnO_3$, $BaTiO_3$, and SnO_2 have been performed [114], [133]–[138]. In 1995, the first study of a highly nonlinear varistor SnO_2-CoO-Nb_2O_5-Cr_2O_3 ($\alpha = 41$) was reported by Pianaro *et al.* [20]. Since then, SnO_2 ceramics have become a promising candidate for commercial varistor application with comparable parameters of multicomponent ZnO varistors [71], [72]. The main advantages of the SnO_2 varistor system over the ZnO-based elements is its simple, uniform microstructure (Figure 1.15 b), lower dopant additions (usually 1-2 mol%), where already two dopants are sufficient to obtain excellent electrical properties, up to two times higher thermal conductivity, better temperature resistance and significantly fewer secondary phases. Consequently, this increases the fraction of active grain boundaries up to 85 % [42], [70], [71], [139]. In comparison, ZnO-based varistors have only 15-33% of active GBs due to inhomogeneous multi-phase (Bi-rich phases, spinel and pyrochlore phases) microstructure (Figure 1.15 a) [140], which leads to degradation phenomena and deterioration of varistor properties [112], [141], [142]. However, despite two main disadvantages of SnO_2-based varistors, which are approximately 200 °C higher processing temperature due to solid-state sintering (for ZnO-based varistors liquid-phase sintering is common) and relatively high cost of SnO_2 raw material, its outperforming electrical characteristics explains a wide interest in this material.

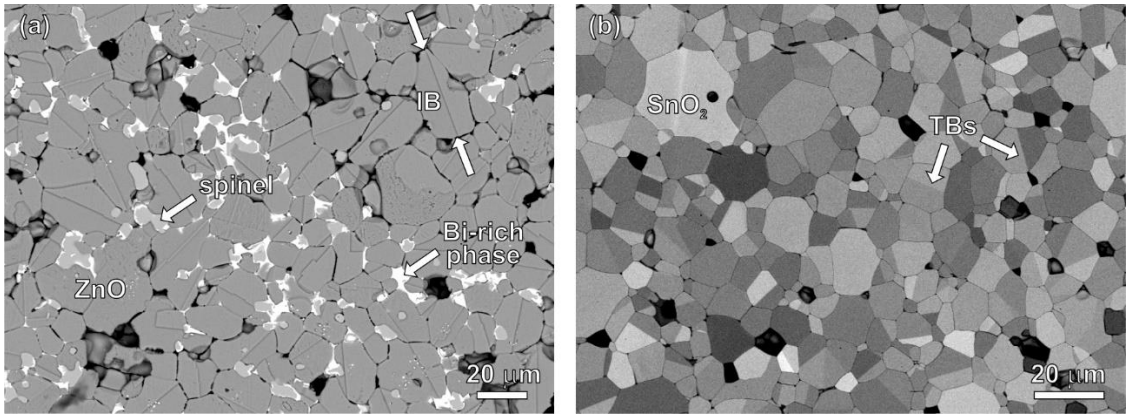

Figure 1.15: Typical microstructures of ZnO-based and SnO_2-based varistor ceramics: a) a complex microstructure of ZnO grains, assisted by Bi-rich phase and spinel particles [95], b) a simple microstructure of SnO_2 grains without any secondary phase.

1.2.2.1.1 Point defects in SnO_2-based ceramics

Microstructure evolution in doped SnO_2-based ceramics is usually interpreted as a solid-state sintering process, controlled by point defects formation [20]. Pure SnO_2 has a poor densification rate and grain growth during sintering due to the predominance of non-densifying mechanisms, such as surface diffusion at low temperatures (T < 1300 °C) [37], [143] and evaporation-condensation mechanism at high temperatures (T> 1300 °C), proposed by Kimura *et al.* [69] and Varela *et al.* [36]. In order to understand the sintering mechanism, Hoenig and Searcy [35] examined the process of SnO_2 evaporation and found that at high temperatures this oxide decomposes by the following reaction:

$$SnO_2(s) \rightleftharpoons SnO\ (g) + \tfrac{1}{2}\ O_2\ (g) \tag{1.10}$$

Further, the evaporation of tin (II) oxide can be described by the formation of oxygen vacancies, $V_O^{\cdot\cdot}$:

$$SnO \xrightarrow{SnO_2} Sn(II)''_{Sn(IV)} + V_O^{\cdot\cdot} + O_O^{\times} \tag{1.11}$$

Although high porosity of SnO_2 ceramics is required in sensor applications [5], [65], [134], [144]–[147], this characteristic is not desirable in varistor applications and density should be increased with the addition of acceptor dopants, such as CuO, ZnO, MnO_2, Bi_2O_3 and CoO that form solid solution with SnO_2 [41], [44], [74], [123], [126], [148]–[151]. The role of Bi_2O_3-liquid phase is less studied in SnO_2-based ceramics, but it is known that this dopant can enhance grain growth during the sintering [73], [74]. Despite the absence of a eutectic liquid phase in the CoO-SnO_2 system, CoO is the most efficient acceptor dopant with a similar ionic radius to Sn^{4+} ($r(Sn^{4+})$ = 0.071 nm; $r(Co^{2+})$ = 0.074 nm), which facilitates CoO to form a solid solution and increases densification of SnO_2 to 99% of theoretical density [20], [39], [123]. With the addition of 2 mol% CoO to the SnO_2 ceramics, Cerri *et al.* [123] observed oxidizing effect of CoO during heating up to 680 °C, followed by the reducing effect at temperature above 950 °C, as written below:

$$2\ CoO + \tfrac{1}{2}\ O_2 \xrightarrow{300-680\ ^\circ C} Co_2O_3 \xrightarrow{950\ ^\circ C} 2\ CoO + \tfrac{1}{2}\ O_2 \tag{1.12}$$

Highly densified SnO_2 ceramics, doped with CoO at high sintering temperatures and low heating/cooling rates can be explained by the substitution of Sn^{4+} ions with Co^{2+} ions, which produces an increase in the oxygen vacancy concentration ($V_O^{\cdot\cdot}$). These oxygen vacancies facilitate the grain growth through a solid-state diffusion mechanism according to the following chemical equation, written in the Kröger-Vink notation [20], [23], [39], [40], [110], [123], [126]:

$$CoO \xrightarrow{SnO_2} Co''_{Sn(IV)} + V_O^{\cdot\cdot} + O_O^{\times} \tag{1.13}$$

$$Co_2O_3 \xrightarrow{SnO_2} 2\ Co'_{Sn(IV)} + 2\ V_O^{\cdot\cdot} + 3\ O_O^{\times} \tag{1.14}$$

The increase in oxygen vacancy concentration requires that the concentration of free electrons decreases due to the equilibrium between solid and gas at a given partial pressure of oxygen [41], [152]:

$$O_O^{\times} \rightleftharpoons \tfrac{1}{2}\ O_2\ (g) + 2\ e' + V_O^{\cdot\cdot} \tag{1.15}$$

Co atoms also segregate at GBs, which is very important for defining the non-ohmic behavior [145]. However, the nonlinear coefficient of Co-doped SnO_2 ceramics is still low and this ceramic behaves as an electrical insulator since grains are highly resistive [123], [143], [145]. For the electrical properties, it has been reported that a suitable addition of donor dopants (the most common are pentavalent dopants Ta_2O_5, Nb_2O_5 and Sb_2O_5) reduced the porosity (indicating that SnO evaporation is suppressed [36]) and significantly increased the electrical conductivity of SnO_2-based ceramics [20], [21], [28], [41], [42], [110], [138], [143], [150], [153]. The substitution of Sn^{4+} by Nb^{5+}, Ta^{5+} or Sb^{5+} results in the formation of Sn-site vacancies, V_{Sn}'''', that compensate two oxygen vacancies, $V_O^{\cdot\cdot}$, and leads to an increase in free electron concentration in tin oxide which, in turn, increases the electrical conductivity of the SnO_2 lattice, as written in the following compensation mechanism [23], [40], [41], [143], [145]:

$$2\ Nb_2O_5 \xrightarrow{SnO_2} 4\ Nb(V)_{Sn(IV)}^{\cdot} + V_{Sn}'''' + 10\ O_O^{\times} \tag{1.16}$$

$$V_{Sn}'''' + 2\ V_O^{\cdot\cdot} \rightarrow 2\ V_O^{\cdot} + V_{Sn}'' \tag{1.17}$$

Further, with higher concentration of dopants, Branković *et al.* [41] suggested that dopants are not incorporated into the SnO_2 lattice only by substitution, but also at interstitial positions. This results in the increase of lattice constant values and decrease of oxygen vacancies, as indicated by the following mechanism:

$$2\ CoO \xrightarrow{SnO_2} 2\ Co_i^{\cdot\cdot} + 2\ O_O^{\times} + V_{Sn}''''$$ (1.18)

Similar equation can be written for donor dopant, for example Nb^{5+}. Since no secondary phase occurs at the grain boundaries in SnO_2 ceramics, defects caused by acceptor and especially by donor dopants are responsible for enhanced formation of potential barriers and increased amount of active grain boundaries [39], [45], [154]. Potential barriers in SnO_2 varistors are the same as in ZnO, both possessing Schottky electrical barriers at the GBs that exhibit high resistivity related to the conducting nature of the intragranular ceramic [39], [70]. Oxygen is responsible for the formation of the Schottky barrier, as O' and O'' are the main absorbed species at the grain boundaries (at T above 200 °C) [40], [110].

1.2.2.1.2 Atomic defect model for SnO_2 varistor

To explain the phenomenon of voltage instability/stability of the varistor under an externally applied electric field, Gupta and Carlson proposed an atomic defect model for the grain-boundary barrier for ZnO varistor. In this model, the authors emphasize the importance of zinc interstitials, which are formed as excess zinc in the depletion layer, due to the inherent nonstoichiometric nature of ZnO. The presence of these interstitials in the barrier and field-assisted diffusion of the interstitials in the depletion layer are the main cause of varistor instability. To restore stability, it is necessary to form a stable ZnO lattice at grain boundaries at the expense of Zn interstitials by heat treatment. In addition, the negative surface charge layer at the grain boundary is balanced on both sides by the positive depletion layer comprising the barrier consisting of a stable component (spatially fixed positively charged substituted ions and vacancies, located on the lattice sites) and a metastable component (mobile positively charged zinc interstitials on the interstitial sites in the ZnO structure)[155].

Based on the atomic defect model for ZnO-based varistors, in 1998, Pianaro *et al.* proposed the atomic model of a SnO_2-based varistor, as shown in Figure 1.16. In this model, like the previous one, a high concentration of negative charge at the SnO_2 grain surface is shown, which is caused by tin vacancies ($V_{Sn}^{''''}$) and the substitution of tin ions with cobalt ions ($Co_{Sn}^{''}$) at the interface. These negative charges, however, are balanced by positive charges from the depletion layer region, with barrier width ω. Positive charges can be oxygen vacancies ($V_O^{\cdot\cdot}$), interstitial tin ions ($Sn_i^{\cdot\cdot}$), as well as pentavalent substitution ions called donor ions ($D_{Sn}^{\cdot}$) [39].

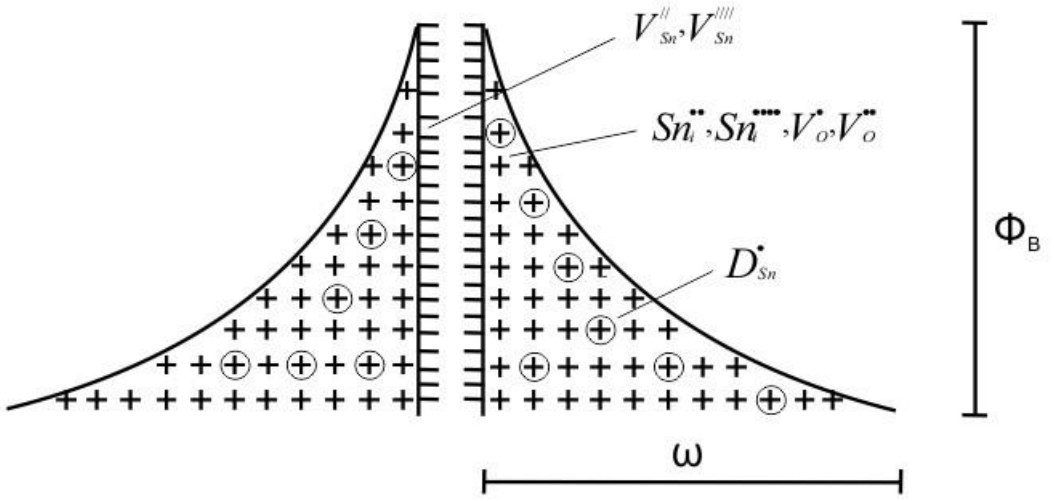

Figure 1.16: Atomic defect model for Schottky barrier at the SnO_2 grain boundaries [39].

1.2.2.1.3 SnO_2-CoO-Nb_2O_5 ceramic system

The first report of SnO_2-CoO-Nb_2O_5 varistor ceramics was made in 1995 by Pianaro *et al.* [20]. With the addition of 0.5 mol% of Nb_2O_5 to the SnO_2-1 mol% CoO system, they intended to reach a highly resistive behavior. As this system alone showed only a weak nonlinear behavior ($\alpha = 8$, $E_b = 1800$ V/cm), high nonlinear behavior ($\alpha = 41$, $E_b = 3990$ V/cm) was achieved by the addition of 0.05 mol% Cr_2O_3 to this system [156]. At high resolution, only a small amount of secondary Co_2SnO_4 phase was observed in the SnO_2-1 mol% CoO samples, formed by solid state precipitation at grain boundaries. Since the solubility limit of CoO in SnO_2 is 0.5 mol%, an excess of CoO caused precipitation of

Co_2SnO_4, while no Co was detected in SnO_2 grains [123], [157]. However, it is not entirely clear whether the addition of Nb_2O_5 dopant increases or decreases the formation of Co_2SnO_4 secondary phase. Fayat *et al.* [23] reported that the addition of Nb_2O_5 favors the formation of Co_2SnO_4 particles that could control the sintering and grain growth rate, whereas Bueno *et al.* [42] reported that Nb_2O_5 doping reduces the precipitation of secondary phases at grain boundaries. Chang *et al.* [44] suggested that secondary phase might not play an important role in grain growth and disappeared with the addition of Nb_2O_5 dopant due to the charge compensation between $Co''_{Sn\,(IV)}$ and $Nb(V)^{\cdot}_{Sn\,(IV)}$.

(Co, Nb)-doped SnO_2-based ceramics are commonly suitable for high-voltage varistor applications [20], [156], [158], [159], while it is more difficult to obtain SnO_2-based ceramics for low-voltage varistors with a sufficiently high nonlinearity coefficient. At relatively low currents (~1 mA/cm^2), the grain boundaries in SnO_2-based varistor ceramics are essentially more resistant than the grains themselves. Additional doping of this ternary system with dopants, such as Cr_2O_3 [156], Fe_2O_3 [158], Pr_2O_3 [159] and Sm_2O_3 [27], inhibits grain growth, while the dopants segregate at the GBs. Recently, it was shown that high nonlinearity at relatively low electric fields can be achieved with the addition of Bi_2O_3 to the SnO_2–CoO–Nb_2O_5 or SnO_2–CoO–Nb_2O_5–Cr_2O_3 compositions [73], [160]. Therefore, electrical conductivity of the material can be controlled by grain boundaries and the observed decrease in electric field can be explained by the enhanced growth of SnO_2 grains in the presence of a liquid Bi-rich phase. This was also confirmed by the strong increase in the relative dielectric permittivity due to grain boundaries number decrease [73], [74]. Moreover, Bondarchuk *et al.* [28] systematically studied the various effects of Nb_2O_5 dopant on the grain growth and electrical properties of the SnO_2–CoO–Cr_2O_3–Bi_2O_3 ceramic system. While already a small amount of Nb enhances the Sn self-diffusion, improves the grain growth and increases the electrical conductivity, higher concentrations of Nb (0.5 and 1 mol %) have only little effect on the electron concentration in the volume of SnO_2-grains, as it segregates mainly at the GBs [28]. As a result, the height of the potential barrier does not change drastically with increased Nb-doping and leads to a decrease in the electrical conductivity of a material.

In contrast to the previous study [28], I showed that a certain amount of the Nb_2O_5 dopant ($\leq$ 1 mol%) increases the conductivity of grains and thus the height of the electrostatic barrier at the grain boundaries as well their resistivity (*i.e.* break- down voltage). I investigated the effects of Nb-doping in a simple ternary system SnO_2-CoO-Nb_2O_5 at relatively high temperatures (where the decomposition of SnO_2 is significant), without the presence of liquid phase during sintering. XRD and EDS analyses showed that Nb_2O_5 doping inhibits the formation of the secondary phase, while the amount of CoO in SnO_2 grains increases along with Nb [75]. I successfully obtained SnO_2-CoO-Nb_2O_5 ceramics for high-voltage varistor applications with comparable electrical parameters of ZnO-based ceramics (more in *Chapter 3*).

1.2.2.1.4 SnO_2-CoO-Ta_2O_5 ceramic system

In 1998, Antunes *et al.* [21] published *Nonlinear electrical behavior of the SnO_2·CoO · Ta_2O_5 system*, comparing its electrical properties to Nb, Co - doped SnO_2 [20]. The authors studied low (0.05 and 0.075 mol%) additions of Ta_2O_5 to the SnO_2-CoO system, which improved electrical conductivity of SnO_2 (α = 13), while the effect of higher additions of Ta_2O_5 dopant (< 0.1 mol%) has not been investigated. Furthermore, Wang *et al.* [111] investigated effects of higher additions of Ta_2O_5 on the grain size in the SnO_2-Co_2O_3 system and achieved promising electrical characteristics with the addition of 1 mol% of Ta_2O_5, suggesting that an increase of Ta_2O_5 decreases the grain size due to Ta segregation at the

grain boundaries. As oxygen vacancies are a particularly important factor in controlling the grain growth, any addition of Ta instantly decreases the concentration of oxygen vacancies and consequently Ta acts as a grain growth inhibitor, which in turn increases the electronic conductivity in the SnO_2 lattice.

Varistor properties of the SnO_2-CoO-Ta_2O_5 ceramic system can be enhanced by an alkali earth elements (Ba/Sr [161]) or with the presence of liquid phase (B_2O_3 addition [162]). Rare-earth oxides (Pr_2O_3, Pr_6O_{11}, La_2O_3) are also often used to improve the electrical properties of this ceramic system, as they can strongly influence the development of microstructures by decreasing the size of SnO_2 grains [42], [138], [163]. However, it is difficult to fabricate fully densified SnO_2-CoO-Ta_2O_5 ternary ceramics by conventional sintering methods, partly due to the decomposition and evaporation of SnO at high sintering temperatures and decreasing concentration of oxygen at grain boundaries on cooling [69], [123], [164]. To replace conventional sintering, in recent years, spark plasma sintering has been successfully used to produce dense SnO_2 ceramics at relatively lower temperatures and significantly shorter sintering times [117]–[119]. Using the SPS technique and systematically varying the sintering temperature, heating rate, holding time at the sintering temperature and the amount of Ta_2O_5 dopant, Yoshida *et al.* [118] produced dense Ta-doped SnO_2 compacts. Although high densification for SnO_2-based ceramics was achieved using SPS, a metastable $Sn_2Ta_2O_7$ compound was formed from a mixture of SnO_2 and Ta_2O_5, leading to high structural inhomogeneity. Chen *et al.* [113] also reported that the residual carbon is detected in the ceramics even after post-annealing.

The aim of this doctoral thesis was to achieve fully dense (Co,Ta)-doped SnO_2 ceramics for low-voltage varistor applications, with a special focus on microstructure development, electrical characteristics and charge compensation mechanism (more in *Chapters 4 and 5*).

1.2.2.2 Dielectric properties

The dielectric permittivity and dielectric loss measurements are based on the measurement of impedance, which is just an extension of the concept of electrical resistance from direct current (DC) to an alternating current (AC). The impedance of the resistor is thus quite equal to his resistance, while the impedance of the capacitor depends on its capacitance, the frequency where the measurement is performed as well on the losses, denoted by tan δ. The dielectric behavior of ceramics powder can be measured in a capacitance cell, consisting of two electrodes of a parallel plate, where A is the pellet cross-sectional area, d is the sample thickness and C is measured capacity. The oscillating field is applied to the sample in a wide frequency range. The dielectric permittivity (ε) can be calculated from the capacitance (C) of an ideal capacitor, according to the equation [165]:

$$\varepsilon_r = \frac{\mathrm{C}\cdot\mathrm{d}}{\mathrm{A}\cdot\varepsilon_0} \tag{1.19}$$

where ε_0 is permittivity of a vacuum ($\varepsilon_0 = 8.854 \cdot 10^{-12}$ F/m) and ε_r is the relative permittivity of the samples, respectively. Dielectric behavior of the synthesized ceramic powder can be explained by phenomenon od frequency dispersion. The dielectric loss (tan δ) and dielectric permittivity of the sample decreases with an increase of a frequency and consequently AC conductivity increases. At lower frequencies (up to 1 kHz), rapid decrease of ε value is more noticeable due to the movement of charge carriers trapped at interfacial region than at higher frequencies, where the dominant mechanism is hopping of charges. The essence of this model is that the frequency of hopping between ions cannot follow the frequency of applied field and therefore lags behind, so the value of ε slowly decreases [166]–[168]. In recent years, several reports of high permittivity behavior of varistor ceramics have been published. High dielectric properties are attributed to the Schottky

barriers, which consist of negative trapped charges and positive depletion layer (*see* Figure 1.16). Doping SnO_2 ceramics with CoO and Cr_2O_3 as acceptor dopant, leads to the formation of barriers (with increasing the $V_O^{\cdot\cdot}$ concentration) to improve the SnO_2 varistor system. The increase in resistance (decrease in conductivity) is enhanced by the addition of a pentavalent donor dopant (such as Nb_2O_5, Ta_2O_5, Sb_2O_5), which introduces many n-type carriers, while an acceptor dopant (*e.g.* Co) can capture the electrons introduced by donor doping. The fact that the large permittivity of the ceramics comes from the resistivity of SnO_2 grain boundary layers and the minor intergranular region, increasing the addition of donor dopant has a negative effect on the dielectric permittivity value due to a significant decrease of the grain size [138], [165]–[167], [169], [170] .

The dielectric measurements of (Co, Nb/Ta)-doped SnO_2 ceramics of this doctoral dissertation were done in collaboration with colleagues from the Advanced Materials Department (K9) from the Jožef Stefan Institute. Before dielectric measurements, silver electrodes were deposited on both sides of sintered pellets. Dielectric properties were calculated from the impedance measurements of the samples, using LCR meter (Model 4284A; Hewlett-Pachard, USA) with desired input signal voltage (1 V) and desired frequencies (20 Hz-1 MHz) at room temperature.

Chapter 2

Aims and Hypothesis

While SnO_2 has a superb combination of chemical, electrical and optical properties, it is still little known about how the presence of planar defects, produced with the addition of specific dopants, affects microstructure development and related physical properties. Previous studies of SnO_2 ceramics have shown that under some conditions SnO_2 is heavily twinned [46], [47] and as we know from other materials, such as ZnO [95], [101]–[106] and TiO_2 [96], [98]–[100], special boundaries play a decisive role in grain growth and microstructure development. In order to test this hypothesis, I investigated SnO_2 ceramics with specific twin-forming dopants to explore their influence on microstructure development and to confirm whether the twinning in SnO_2 might be chemically induced. Furthermore, my research will serve as a good starting point for future studies on the presence of planar defects and their role in electrical properties of these materials.

2.1 Objectives

The main aim of my dissertation was to investigate the role of twinning in doped SnO_2-based ceramics, and its relation to grain growth, microstructure development and electrical properties for surge protection applications. In order to study these effects, I choose two ternary systems: SnO_2-CoO-Nb_2O_5 and SnO_2-CoO-Ta_2O_5, allowing to study the effects of acceptor (*i.e.* Co) and donor dopants (*i.e.* Nb/Ta). The main challenge was to reproduce twinning in SnO_2 under control laboratory conditions and to resolve ionic charge compensation mechanisms for both SnO_2 ternary systems. Studied materials were optimized with respect to their bulk varistor and dielectric properties.

Accordingly, I defined three main objectives:

I. **Twinning in SnO_2-based ceramics:** To determine what causes the twinning in SnO_2 and to investigate its direct effect on microstructure development and electrical properties my work was focused on the following questions:

   - *What is the role of twin boundaries in microstructure development and electrical properties in SnO_2-based ceramics?*
   - *What is the role of donor dopant addition on the twin boundary formation?*

II. **Formation of point defects and charge compensation mechanisms in SnO_2:** Pure SnO_2 does not densify well at high temperatures, where tin (IV) is reduced to tin (II) that evaporates from the system. To stabilize the SnO_2 surface structure, it is necessary to add acceptor dopant (*e.g.* Co), while the addition of

donor dopants (*e.g.* Nb/Ta) improves electrical characteristics of ceramics. However, to achieve equilibria of point defects, a balanced addition of donor and acceptor dopants is required. Accordingly, I have attempted to answer the following unsolved questions:

- *What is the solid solubility limit of Co dissolved in SnO_2 grains?*
- *How the amount of incorporated Co changes with the addition of donor (Nb/Ta) dopants?*
- *What is the ionic charge compensation mechanism for both systems? Is it the same?*

III. **Optimization of varistor and dielectric properties in SnO_2-based ceramics:** Defect formation by acceptor and donor additives in SnO_2 ceramics is responsible for the origin of the Schottky barriers at grain boundaries, therefore the electric conductivity can be greatly increased with Nb_2O_5 or Ta_2O_5 additions. Here I focused on determining the conditions for achieving SnO_2-based ceramics with optimal electric and dielectric properties. Accordingly, I have attempted to answer the following unsolved questions:

- *How does the addition of donor dopants (Nb_2O_5 or Ta_2O_5) affect the average grain size and SnO_2 microstructure development?*
- *How does this affect the electrical characteristics, including conductivity, nonlinear coefficient and breakdown voltage?*
- *What is the correlation between the grain size and the electrical characteristics of SnO_2 ceramics?*
- *How does the addition of acceptor and donor dopants influence the dielectric permittivity and dielectric losses?*
- *What are the conditions for optimal varistor and dielectric properties?*

2.2 Outline of Results

I. Twinning in SnO_2-based ceramics

To answer these questions, I first synthesized SnO_2-based ceramics doped with the addition of CoO (1 mol%) and different concentrations of Nb_2O_5 (0.1-2 mol%). To find the optimal sintering temperature and sintering time I measured densification characteristics of SnO_2-based ceramics. Then I identified the phase compositions and determined the relative densities of all samples by XRD and Archimedes method, respectively. The sample with the addition of 1 mol% Nb_2O_5 showed the most promising characteristics, with its 99% of the theoretical density and excellent electrical properties. Using transmission electron microscopy, I have shown that the predominant type of twins in SnO_2 is {101} and that cyclic twins are also common. Further study with high-angle annular dark-field scanning transmission electron microscopy has shown that the twin boundaries are not directly induced by the addition of Nb_2O_5 (chemically induced) but are most likely the result of yet unexplained sequence of topotaxial replacement reactions. Thus, I continued my research, where I replaced donor dopant (Ta_2O_5 instead of Nb_2O_5). The increase in Ta_2O_5 addition also resulted in abundant twinning, and like in Nb_2O_5 doping, also here the cyclic twins were common. Using TEM I confirmed that TBs lie in {101} planes of SnO_2, while EDS analysis did not show any excess of dopant at the TB planes, again indicating that the twinning in SnO_2 is not chemically induced, as IBs in ZnO. More details are given in Chapters 3-4 and research articles:

- S. Tominc, A. Rečnik, Z. Samardžija, G. Dražić, M. Podlogar, S. Bernik, N. Daneu, "Twinning and charge compensation in Nb_2O_5-doped SnO_2-CoO ceramics exhibiting promising varistor characteristics", *Ceramics International*, vol. 44, no. 2, pp. 1603-1613, 2018, doi: 10.1016/j.ceramint.2017.10.081.
- S. Tominc, A. Rečnik, S. Bernik, M. Mazaj, N. Daneu, "Charge compensation and electrical characteristics of Ta_2O_5-doped SnO_2-CoO ceramics", *Journal of European Ceramic Society*, vol. 40, no. 2, pp. 355-361, 2020, doi: 10.1016/j.jeurceramsoc.2019.09.028.

II. Formation of point defects and charge compensation mechanisms in SnO_2

With quantitative TEM/EDS analysis I demonstrated that the amount of dissolved CoO in SnO_2 grains varies, but is always approximately four times lower than the amount of incorporated Nb. Based on this observation I proposed a charge compensation mechanism for the SnO_2-CoO-Nb_2O_5 system, which with respect to previous studies [20], [22], [39], [41], [110] involves Sn^{2+} species. Further, I studied charge compensation mechanism in isovalent Ta_2O_5, where I have shown that a twice lower amount of donor dopant (Ta^{5+}) is incorporated into the SnO_2 structure along with Co^{2+}, compared to the Nb_2O_5-doped SnO_2-CoO system [75], indicating that here, another charge compensation mechanism is at play that does not involve Sn^{2+}. I proposed a new charge compensation mechanism for both systems. More details on this objective are addressed in Chapters 3-4 and articles:

- S. Tominc, A. Rečnik, Z. Samardžija, G. Dražić, M. Podlogar, S. Bernik, N. Daneu, "Twinning and charge compensation in Nb_2O_5-doped SnO_2-CoO ceramics exhibiting promising varistor characteristics", *Ceramics International*, vol. 44, no. 2, pp. 1603-1613, 2018, doi: 10.1016/j.ceramint.2017.10.081.
- S. Tominc, A. Rečnik, S. Bernik, M. Mazaj, N. Daneu, "Charge compensation and electrical characteristics of Ta_2O_5-doped SnO_2-CoO ceramics", *Journal of European Ceramic Society*, vol. 40, no. 2, pp. 355-361, 2020, doi: 10.1016/j.jeurceramsoc.2019.09.028.

III. Optimization of varistor and dielectric properties in SnO_2-based ceramics

SnO_2-CoO ceramics alone, shows a relatively high resistance, as the majority of added CoO is segregated to the GBs. This is expressed in a low nonlinear coefficient and low threshold voltage, indicating a weak varistor behavior. On the other hand, the dielectric permittivity is relatively high ($\varepsilon = 2675$) and the dielectric loss is low (0.085 at 1 kHz). However, only a small addition of donor dopant (0.1 mol% of Nb_2O_5) results in 2-3 times larger average grain size, 2 times higher dielectric constant and halved dielectric loss than SnO_2-CoO ceramics, while still showing a weak varistor behavior. Threshold voltage and nonlinear coefficient increase with the addition of donor dopants, achieving its peak at 1 mol% of Nb_2O_5. On the other hand, the dielectric permittivity decreases ($\varepsilon < 1000$) and the dielectric losses increase. Higher additions of Nb_2O_5 (2 mol%) causes varistor deterioration.

Based on SnO_2-CoO-Nb_2O_5 ternary system, I prepared SnO_2 ceramics with CoO and Ta_2O_5 additions. We found that Ta^{5+} and Co^{2+} produce a constant 2:1 ratio (compared to the Nb^{5+}/Co^{2+} ratio of 4:1), which indicates that a lower amount of Ta^{5+} is incorporated into the SnO_2 structure. To increase the efficiency of this system, the addition of CoO was changed to 1-4 mol%, the maximum density was obtained with 4 mol% CoO for all Ta_2O_5

additions (0.05-2 mol %). By increasing the amount of CoO, I achieved the condition of rapid grain growth in SnO_2 ceramics. I showed that small additions (0.05 and 0.10 mol%) of Ta_2O_5 to the SnO_2 – 4mol% CoO system increase both the density and growth of SnO_2 grains. The sample with the addition of 0.10 mol% Ta_2O_5 had the largest average grain size and the best dielectric properties. In contrast, the sample with 4 mol% CoO and 1 mol% Ta_2O_5 showed the highest density and fine grain size, which was reflected in unprecedented varistor properties. Details on this objective are addressed in Chapters 3 and 5 and articles:

- S. Tominc, A. Rečnik, Z. Samardžija, G. Dražić, M. Podlogar, S. Bernik, N. Daneu, "Twinning and charge compensation in Nb_2O_5-doped SnO_2-CoO ceramics exhibiting promising varistor characteristics", *Ceramics International*, vol. 44, no. 2, pp. 1603-1613, 2018, doi: 10.1016/j.ceramint.2017.10.081.
- S. Tominc, A. Rečnik, S. Bernik, M. Mazaj, M. Spreitzer, N. Daneu, "Microstructure development in (Co,Ta)-doped SnO_2-based ceramics with promising varistor and dielectric properties", *Journal of European Ceramic Society*, vol. 40, no. 15, pp. 5518-5522, doi: 10.1016/j.jeurceramsoc.2020.03.062.

Chapter 3

Twinning and Charge Compensation in Nb_2O_5–Doped SnO_2–CoO Ceramics Exhibiting Promising Varistor Characteristics

Nowadays, the production of varistors is based on ZnO ceramics, where it has been shown that the formation of planar defects (IBs) in ZnO grains, triggered by certain dopants, plays a decisive role in microstructure development and to a great extent tailor varistors electrical properties [103], [105], [171], [172]. In the last 25 years, however, numerous studies of SnO_2 varistor ceramics have been developed [20]–[28]. The main advantages of SnO_2-based ceramics over ZnO-based ceramics are significantly lower addition of dopants, uniform microstructure without secondary phases, better thermal conductivity and temperature resistance. Since undoped SnO_2 does not densify well at high temperatures due to surface reduction and evaporation of SnO [35], its structure is best stabilized by doping. On the other hand, there are several reports in the literature that SnO_2 is prone to twinning upon doping [24], [46]–[48], however the effect of twin boundaries on grain growth and electrical properties has never been assessed in a SnO_2-based varistor system. Common to these studies is that:

- acceptor dopants (*e.g.* CoO) enhance densification of SnO_2 and trigger the formation of oxygen vacancies,
- donor dopants (*e.g.* Nb_2O_5) improve the electrical conductivity of SnO_2 by forming free electrons in the lattice, while inhibiting grain growth,
- a small addition of pentavalent dopants triggers twinning in SnO_2.

In this Chapter, I wanted to determine the influence of donor dopant (Nb_2O_5) on the microstructure development, formation of TBs and electrical / dielectric properties. The key processes that are important in this study are:

I. Densification behavior

According to the literature, compositions with fixed addition of CoO (1 mol%) and different additions of Nb_2O_5 (0.1 - 2 mol%) were determined. Using a heating-stage microscope, I determined the optimal sintering temperature at which the maximum densification rate was achieved (*see* Figure 3.1.) and measured the relative densities of the samples.

Depending on the addition of Nb_2O_5, a remarkable effect on the degree of porosity was observed.

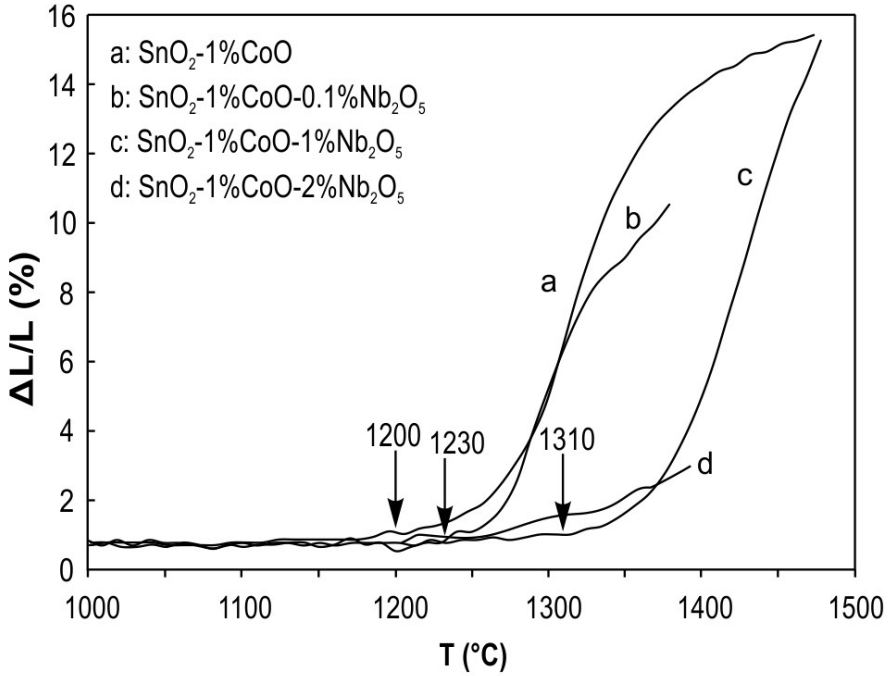

Figure 3.1: Linear shrinkage (ΔL/L) with respect to temperature for different dopant concentrations in SnO_2 ceramics. Curve **a** shows SnO_2 sample doped with Co only, starting to densify at ~1200 °C. With the addition of 0.1 mol% Nb_2O_5, the onset of densification appears at ~ 1230 °C (curve **b**), while with the addition of 1 mol% of Nb_2O_5 (curve **c**), densification starts at ~ 1315 C, with the maximum rate achieved at 1430 °C. With higher addition of Nb_2O_5 (2 mol%), densification appears at even higher T (curve **d**), but due to the limitation of the heating-stage microscope (its use is restricted to T up to 1450 °C) cannot be determined precisely.

II. Grain growth and varistor performance

In this study, I have shown that even a small addition of Nb_2O_5 (0.1 mol%) to the SnO_2-CoO binary system is sufficient to triple the average grain size and to halve the porosity. The maximum dielectric permittivity was also determined for this sample. Furthermore, with equimolar addition of CoO and Nb_2O_5 we prevent tin out-diffusion and the sample almost achieved theoretical density. This results in dense microstructure with excellent varistor performance in the most applicable voltage range, having excellent current-voltage nonlinearity expressed in the high coefficient of nonlinearity (α=50) and an exceptionally low leakage current (I_L=2-4 μA).

III. Twin boundary formation

I have shown that charge compensation mechanisms that take place upon the addition of aliovalent dopants trigger the formation of multiple and single twin boundaries in SnO_2 grains (Figure 3.2). Their effect on microstructure development is explained as well.

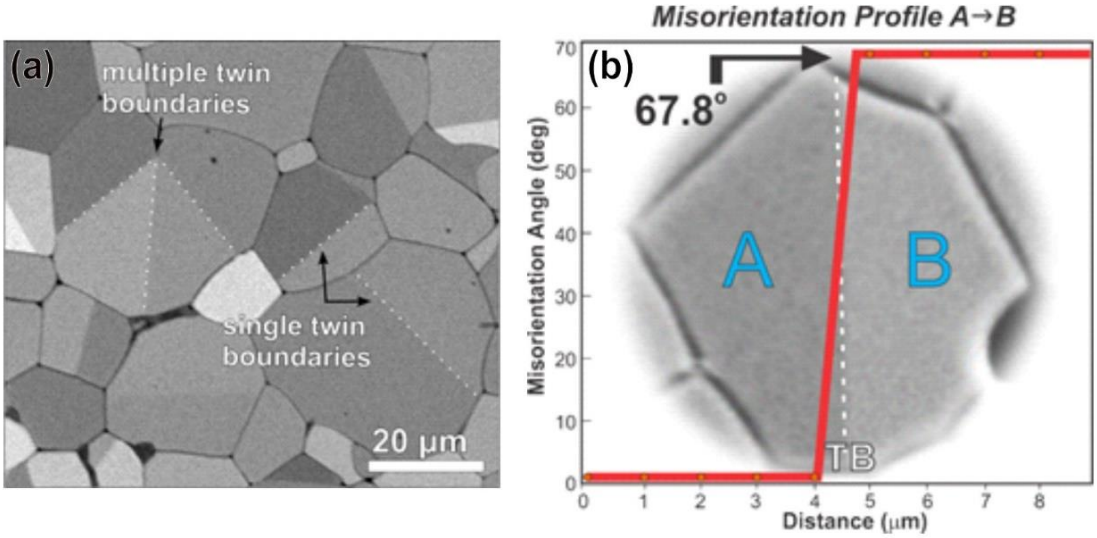

Figure 3.2: FEG-SEM image of thermally etched cross-sections of SnO_2-1 mol% CoO-1 mol% Nb_2O_5 ceramics, sintered at 1430 °C for 5 h. (a) In this sample, multiple (cyclic) and single twin boundaries are present. (b) Misorientation angle between twin individuals A and B: measured misorientation angle across twin boundary of **67.8° ± 0.2°** is the complementary angle of (101) twin boundary in cassiterite, which is 112.2°.

More on this topic is provided in the article entitled "Twinning and charge compensation in Nb_2O_5–doped SnO_2–CoO ceramics exhibiting promising varistor characteristics", written by S. Tominc, A. Rečnik, Z. Samardžija, G. Dražić, M. Podlogar, S. Bernik and N. Daneu [75]. For this article, I performed sample preparation, solid-state sintering, XRD sample preparation, heating microscope sample preparation, density measurements, polishing and thermal etching of the samples, EBSD sample preparation, SEM/TEM sample preparation, SEM/TEM observations, average grain size determination, varistor (I-U) measurements and processing and interpretation of the obtained data together with the listed co-authors. The article is presented on page 33, and its Supporting Information under Appendix A.

Ceramics International 44 (2018) 1603–1613

Contents lists available at ScienceDirect

Ceramics International

journal homepage: www.elsevier.com/locate/ceramint

Twinning and charge compensation in Nb_2O_5–doped SnO_2–CoO ceramics exhibiting promising varistor characteristics

Sara Tominc[a], Aleksander Rečnik[a], Zoran Samardžija[a], Goran Dražić[b], Matejka Podlogar[a], Slavko Bernik[a], Nina Daneu[a,*]

[a] Jožef Stefan Institute, Department for Nanostructured Materials, Jamova cesta 39, Ljubljana, Slovenia
[b] National Institute of Chemistry, Department of Materials Chemistry, Hajdrihova 19, Ljubljana, Slovenia

ARTICLE INFO

Keywords:
Sintering
Planar defects
Point defects
Grain growth
Electrical properties

ABSTRACT

We investigated the effects of dual doping of SnO_2 varistor ceramics with 1 mol% CoO and different amounts of Nb_2O_5 (0.1–2 mol%) on the formation of twin boundaries, microstructure development and electrical properties. Nb_2O_5 addition shifts densification to higher temperatures (up to 1430 °C), producing microstructures composed of twinned SnO_2 grains. Already 0.1 mol% Nb_2O_5 triggers a three-fold increase in growth rate *via* the diffusion induced grain boundary mobility (DIGM). At 0.5 mol% of Nb_2O_5 chemical equilibrium is achieved and SnO_2 grains undergo normal grain growth. Electron back-scatter diffraction (EBSD) has shown that the prevailing type of twins is {101}. Cyclic twins are common. High-angle annular dark-filed scanning transmission electron microscopy (HAADF-STEM) image analysis revealed non-uniform segregation of Nb along the twin boundaries, indicating that they are not directly triggered by Nb_2O_5, but are a result of yet unexplained sequence of topotaxial replacement reactions. Energy dispersive spectroscopy (EDS) has shown that by dual doping of SnO_2 with CoO and Nb_2O_5 the amount of Co dissolved in SnO_2 grains is always ~4x lower compared to the amount of incorporated Nb and propose the following mechanism of tin out-diffusion: $6\,Sn(IV)_{Sn(IV)}^{\times} \leftrightharpoons Sn(II)_{Sn(IV)}^{''} + Co(II)_{Sn(IV)}^{''} + 4\,Nb(V)_{Sn(IV)}^{\cdot}$. Optimal electrical properties were achieved at 1 mol% Nb_2O_5 addition displaying high nonlinearity ($\alpha = 50$), moderate break-down voltage (571 ± 12 V/mm) and low leakage current (I_L = 4.2 μA). The addition of 2 mol% of Nb_2O_5 has an inhibiting effect on densification and SnO_2 grain growth, resulting in a collapse of nonlinearity and increase of leakage current.

1. Introduction

Tin dioxide (SnO_2) is a wide bandgap *n*-type semiconductor with advantageous combination of chemical, electric and optical properties [1] that make it suitable for a range of applications, from solid-state gas sensors, transparent conductive coatings, oxidation catalysts and also varistors [2,3]. Varistors are used as adaptable (nonlinear) resistors for the protection of electrical and electronic components from unwanted voltage surges. The current (I) – voltage (U) nonlinearity of a device is defined by the empirical equation $I = k \cdot U^{\alpha}$, where U is the applied voltage, I is electrical current flowing through the varistor, whereas k and α are linearity constant related to the material's microstructure [3] and the coefficient of nonlinearity that characterize the varistor's response, respectively.

Commercial varistors are commonly based on ZnO ceramics with nonlinear exponents α ranging from 30 to 80 [4]. In order to achieve good electrical properties in ZnO-based systems, rather high additions of many different dopants are required; the overall additions are typically up to 5 mol%. An ideal varistor ceramics is composed of a microstructure with highly conductive grains, separated by nonconductive grain boundaries that typically contain a thin amorphous layer of intergranular phase acting as double Schottky barrier (*i.e.* active grain boundary). In ZnO-based varistors, the ZnO grains are separated by thin Bi-rich layers that form the potential barriers. However, because of the high doping level, ZnO varistor ceramics commonly contains a high fraction of unwanted secondary phases. The presence of excessive amounts of secondary phases at grain boundaries reduces the fraction of active (*i.e.* nonlinear) grain boundaries to only 15–33% [5], which can enhance gradual deterioration of varistor properties during varistor operation [6].

In this view, SnO_2-based varistor ceramics display several advantages over ZnO-based elements [7]. Outstanding I-U nonlinearity of SnO_2-based varistor ceramics was for the first time reported in 1995 by Pianaro et al. [8] and also results, as in the ZnO-based varistor ceramics

* Corresponding author.
E-mail address: nina.daneu@ijs.si (N. Daneu).

http://dx.doi.org/10.1016/j.ceramint.2017.10.081
Received 8 June 2017; Received in revised form 3 October 2017; Accepted 13 October 2017
Available online 14 October 2017

from the Schottky-type barriers at the grain boundaries, which was confirmed by Bueno et al. [9,10]. Microstructure of SnO_2-based varistor elements develops already at much lower dopant additions, usually around 1–2 mol%, and already two or three dopants are sufficient to obtain desired electrical properties. Consequently, the microstructure of such low-doped ceramics is more uniform and contains significantly less secondary phases. This results in considerably higher fraction of active grain boundaries – up to 85% – with uniform current pathways that make device operation more stable [9,10]. In addition, SnO_2-based ceramics show a better temperature resistance and higher thermal conductivity. The main drawbacks of SnO_2-based ceramics are high processing temperature and the relatively high cost of SnO_2 raw material. However, despite these disadvantages, its outperforming electrical characteristics make the use of SnO_2 varistor ceramics preferable in many applications.

Undoped SnO_2 exhibits low densification rates and poor grain growth due to sluggish surface diffusion rates at temperatures below 1300 °C, followed by evaporation-condensation, according to surface dissociation reaction above 1300 °C: $SnO_2 \rightleftarrows SnO + ½O_2$ [13–17]. Improved densification of SnO_2-based ceramics can be achieved by hot isostatic pressing [18] or electric field-assisted flash sintering [19]. Most commonly, however, the sinterability is enhanced by doping [7,20–28]. In general, dopants with valence states lower than 4+, *i.e.* acceptor dopants, substitute Sn^{4+} ions on their regular lattice sites, and trigger the formation of charge compensating oxygen vacancies, $V_O^{\cdot\cdot}$. Since the rate-controlling process in densification of SnO_2 is oxygen diffusion, the increased amount of oxygen vacancies enhances the diffusion processes. The most effective acceptor dopant is CoO, which enhances densification of SnO_2 to 99% of theoretical density [20]. The formation of $V_O^{\cdot\cdot}$ promotes densification *via* the vacancy rate controlled diffusion process [26]. Similar effect can be achieved through the addition of other acceptor dopants such as MnO, CuO and ZnO [7,23–31]. Acceptor doped SnO_2 shows a low nonlinear coefficient and is highly resistive [7]. The electrical conductivity of SnO_2 can be significantly improved by the addition of donor dopants, *i.e.* dopants with valence states higher then 4+, for example Sb_2O_3 (with Sb adopting pentavalent oxidation state at elevated temperatures), Ta_2O_5 and most commonly, Nb_2O_5 [25–33]. Donor doping results in the formation of Sn-site vacancies, $V_{Sn}^{''''}$, that compensate for two $V_O^{\cdot\cdot}$, and increase the conductivity of SnO_2 by creating free electrons in the lattice. Bueno et al. [11,34,35] showed that the Nb_2O_5-doping increases the concentration of shallow donors, which are increasing the electron donation to grain boundary acceptors leading to the enhanced formation of potential barriers and increased amount of active grain boundaries for enhanced I-U nonlinearity. They also found that Nb_2O_5-doping hinders sintering, while Chang et al. [28] reported that it also has an inhibiting effect on grain growth and therefore a balanced addition of acceptor and donor dopants is required.

In varistor ceramics, grain growth studies are of particular interest, because understanding the growth process can be beneficially used for controlling the microstructure development and also for tailoring grain size-dependant electrical properties, such as the threshold voltage [4]. Unlike in ZnO varistor ceramics, where the role of dopants on microstructure evolution is well understood [36], these effects have not been fully examined in SnO_2 ceramics yet. A very interesting study was reported by Kawamura et al. [37] who systematically investigated the influence of transition metal oxides on the morphology of flux grown SnO_2 crystals. They demonstrated that already small amounts of pentavalent dopants, including Nb_2O_5 and Ta_2O_5, trigger heavy twinning in SnO_2. This finding suggests that twinning in SnO_2 could be chemically induced. Similar to ZnO ceramics, where the grain growth is entirely controlled by the formation of inversion boundaries [38–41], such chemically induced twinning may have an important effect on microstructure development in SnO_2 varistor ceramics.

In the present study we explore the role of Nb_2O_5 addition on twin boundary formation, microstructure development, and its effects on electrical properties in SnO_2/CoO–based varistor ceramics.

2. Experimental procedure

2.1. Sample processing

To study the effect of twin boundaries (TB) on microstructure development in SnO_2-based ceramics, we prepared compositions with fixed addition of CoO as a densifying agent, and different amounts of Nb_2O_5: (99-x)% SnO_2 + 1% CoO + x% Nb_2O_5, where x = 0.1, 0.5, 0.75, 1.0 and 2.0 (all compositions in mol%). As starting materials we used analytical-grade powder of SnO_2 (Alfa Aesar, 99.9%, nanopowder), CoO (Alfa Aesar, 95%) and Nb_2O_5 (Merck, 99%) in orthorhombic modification (JCPDS #27-1313). The powder mixtures were homogenized in absolute ethanol, dried at room temperature, and then pressed into pellets, with a diameter of 8 mm and thickness of 3 mm, at a pressure of 150 MPa. The pellets were isothermally sintered at 1430 °C for 5 h with heating and cooling rates of 5 °C/min.

2.2. Characterization methods

Densification characteristics of the samples were recorded on a heating-stage microscope (Ernst Leitz GmbH, Wetzlar, Germany). The densification curves were recorded up to 1480 °C with a heating rate of 10 °C/min. Phase composition of the samples was determined by X-ray diffractometer (PANalytical X'Pert PRO MPD, Almelo, the Netherlands) using Cu-Kα_1 radiation (λ = 1.5406 Å) and a fully opened 100-channel X'Celerator detector under continuous scanning mode in the 2θ range of 20–80° with a step of 0.034° and a recording time of 1 s/step. Phase composition of the samples was analyzed using the X'Pert HighScore software (PW3209, PANalytical, Almelo, the Netherlands).

The relative density of the sintered samples was determined using the Archimedes method and related to the theoretical density of the SnO_2 (ρ_{theor} = 6.95 g/cm^3). Measured densities of the samples after sintering were higher than 90% of ρ_{theor}, except for the undoped SnO_2.

For microstructural observations, the samples were cut in half and fixed in acrylic resin. The cross-sections were mechanically ground and polished down to 0.25 µm, using a diamond paste. To expose the microstructures, polished cross-sections were thermally etched at 1250 °C for 15 min. Microstructural studies were performed using a field-emission gun scanning electron microscope (FEG-SEM; JSM-7600F, Jeol Ltd., Tokyo, Japan) operated at 10-kV and equipped with an energy dispersive X-ray spectrometer (EDS; INCA Oxford 350 EDS SDD, Oxfordshire, UK). The average grain size in the samples with different compositions was determined by a dedicated microstructure analysis program (Image Tool™, University of Texas, USA), where the virtual diameter of irregularly shaped grains is obtained by transforming its area into a circle with an equivalent circumference.

Crystallographic orientations of SnO_2 (cassiterite) grains in polycrystalline bulk matrix were studied using electron back-scatter diffraction (EBSD) technique (Oxford Instruments EBSD system equipped with a Nordlys detector and a *HKL* Channel-5 software) in the FEG-SEM (JEOL JSM-7600F) operated at an accelerating voltage of 20-kV, and using 5-nA beam current. For EBSD studies, the samples were thermally etched for about 5 min to obtain highly crystalline surface without amorphous layer. The EBSD analyses were performed at a working distance of 18 mm and specimen tilt of 70°. The material was sufficiently conductive and thus no charging was observed under operating conditions. The EBSD patterns were acquired at 50 ms dwell time per point and indexed using the unit cell parameters of tetragonal cassiterite (JCPDS #01-077-0449).

The samples for transmission electron microscopy (TEM) investigations were cut from sintered pellets into 3 mm discs by an ultrasonic cutter (SONICUT380, SBT, California, USA). The discs were ground to 100 µm thickness, polished and dimpled down to a 15 µm thickness in the disc center, and finally ion-milled with Ar^+ ions (Gatan Pips Model 691, California, USA) until perforation. To prevent electron charging during observations, the samples were sputtered by a thin

layer of conducting carbon. TEM and EDS analyses were performed using a conventional 200-kV transmission electron microscope (TEM; JEM-2100, Jeol Ltd., Tokyo, Japan) and a 200-kV probe-aberration corrected atomic-resolution scanning transmission electron microscope (STEM; JEM-ARM200 CF, Jeol Ltd., Tokyo, Japan) that was used for studying the atomic-scale distribution of Nb near the twin boundaries. Atomically-resolved images were collected using a high-angle annular dark-field (HAADF) detector with inner and outer semi-angles of 68 and 180 mrad, respectively.

For DC current-voltage (*I-U*) characterization silver paste electrodes were painted on both sides of the sintered pellets and fired at 600 °C for 15 min. Varistor properties of the samples were measured using high-voltage source meter (Keithley 2410, Keithley Instruments Inc., Cleveland, USA). To determine the threshold voltage U_T (V/mm) and the non-linear coefficient (α) we measured nominal varistors voltages U_N (V) at current densities $J_1 = 1$ mA/cm^2 and $J_2 = 10$ mA/cm^2, leakage currents I_L (μA) at 0.75 U_N (1 mA/cm^2) and sample thickness d (mm). The threshold voltage was calculated as $U_T = U_N$ (1 mA/cm^2)/d, and coefficient $\alpha = d \log J/d \log U$.

3. Results

To study the effect of Nb_2O_5 addition on microstructure development and electrical properties of SnO_2–CoO ceramics typical compositions, reported in literature were used. For all samples densification behavior, phase composition, relative density, average grain size and *U-I* properties were measured and discussed in terms of grain growth and twin formation.

3.1. Densification behavior

To determine the optimum sintering temperature for our samples densification behavior for two compositions, SnO_2 + 1 mol% CoO and SnO_2 + 1 mol% CoO + 1 mol% Nb_2O_5, was measured by heating-stage microscope. Relative linear shrinkage $(L_0 - L_1)/L_0$ of the two samples plotted as a function of T is shown in Fig. 1. Undoped SnO_2–CoO sample starts to densify at ~1200 °C and reaches the peak of densification rate at 1315 °C, whereas the onset of densification of the sample doped with 1 mol% of Nb_2O_5 appears at ~100 °C higher temperature, achieving the maximum rate at 1430 °C. We use this temperature as a guideline for our grain growth studies in the SnO_2–CoO –Nb_2O_5 system, where sintering temperature was set to 1430 °C for all samples.

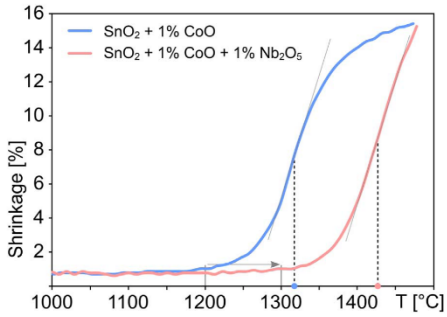

Fig. 1. Relative linear shrinkage $(L_0 - L_1)/L_0$ of the SnO_2 + 1 mol% CoO (*blue curve*) and SnO_2 + 1 mol% CoO + 1 mol% Nb_2O_5 (*red curve*) samples as a function of temperature (T). The shift of densification onset is indicated by an arrow. Dashed vertical lines denote the temperature of maximum densification rate for the two samples. (For interpretation of the references to color in this figure legend, the reader is referred to the web version of this article.)

3.2. Phase composition

Phase composition of the samples was analyzed by powder XRD (Fig. 2). The major phase in all samples corresponds to cassiterite SnO_2 with the rutile-type structure and cell-parameters: a = 0.4735 nm and c = 0.3185 nm (JCPDS #01-077-0449). Compared to the nominal SnO_2 composition (Fig. 2a) no notable changes of the cell parameters are observed with the addition of CoO and Nb_2O_5 (Fig. 2b-g). In the sample with 1 mol% of CoO (Fig. 2b) and in the samples with low Nb_2O_5 addition (< 0.5 mol%; Fig. 2c-d), weak reflections of residual Co_2SnO_4 spinel-type* secondary phase (JCPDS #029–0514) are present (*see* enlarged section of the 2θ range of 34–35°; inset Fig. 2) and confirmed by SEM/EDS analysis (Fig. 2h). Co_2SnO_4 grains are observed either at SnO_2 grain boundaries, or occluded within the SnO_2 grains. They disappear with higher additions of Nb_2O_5 (> 0.5 mol%; Fig. 2e-f). As no other phases were detected in the XRD patterns, even on the highest Nb_2O_5 doping, grain boundaries (GB) and triple points (tp) of the samples at the two ends of our composition range were additionally inspected by TEM (Fig. 3). In undoped SnO_2–CoO sample GBs contain a uniform, amorphous, ~1 nm thick Co-rich equilibrium film (inset; Fig. 3a), whereas any surplus of this phase would be concentrated at triple points (Fig. 3a). EDS analysis did not confirm any Co in bulk SnO_2 grains (Fig. 3b). Unlike the undoped sample, the SnO_2–CoO sample doped with 2.0 mol% of Nb_2O_5 (Fig. 3c) shows small amounts of Co present in bulk SnO_2 grains along with Nb (Fig. 3d). Many GBs in this sample display a diffusion-like (dGB) rippled interfaces (*see* the inset in Fig. 3c). The concentration of Co and Nb varies within the SnO_2 grains and also among the grains in the range of 0.3–1.4 at% for Co and 1.4–6.1 at% for Nb; however, according to EDS measurements the atomic fraction of Co dissolved in SnO_2 always stays 3–5 times lower than that of Nb. Interestingly, a similar Nb/Co ratio as found in SnO_2 grains is maintained in the amorphous GB films, that are present at grain boundaries and triple junctions (tp1, tp2) between Nb-rich pockets and SnO_2 grains. GB films are continuous and have a uniform width of ~1 nm throughout the sample. Any surplus of Nb is segregated at triple junctions. Composition of these pockets is highly variable and could match either Nb_2O_5 or any of the Sn-Nb binary phases; however none of these phases were detected by XRD.

3.3. Microstructure evolution

Let us now take a look on the microstructural features of the samples, shown in Fig. 4. Depending on the amount of Nb_2O_5 added to the SnO_2–1 mol% CoO starting composition we observe a remarkable effect not only on SnO_2 grain size, but also on the degree of porosity and twinning (*see* Table 1 for relative densities and average grain size distributions of the samples). The undoped SnO_2–CoO sample (Fig. 4a) is characterized by small SnO_2 grains (3.4 μm) and a relatively high intergrannular porosity (~10%) with pores located mostly at triple points, and sometimes also at regular GBs. In highly anisotropic materials, such as cassiterite, back-scattered electrons (BSE) are strongly dependant on crystallographic orientation; the grains that are oriented close to a low-index zone-axis would appear dark in contrast, as many electrons are lost due to channeling, whereas misalignments from such orientations for different angles produce different shades of grey. This effect can be exploited to identify twinning in SnO_2 grains. Using BSE mode, TBs can be readily observed as straight lines intersecting the grains, characterized by an abrupt contrast change due to the twin relationship between the adjacent crystal domains. In thermally etched cross-sections of microstructures TBs can be identified by a shallow etch-relief due to their lower interface energy, compared to regular GBs with higher interface energy producing deeper grooves. If we carefully look at the microstructure of undoped SnO_2–CoO sample, shown in Fig. 4a, we see that some SnO_2 grains already contain twin boundaries (*see* Table 1).

Already a small addition of Nb_2O_5 (0.1 mol%) to the starting

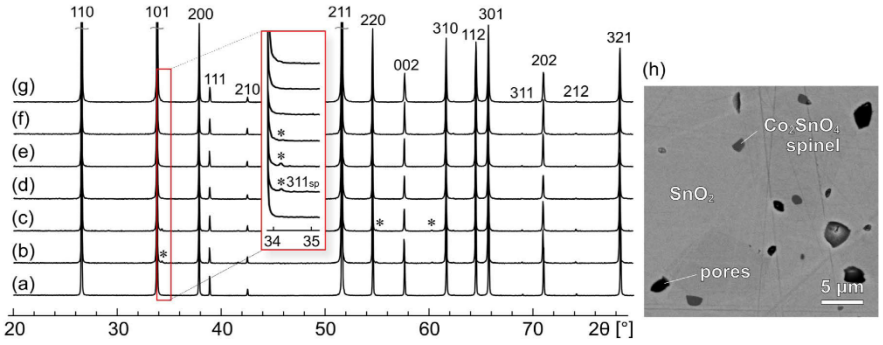

Fig. 2. XRD analysis of the samples with different (99-x)% SnO2 + 1% CoO + x% Nb_2O_5 compositions sintered at 1430 °C for 5 h. (**a**) pure SnO_2; (**b**) SnO_2 + 1 mol% CoO, and (**c-g**) SnO_2 + 1 mol% CoO + 0.1, 0.5, 0.75, 1.0 and 2.0 mol% of Nb_2O_5 addition. Magnified inset at $2\theta \doteq 34.2°$ (outlined in red) shows weak reflections corresponding to Co_2SnO_4 phase (marked by an asterisk). (**h**) Back-scattered SEM image of polished SnO_2 – 1 mol% CoO sample; XRD in (b), showing the presence of micron-sized dark-grey Co_2SnO_4 grains embedded in light-grey SnO_2-matrix; the pores appear black. (For interpretation of the references to color in this figure legend, the reader is referred to the web version of this article.)

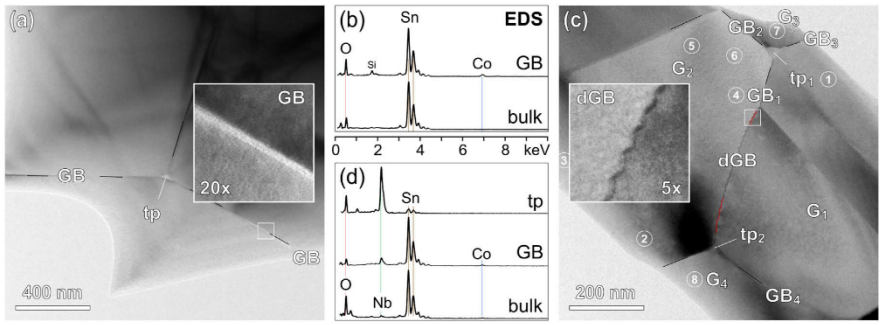

Location	G1-1	GB1	dGB	G2-2	G2-3	G2-4	G2-5	G2-6	GB2	G3-7	GB3	G4-8	GB4	tp1	tp2
Co-K [at%]	1.37	3.64	3.63	0.35	0.28	1.05	1.07	1.15	3.28	0.89	4.48	1.07	4.12	0.93	2.46
Nb-K [at%]	6.10	17.2	12.5	1.44	1.47	3.27	4.39	3.48	17.4	2.76	16.6	3.49	19.4	79.9	49.9
Nb/Co	4.45	4.72	3.43	4.11	5.25	3.11	4.10	3.03	5.30	3.10	3.70	3.26	4.70	85.9	20.3

Fig. 3. TEM/EDS analysis of grain boundaries and triple points in SnO_2–CoO–Nb_2O_5 ceramics. (**a**) TEM image of the SnO_2 – 1 mol% CoO sample showing three GBs (one magnified in the inset) converging to a triple point (white pocket; *tp*), with corresponding (**b**) EDS analysis of bulk SnO_2 and a GB. (**c**) TEM image of the SnO_2 – 1 mol% CoO sample with 2 mol% of Nb_2O_5 addition. Some GBs are undulated, marked with red ripples (dGB), magnified 5× in the inset. (**d**) EDS spectra of bulk SnO_2 grains, GBs and triple points (*tp*) with the corresponding EDS analyses listed below from locations marked in (c).

composition (Fig. 4b) results in a three-fold increase of the SnO_2 average grain size (10.8 µm). With grain sizes, the size of the pores is also increased; however the overall porosity is reduced by almost a half of the starting value (~6%). Many pores are occluded by large grains. Similar to undoped sample, the majority of grains here are single, untwinned crystallites. The fraction of twinned grains is ~ 8%. Further increase of Nb_2O_5 addition (0.5 mol%) rapidly decreases the porosity (~2%) with no much change in the average grain size (Fig. 4c), while a slight increase in the number of twinned grains to ~ 10% is observed. A sharp turnover point in terms of average grain size and fraction of twinned grains is reached by further additions of Nb_2O_5 (Figs. 4d-e) to 0.75 mol%. The porosity is even lower, while the number of twins is increased to 30%. In the sample with an equimolar addition of CoO and Nb_2O_5 (Fig. 4e), every other SnO_2 grain contains a TB and the sample almost reached the theoretical density (Table 1). The microstructure of this sample is tightly packed with SnO_2 grains, where multiple and cyclic twins are common. Higher additions of Nb_2O_5 (2 mol%) have an inhibiting effect on densification and SnO_2 grain growth. Twins are present in almost every grain (Fig. 4f).

3.4. Twin boundary formation

Twin boundaries in Nb-doped SnO_2–CoO ceramics (Nb > 1 mol%) were further studied by electron microscopy methods. Fig. 5 shows single and multiply twinned SnO_2 grains as constituents of the ceramic microstructure. Frequently observed are multiply twinned clusters forming petal-like cyclic crystal assemblies, comprising up to 5 consecutively twinned SnO_2 domains radiating from a common junction (Fig. 5a). Parallel twins are less frequent. The crystallographic nature of the twins was analyzed by TEM. Fig. 5b shows a twin boundary extending across the SnO_2 grain, splitting it into two domains. Selected area electron diffraction (SAED) shows characteristic diffraction spot doublets, produced by 180° rotation around the (101)-plane normal (inset in Fig. 5b), demonstrating that SnO_2 domains are related by (101)-twin operation. No other type of twinning known for cassiterite, such as {301}, could be confirmed in our samples by TEM.

To identify mutual crystallographic relations between twinned SnO_2 domains in ceramic microstructure, we implemented EBSD method. EBSD orientation map, shown in Fig. 6a, was acquired in a rectangular

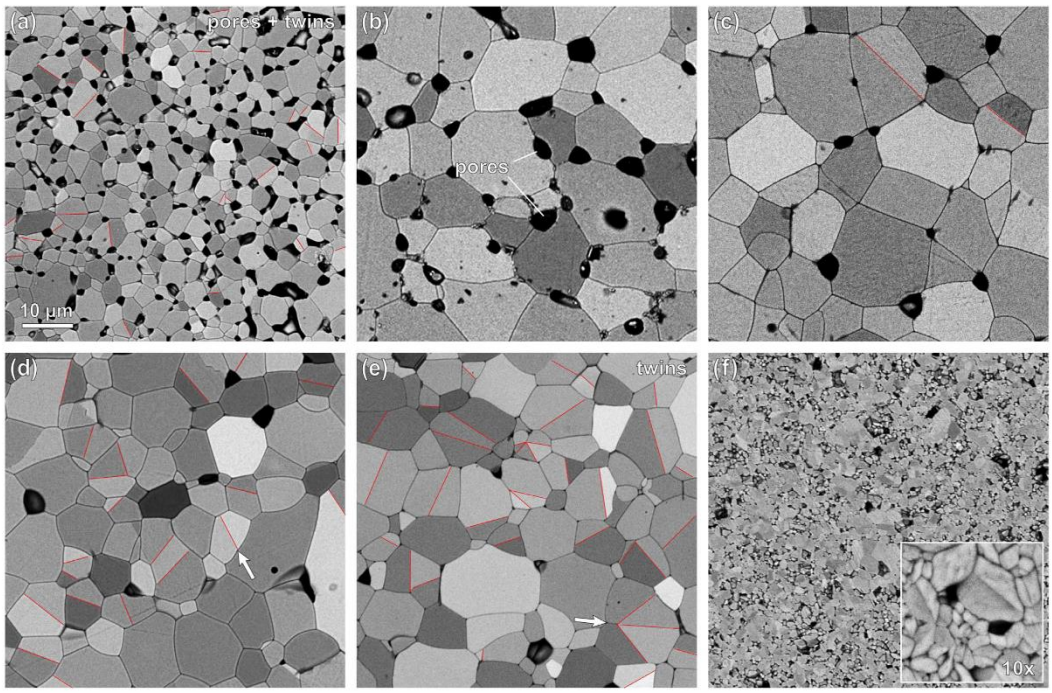

Fig. 4. SEM/BSE images of thermally etched cross-sections of SnO_2–CoO ceramics with different Nb_2O_5 additions. (**a**) SnO_2 – 1 mol% CoO, with no Nb_2O_5, (**b**) 0.1 mol% Nb_2O_5 addition, (**c**) 0.5 mol% Nb_2O_5 addition, (**d**) 0.75 mol% Nb_2O_5 addition, (**e**) 1.0 mol% Nb_2O_5 addition, and (**f**) 2.0 mol% Nb_2O_5 addition with a 10x magnified inset (bottom-right) to show twinned grains. Note the presence of twin boundaries (TBs; marked by thin red lines) in the samples (d) and (e) and the absence of porosity in these two samples. (For interpretation of the references to color in this figure legend, the reader is referred to the web version of this article.)

42 μm × 35 μm area and a step of ~0.6745˙ μm between each measured Kikuchi pattern, which gave the total number of 3231 analyzed points. A high indexing efficiency of 93% was achieved. Non-indexed points occurred mainly because of grain boundary effects, where the local topography, *i.e.* the curvature of GBs grooves and pores, make the pattern acquisition and indexing impossible. All the patterns were indexed with high confidence using 10 characteristic Kikuchi bands with an average mean angular deviation of 0.4°. The acquired data were subsequently processed to obtain information about the crystallographic orientation of SnO_2 grains from the EBSD map.

The spatial distribution of crystallographic orientations of SnO_2 grains in the ceramic microstructure is generally random, as evident from the pole figure plots (not shown), with a sole exception implying a relatively high frequency (~25% of all grains visible at the cross-section surface) of < 001 > pole angular coincidences at 67.8 ± 0.4°. In the implemented software the lower incidence angles are shown, and therefore the measured angle is the complementary angle of (101) twin boundary in cassiterite, corresponding to 112.2°. Frequency of angular incidences among SnO_2 grains within the EBSD map in Fig. 6a is shown in plot of misorientations in Fig. 6b, where neighboring grains were correlated with each other to reveal whether any angular incidences peak above the statistical mean as predicted by the MacKenzie random distribution [42]. Correlation of 147 GBs shows a characteristic distribution of the c-axis misorientations with an absence of low-angle tilt boundaries, where 98% of interfaces are > 27°. The peak observed in the range of 67.5–68.0° corresponding to {101} twin orientations at 67.8°. In addition there exists a ± 2° gap of incidences around the coincident angle for {101} twin boundaries. Relations that would

Table 1
Relative density ρ_{rel}, average grain size d, frequency of twinning f_{TB} and basic varistor properties: threshold voltage U_T, non-linearity coefficient α, leakage current I_L, number of GBs/mm N, and voltage drop per grain boundary U_{GB} of the samples with different nominal compositions.

Sample	ρ_{rel}[a] [%]	d [μm]	f_{TB} [%]	U_T [V/mm]	α	I_L [μA]	N []	U_{GB} [V]
SnO_2	55.7 ± 2.1	~ 0.1 – 1.0	n/a	n/a	n/a	n/a	n/a	n/a
SnO_2 + 1 mol% CoO	90.3 ± 1.3	3.4 ± 1.5	8.4	69 ± 1	6	66.5	293	0.24
… + 0.1 mol% Nb_2O_5	91.4 ± 3.6	10.8 ± 4.1	7.4	87 ± 2	7	56.4	92	0.95
… + 0.5 mol% Nb_2O_5	95.4 ± 4.3	10.5 ± 4.9	10.8	210 ± 2	42	2.1	94	2.23
… + 0.75 mol% Nb_2O_5	97.3 ± 2.4	8.4 ± 4.1	29.4	300 ± 5	46	2.2	118	2.54
… + 1.0 mol% Nb_2O_5	98.6 ± 1.3	7.1 ± 3.7	35.9	571 ± 12	50	4.2	140	4.08
… + 2.0 mol% Nb_2O_5	87.4 ± 5.8	~ 0.1 – 1.0	n/a	119 ± 3	2	79.3	2000	0.06

[a] Theoretical density: ρ_{rtheor} = 6.95 g/cm^3.

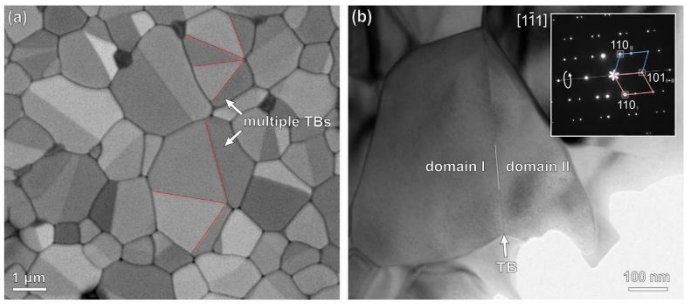

Fig. 5. Twinning in SnO_2 ceramics. (**a**) SEM/BSE image of thermally etched cross-section of the sample with 1 mol% Nb_2O_5, sintered 5 h at 1430 °C. Different shades of BSE contrast are due to different orientations of SnO_2 grains that makes the identification of twinned grains straightforward. In this sample, cyclic twins are common (highlighted by red lines). (**b**) Low-magnification TEM image of (101) twin boundary viewed in [1$\bar{1}$1] orientation with the corresponding electron diffraction pattern showing reflections from both SnO_2 domains (blue and red) in twinned orientation. (For interpretation of the references to color in this figure legend, the reader is referred to the web version of this article.)

correspond to {301} twins, *i.e.* 52.7° (direct angle between the c-axes), fall within the statistical average, confirming that the only type of twinning in our samples is {101}.

In the last step of our {101} twin analysis we address the twin formation mechanism. From experimental observations it is evident that the number of twinned SnO_2 grains increases with the addition of Nb_2O_5. So the most obvious question is where the Nb atoms are located in the SnO_2 structure and in what way they trigger twinning. The best choice to study such problems is atomically-resolved STEM. HAADF-STEM images of (101) twin boundary in SnO_2 are shown in Fig. 7. Local variations in the Z-contrast intensity are due to local chemical inhomogeneities, rather than thickness variation. This has been confirmed by the local EDS/EELS measurements that clearly showed increased amounts of Nb at any dark patches of the low-resolution HAADF-STEM image (Fig. 7a). Such localized increases in Nb concentration are observed in bulk SnO_2 as well as along the twin boundary. Intensity variations are also evident in atomically-resolved HAADF-STEM images. If we take a close look at (101) twin boundary we observe intensity variations of individual atomic columns where the lower intensity columns tend to accumulate along the (101) twin boundary (Fig. 7b). Regular distribution of atomic columns in the HAADF-STEM image suggests that Nb and Co are located on regular lattice sites of the SnO_2 structure. Normalized column intensities were measured using the approach where average intensity of the detector background signal was subtracted from experimental HAADF-STEM images [43]. Pixel intensities of each atomic column were then integrated within an approximated 2D Gaussian profile [44]. Finally, the intensity of each atomic-column was normalized to most intense atomic column, with presumably highest amount of Sn (highest Z-value). Following this method, a 20% decrease of intensity was measured on least intense atomic columns. Given that the brightest intensity represents atomic columns with the highest concentration of Sn, and the columns with least intensity to the highest concentration of Co/Nb in the ratio of 1:4, we can now estimate the fraction of replaced Sn-sites by Nb. Assuming a simple charge compensation model for ionic crystals, solute atoms located at regular lattice sites, and straightforward Z^2-dependency of atomic-column intensity, one can write:

$$I_{HAADF} \propto (1-x)\cdot Z^2_{Sn^{4+}} + x\cdot(\tfrac{1}{6}Z^2_{Co^{2+}} + \tfrac{2}{3}Z^2_{Nb^{5+}} + \tfrac{1}{6}Z^2_{Sn^{2+}}) \quad (1)$$

where x is the fraction of replaced regular Sn^{4+} sites by other species. From the above equation the observed decrease of intensity would be produced by approx. 60% Sn^{4+} ions being replaced by Sn^{2+}, Co^{2+}

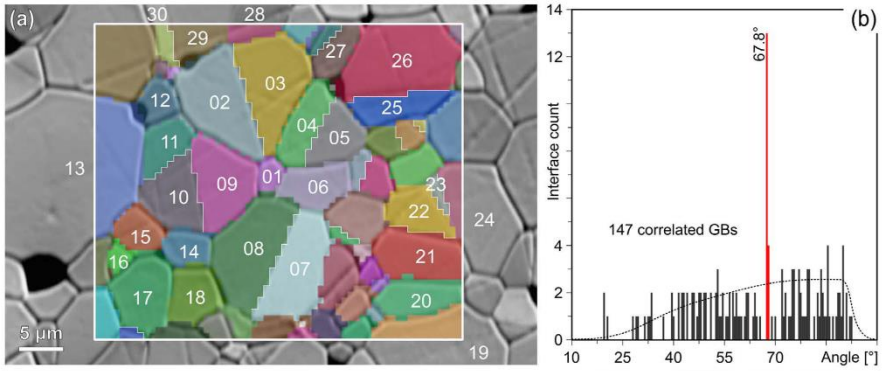

Pair	01-02	02-03	03-04	04-05	07-08	08-09	09-10	10-11	09-11	11-12	20-21	21-22	22-23	23-24	22-24
Angle	80.2	67.8	85.9	67.7	67.7	72.6	67.6	68.3	44.2	33.1	33.9	68.0	67.9	68.3	90.0

Fig. 6. EBSD analysis of grain orientations in Nb_2O_5-doped SnO_2–CoO ceramics. (**a**) EBSD map produced by crystallographic orientation data from 3231 Kikuchi patterns recorded within the outlined area. Selected grains are indicated by numbers and their angular relations are listed below. White lines indicate boundaries where the grains are met in {101} twin orientation. (**b**) MacKenzie plot of relative frequency of angular incidences among the SnO_2 grains included in EBSD analysis. Red lines indicate the incidence corresponding to the complementary angle of {101} twins. Note the ± 2° gap of GB incidences around 67.8°. Dotted line presents the mean angular distribution for randomly oriented grains. (For interpretation of the references to color in this figure legend, the reader is referred to the web version of this article.)

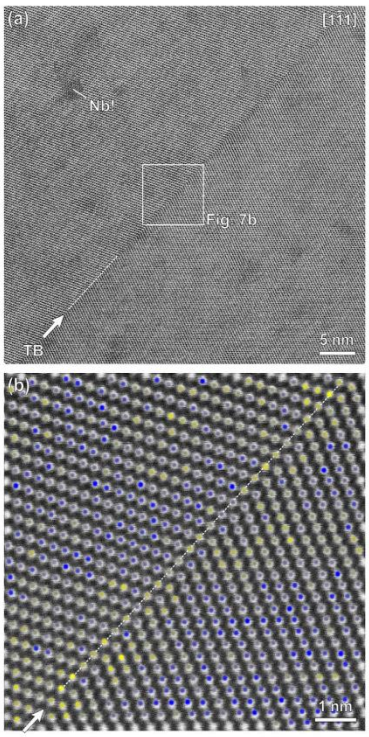

Fig. 7. HAADF-STEM of Nb distribution on TBs and bulk SnO_2, viewed along [1$\bar{1}$1] zone axis. (**a**) Low-resolution Z-contrast image showing patches of darker contrast related to increased Nb-concentration. (**b**) High-resolution Z-contrast image with characteristic intensity variations of atomic columns due to compositional differences. To visualize the distribution the atomic columns are color-coded according to their relative intensity (blue – Sn, yellow – Co/Nb replaced). The arrow indicates the position of the (101) twin boundary. (For interpretation of the references to color in this figure legend, the reader is referred to the web version of this article.)

and Nb^{5+} ions, which corresponds to up to 40 at% of Nb/atomic column. Spatial distribution of solute atoms along the (101) twin boundary is random and only a nonuniform segregation is observed.

3.5. Electrical properties

Relative density, average SnO_2 grain sizes, frequency of twinning and the resulting varistor properties of samples with different additions of Nb_2O_5 are listed in Table 1. While pure SnO_2 does not show a nonlinear behavior, the addition of 1 mol% CoO already results in small nonlinear coefficient and low threshold voltage, showing a weak varistor behavior. SnO_2–CoO ceramics also has a relatively high leakage current, which is also not positive in the varistor applications. Similar electrical properties are measured for the sample with 0.1 mol% Nb_2O_5 addition even though the average SnO_2 grain size is threefold larger. With 0.5 mol% Nb_2O_5 addition the grain size remains unchanged while the threshold voltage and the nonlinearity coefficient increase, achieving a peak at 1 mol% Nb_2O_5 addition. This increase is associated with the increasing fraction of active GBs, *i.e.* high ρ_{rel}, that is reflected in low leakage current of < 5 μA. SnO_2–CoO ceramics doped with 1 mol % of Nb_2O_5 with the highest ρ_{rel} shows the optimum nonlinear electrical behavior at $\alpha \approx 50$. At higher additions of Nb_2O_5 (2 mol%) the porosity again increases and the varistor's properties rapidly deteriorate (*see* Table 1 for details).

Fig. 8 shows the dependence of non-linearity α, leakage current I_L and *I–U* characteristics of our samples depending on the amount of Nb_2O_5. Most significant improvement of nonlinear properties is observed with Nb_2O_5 additions from 0.5 to 1.0 mol%, showing α values from 42 to 50, threshold voltages between 200–600 V/mm and low leakage currents (2.1–4.2 μA). These excellent electrical properties can be attributed to some degree also to the high relative density of these samples. At Nb_2O_5 additions of 2 mol%, the grain growth is suppressed, the density decreases, and the varistor properties are destroyed.

4. Discussion

Our studies of many ceramic materials have shown that planar defects produced with the addition of specific dopants, may have a decisive role in microstructure evolution in such materials. The formation of chemically induced planar faults like inversion, twin or antiphase boundaries, plays an important role in grain growth and microstructure development. Grains in which chemically induced planar faults nucleate in the beginning of the growth process, continue to grow along the chemically induced fault and therefore these grains grow faster compared to the normal grains without these defects [45]. It has been demonstrated that inversion boundaries (IBs) that form in ZnO grains

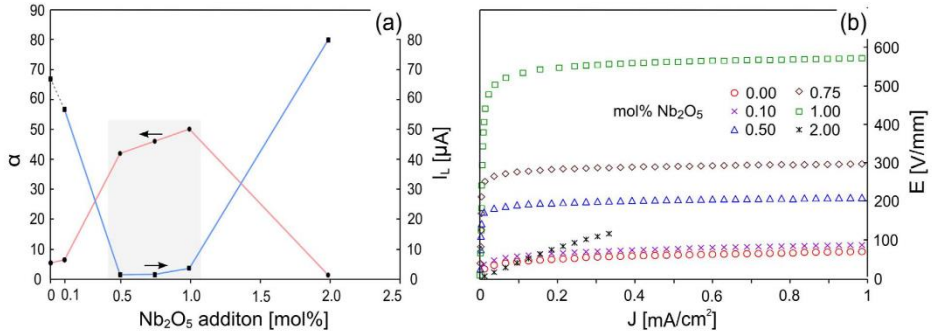

Fig. 8. (**a**) Nonlinear coefficient, α and leakage current, I_L of the SnO_2 – 1 mol% CoO samples doped with different amounts of Nb_2O_5, sintered at 1430 °C for 5 h. Samples with Nb_2O_5 addition between 0.5 and 1.0 mol% show optimum properties (shaded region). (**b**) The nonlinear current-voltage (I–U) characteristics of the SnO_2 – 1 mol% CoO samples doped with different amounts of Nb_2O_5.

after the addition of Sb_2O_3, In_2O_3, TiO_2 and SnO_2 effectively control grain growth in ZnO-based varistor systems [36]. In this work we focused on microstructure development in SnO_2-based varistor ceramics with CoO and Nb_2O_5 addition, where the role of twinning in SnO_2 has not yet been addressed.

4.1. Formation of point defects and charge compensation mechanisms in SnO_2

Microstructural evolution in CoO and Nb_2O_5 doped SnO_2 ceramics is commonly explained as a solid-state sintering process controlled by the formation of point defects [3]. Pure SnO_2 does not densify due to surface reduction of SnO_2 and evaporation of volatile stannic (II) oxide [14] under low oxygen partial pressures > 1300 °C. This process can be described by the formation of oxygen vacancies, $V_O^{\cdot\cdot}$:

$$SnO \xrightarrow{SnO_2} Sn(II)''_{Sn(IV)} + V_O^{\cdot\cdot} + O_O^{\times} \quad (2)$$

Now, unless Sn(II) is stabilized in this structural framework, it departs the system. Out-diffusion of tin releases the holes trapped on the oxygen sublattice [17], making the system structurally unstable. The addition of CoO is known to stabilize cassiterite structure by replacing tin on its regular sites [23]:

$$CoO \xrightarrow{SnO_2} Co(II)''_{Sn(IV)} + V_O^{\cdot\cdot} + O_O^{\times} \quad (3)$$

To some extent this hinders evaporation of SnO and promotes densification through solid-state diffusion. Following this substitution mechanism Co^{2+} readily diffuses into the SnO_2 structure until it reaches the solid solubility limit of around 0.5 mol% [20], whereas any surplus of CoO results in the formation of Co_2SnO_4 spinel phase [22]. In our study, spinels were confirmed by XRD measurements and SEM observations of SnO_2–CoO samples, whereas no Co could be detected in SnO_2 grains by TEM. While the densification is improved, we continue to observe high porosity as a result of moderate SnO evaporation. Previous authors [21–23] suggested that Co_2SnO_4 spinel phase is formed by exsolution of CoO on cooling, however this fails to explain the presence of Co_2SnO_4 particles in SnO_2 grains. On the other hand, the absence of Co in SnO_2 grains, and the presence of CoO-rich equilibrium intergrannular film is indicative of temperature dependant solid solubility of CoO and segregation of solute to GBs and triple points on cooling. Co_2SnO_4 spinels and the CoO-rich intergrannular film appear to be formed in two processes; the first as a result of solid-state reaction between excess CoO with SnO_2 during grain growth, whereas Co exsolved from SnO_2 on cooling, forms the amorphous GB film.

Further evidence that the observed intergrannular film is a result of exsolution is provided by doping the samples with Nb_2O_5. Already with small additions of Nb_2O_5 porosity is reduced, indicating that SnO evaporation at elevated temperatures is suppressed [15]. In the SnO_2-MnO system Bueno et al. [34] observed that Nb_2O_5 doping prevents the formation of the Mn_2SnO_4 spinel phase. Similarly, our EDS analyses have shown that the amount of Co in SnO_2 grains is increased along with Nb, whereas the Co_2SnO_4 spinel reflections disappear from XRD. This suggests a competing compensation mechanism, as proposed by Bueno et al. [25]:

$$2\,Nb_2O_5 \xrightarrow{SnO_2} 4\,Nb(V)^{\cdot}_{Sn(IV)} + V_{Sn}^{''''} + 10\,O_O^{\times} \quad (4)$$

which in combination with Eqs. 2 and 3 corresponds to the observed Co/Nb ratio in SnO_2 grains, empirically described in Eq. (1). Solid-state interdiffusion of Nb^{5+} into the SnO_2 structure is driven by a charge compensation mechanism [28], triggered by the presence of $V_O^{\cdot\cdot}$ that are generated near the surface of SnO_2 grains. Assuming a simple ionic compensation model [17] where dopants occupy regular sites in the cassiterite structure, the 2x negatively charged acceptor doped Sn-sites, replaced by Sn^{2+} and Co^{2+}, are compensated by four 1x positively charged donor doped Sn-sites, occupied by Nb^{5+}:

$$6\,Sn(IV)^{\times}_{Sn(IV)} \leftrightharpoons Sn(II)''_{Sn(IV)} + Co(II)''_{Sn(IV)} + 4\,Nb(V)^{\cdot}_{Sn(IV)} \quad (5)$$

whereby two oxygen vacancies, $V_O^{\cdot\cdot}$, generated by acceptor dopants Sn^{2+} and Co^{2+} are compensated by one vacancy on the tin lattice site, $V_{Sn}^{''''}$, produced by donor doping with Nb^{5+} [29]:

$$\emptyset \leftrightharpoons V_{Sn}^{''''} + 2\,V_O^{\cdot\cdot} \quad (6)$$

creating a double Schottky pair [2,26]. This is in agreement with our TEM/EDS analysis of Nb_2O_5 doped samples where the amount of dissolved Co in the grains is always ~4x lower compared to the amount of dissolved Nb, which corresponds to the ratio of Co^{2+} and Nb^{5+} to produce an equal amount of vacancies on O and Sn sites in SnO_2. Upon doping with Nb_2O_5 no secondary phases were formed on cooling, and more Co remains incorporated in the SnO_2 structure according to this ionic charge compensation mechanism. The proposed formation and equilibria of point defects in this study is in good agreement with point defect compensation in SnO_2 ceramics, previously reported by Leite et al. [46]. While no lattice parameters were changed upon CoO and Nb_2O_5 doping, interstitial compensation as suggested by some authors [22,26–28] may be possible, but only to minor extent. A similar conclusion can be made based on our atomic-scale HAADF-STEM analysis of Co/Nb-doped SnO_2, which confirmed that Co^{2+} and Nb^{5+} mainly occupy regular structure sites in SnO_2.

4.2. SnO_2 grain growth, twinning, and the role of dopants

The addition of Nb_2O_5 has a dramatic effect on SnO_2 grain growth. With the addition of 0.1 mol% of Nb_2O_5 the average grain size is almost tripled compared to the binary SnO_2–CoO system. Several authors that studied microstructure evolution in SnO_2 ceramics report on complete densification already in pure SnO_2–CoO system [20–22], however their experiments were performed at lower temperatures, from 1200 to 1400 °C, where evaporation of SnO_2 is less intense, and observe a reduction of grain sizes after the addition of Nb_2O_5 [28]. In our study we used a higher sintering temperature of 1430 °C, where the evaporation of SnO_2 is intense [13,14] and despite doping with CoO the microstructures are fine grained and porous. With the addition of Nb_2O_5, the densification of SnO_2 ceramics is shifted to even higher temperatures, which is in agreement with the observation of Bueno et al. [34] who reported increased hindering of sintering with the increasing amount of Nb_2O_5.

A sudden increase of average grain size on small Nb_2O_5 additions resembles that observed by Daneu et al. [38] in ZnO-based varistor ceramics doped with SnO_2, where the grain growth is entirely controlled by the formation of IBs in ZnO grains [39–41]. It has been shown that once these chemically-induced defects nucleate in ZnO grains, these new ZnO(IB) grains would entirely consume all normal ZnO grains without these defects. In ZnO ceramics the average grain size is thus inversely proportional to the concentration of the IB-forming dopant, *e.g.* SnO_2, Sb_2O_3, *etc.*: low dopant concentrations produce fewer IBs in ZnO grains and these grow large to recrystallize the whole microstructure, however when a higher concentration of IB-forming dopant is added, IBs form in more ZnO grains, mean free path for growth is shorter, and the average grain size in the ceramic is consequently smaller [36].

The central challenge of this work was to identify whether the twin boundaries (TBs) in SnO_2 have any role in microstructure development of SnO_2-based varistor ceramics. Motivated by the study of Kawamura et al. [36], who reported that the addition of certain metal oxides, including Nb_2O_5, triggers twinning in SnO_2, and reports on unusual effects of Nb_2O_5 addition on microstructure development in SnO_2-based varistor ceramics [28], we choose this system for investigations of the role of twinning in SnO_2 grain growth. At first glance, the effects of Nb_2O_5 addition to the SnO_2–CoO system are similar to what we observe in ZnO–Bi_2O_3 system with the addition of IB-forming dopants: (*i*) TBs are formed in abundance, (*ii*) there is an initial increase of grain sizes on

small dopant concentrations, while on (*iii*) the increasing addition of the dopant, the average grain size is suppressed.

However, when we look carefully on the response of the system to Nb_2O_5 addition we see that not all SnO_2 grains contain a TB, moreover, TBs are already present in the microstructure prior to the addition of Nb_2O_5, which implies that TBs are not exclusively a result of Nb_2O_5 doping. With increasing addition of Nb_2O_5 the number of twins is increased, but never affects all grains, like IBs in ZnO. Even if we take into account that 2D features, such as TBs, are generally underestimated and effectively, there are always ~30% more twinned grains in the microstructure than actually observed in random cross-section [40], the number of twinned grains in SnO_2 ceramics never exceeds 50% of the microstructure. This alone is a strong indication implying that TBs in SnO_2 do not play the same role in microstructure development as IBs in ZnO. Their different nature is further confirmed by our EDS and HAADF-STEM analysis, which did not confirm any abrupt compositional change at the TB plane that would indicate the existence of a 2D phase like layer, that characterizes typical growth defects, such as APBs in $CaTiO_3$ [45], IBs in ZnO [47], or TBs in spinel [48], and dictates anisotropic growth of composite grains along the fault plane as long as the fault-triggering dopant is available in surroundings. In SnO_2 ceramics we do not observe anisotropic growth along the TBs and the dopants are merely segregated to the vicinity of the twin plane rather than being strictly localized to it. All this implies that TBs in SnO_2 are formed in the nucleation stage, and have a benign role in ceramic microstructure evolution.

While TBs in SnO_2 may not be chemically induced, the role of dopants is not as trivial as originally expected. This is due to a different origin of their formation. In the structurally related rutile (TiO_2) it has been shown that twinning is a consequence of complex topotaxial replacement reactions after structurally related bulk precursors [49], and is driven by the changes in oxidation conditions that consequently trigger diffusion controlled remobilization of cations [50]. A similar mechanism could be responsible for twinning of cassiterite. While crystallography of {101} twin boundaries in SnO_2 has been recently explained by Nespolo & Souvignier [51], questions related to their formation remain unsolved. Twinning in cassiterite is reported in both pure and doped SnO_2. In pure SnO_2 twinned crystals were produced by electron or laser ablation of SnO_2 or Sn in O_2 atmosphere [52–56] conducted in partially reducing growth conditions. The highest density of {101} twins was reported by Zheng et al. [54] who studied SnO_{2-x} films. Tseng et al. [55,56] suggested that polysynthetic twinning of SnO_2 may be related to the *o*-$CaCl_2$-type structure caused by slight polyhedral distortion. Based on their study of polycrystalline SnO_2 films Tomaev & Glazov [57] suggested that doping can be used to control the concentration of twins. They showed that trivalent dopants trigger abundant twinning in SnO_2. Similar observation was done by Kawamura et al. [37,58] who observed twinning in flux grown SnO_2 crystals by the addition of Fe_2O_3, Ga_2O_3, Sb_2O_3, Nb_2O_5 and Ta_2O_5, whereas Oliveira et al. [59] reported on formation of twins in La_2O_3 and Pr_2O_3-doped SnO_2 ceramics. Given the diversity of growth conditions there appears to be no consensus about what triggers twinning in SnO_2. Apparently, some nonstoichiometry related lattice strain, or topotaxial replacement on unknown precursor phases may be the reasons. The formation of cyclic twins with increasing additions of Nb_2O_5 favors the topotaxial mechanism, whereas the presence of single TBs even in undoped SnO_2 suggests lattice strain related nucleation, where the presence of aliovalent species, such as Sn^{2+}, Co^{2+}, *etc.* could cause cationic imbalance.

The observed increase of the average grain size on small additions of Nb_2O_5 can thus be attributed to suppression of SnO_2 evaporation due to combined stabilization of point defects, and enhanced diffusion controlled grain boundary mobility due to increased chemical potential of the species in the grain boundary region. According to Hillert [60], the major driving force for such growth is discontinuity in chemical composition, which triggers accelerated diffusion induced grain boundary mobility (DIGM). In our system the compositional gradient is driven by the formation of $V_O^{\cdot\cdot}$ due to $Sn^{4+} \rightarrow Sn^{2+}$ reduction on SnO_2 surface. While without doping, SnO_2 evaporates at elevated temperatures [14], its structure is stabilized by combined Co/Nb doping that creates the chemical discontinuity. As long as such nonequilibrium condition persists, the grains grow exaggeratedly until the necessary concentration of solute atoms is attained for chemical equilibrium. Typical for DIGM are wavy GBs with macroscopic high energy undulations, which are observed in all Nb_2O_5–doped samples. In this process, all low-angle tilt boundaries are consumed, indicating that they are thermodynamically less favorable [35], as confirmed by our EBSD analysis of angular relations in Nb_2O_5–doped SnO_2–CoO ceramics. This grain growth mechanism where grains grow exaggeratedly due to their high internal chemical potential, can also be observed on cyclic twins. Here, due to rapid growth of SnO_2 domains, individual twin domains develop a convex shape, whereas the TBs are simply dragged along, and as a result of this process, they display characteristic re-entrant angles. With increasing addition of Nb_2O_5 more nuclei are formed, the resulting microstructure is fine grained, and all grains contain twin boundaries. Microstructure development in SnO_2 ceramics is thus similar to that described in ZnO-based varistor ceramics, where higher additions of dopants lead to fine grained microstructures following IB-induced grain growth mechanism [38–41]. Approaching a chemical equilibrium at 1 mol% of Nb_2O_5, SnO_2 grain growth slows down, while in the sample with highest Nb_2O_5 addition (2 mol%), inhibited grain growth is observed. According to our TEM/EDS analyses of this sample, the average amount of Co inside SnO_2 grains is ~0.9 at% and that of Nb is ~3.3 at %. This suggests that there is a surplus of Nb_2O_5 in this composition, also indicated by Nb-rich triple grain junctions. At this point, the formation of $V_{Sn}^{''''}$ (Eq. (4)) prevails over the $V_O^{\cdot\cdot}$ (Eq. (3)) formation and the grain growth is inhibited. It has been shown previously that Nb^{5+} has an inhibiting effect on SnO_2 grain growth [28] and leads to a fine-grained microstructure; however, this effect only takes place when the formation of $V_{Sn}^{''''}$ is not compensated by $V_O^{\cdot\cdot}$.

4.3. Electrical properties

While typical correlation between grain size and the break-down voltage is only vaguely expressed, the current-voltage (I–U) characteristics of the samples indicate strong dependence to the established equilibria of defects in the grains and at the grains boundaries induced by the CoO and Nb_2O_5 doping in accordance to the Eqs. (2) to (6) [46], Nagasawa [13] suggested that oxygen vacancies or interstitial Sn ions could act as donor centers responsible for *n*-type conductivity of cassiterite. It is known that addition of CoO improves SnO_2 densification by forming additional oxygen vacancies, while niobium ions, as donors, incorporate into SnO_2 grains and enhance their electrical conductivity [11,12,34,61]. In the undoped SnO_2–CoO ceramics week I–U nonlinearity and very low breakdown voltage despite the small grain size likely result from the difference in resistivity between the grains and the GBs, which is controlled by low conductivity of grains, as already observed by Metz et al. [24]; due to very limited solubility of Co^{2+} in SnO_2 (below the detection limit of EDS analysis) form associates [$Co(II)_{Sn}^{''}{}_{(IV)} + V_O^{\cdot\cdot}$], which act as shallow donors, can only weekly contribute to the conductivity of the grains, while the majority of the added CoO (*p*-type conductor) is segregated at the grain boundaries.

With Nb_2O_5-doping the solubility of Co^{2+} in the SnO_2 increased in proportion to its amount and prevented its segregation at the grain boundaries, while the donor defects $Nb(V)_{Sn(IV)}^{\cdot}$ formed in the SnO_2 grains (Eq. (5)) enhanced their conductivity. In parallel to the Nb-donor defects, Sn-vacancies ($V_{Sn}^{''''}$) are formed, that act as electron traps enhancing the formation of electrostatic double Schottky barriers at grain boundaries. These observations are well in agreement with the previous reports of Bueno and coworkers [11,12,34,35]. At the lowest addition of Nb_2O_5 (0.1 mol%) this effect is only slightly expressed in the nonlinear coefficient (α = 7), which remains similar as in the undoped

sample (α = 6), accompanied with a small decrease of leakage current (*see* Table 1). However, if we consider that an average grain size is 3-times larger than that of the undoped sample, this value reflects in effect, a 4-fold increase of the nominal breakdown voltage per GB (U_{GB})! With further increase of Nb_2O_5 doping (0.5 mol%), the conductivity of the grains progressively enhances, as well as the height of electrostatic barriers at the grain boundaries, and hence their resistivity (*i.e.* breakdown voltage). Accordingly, the coefficient of nonlinearity increases to values above 40, reaching its maximum at 50, for 1 mol% of Nb_2O_5. In the samples with 0.5–1 mol% Nb_2O_5 additions, the density of the samples is close to the theoretical, resulting in a high percentage of active grain boundaries [7] and excellent electrical properties. The threshold voltage U_T rapidly increases regardless the slight decrease in grain size, as the average U_{GB} increases to 4.0 V/GB. Extreme voltage drop per GB, accompanied with a sudden blockage of leakage current I_L, presents unprecedented electrical properties for the ternary SnO_2–CoO–Nb_2O_5 varistor ceramics. Similar was observed by Bueno et al. [34] in Nb_2O_5-doped SnO_2-MnO ceramics with strong increase in U_T and α for Nb_2O_3 for additions above 0.2 mol% while I_L dropped significantly.

The addition of 2 mol% of Nb_2O_5 drastically reduces the grain size (Fig. 3d), increases the porosity and results in a collapse of nonlinearity and an increase of leakage current to a value even higher than that for the undoped SnO_2–CoO sample, indicating that the critical maximum value of Nb_2O_5 doping is exceeded. Pianaro et al. [3] reported a similar increase of nonlinear coefficient (α = 41) when SnO_2-based varistor ceramics with 1 mol% of CoO and 0.05 mol% of Nb_2O_5 was doped with 0.05 mol% Cr_2O_3. Other authors succeeded to increase the nonlinear coefficient with the addition of small amounts of other transition metal oxides [62,63] or rare earth oxides [64,65] to the SnO_2–CoO–Nb_2O_5 ternary system, however until now, such a high coefficient of nonlinearity for this ternary system as obtained in our work has not yet been achieved, implying that equilibria of point defects in the SnO_2 grains play the key role in the varistor's properties, and a balanced addition of donor and acceptor dopants is required to achieve an optimum I–U nonlinearity with low leakage currents.

5. Conclusions

In this work we studied the effects of Nb_2O_5 additions to SnO_2 − 1 mol% CoO varistor ceramics with special emphasis on the formation of twin boundaries in SnO_2 grains. In undoped ceramics, twin boundaries are observed only occasionally, while their fraction with Nb_2O_5 addition increases and cyclic twins become common. This confirms that the formation of twins is related to Nb_2O_5 addition. HRTEM and HAADF-STEM analyses have shown that Nb segregates to the twin boundaries, however its distribution is random, suggesting that they form as a result of a topotaxial recrystallization process in the beginning of SnO_2 grain growth.

One of the most important effects of Nb_2O_5 additions (< 1 mol%) is a drastic decrease in porosity. Detailed TEM/EDS analyses of the distribution of both dopants inside SnO_2 grains, at grain boundaries, and at triple points, suggest a synergistic effect of aliovalent dopants addition on densification and grain growth of SnO_2 *via* the charge compensation mechanism in SnO_2 grains, which is governing the accelerated diffusion induced grain boundary mobility in this ceramic system. The incorporation of donor (Nb^{5+}) and acceptor (Co^{2+}) dopants in regular Sn^{4+} sites in the SnO_2 structure in 4:1 ratio adjusts the charge balance in SnO_2, preventing evaporation of SnO and, at optimum densification temperature of 1430 °C, it results in almost fully dense, pore-free ceramics with excellent electrical properties for surge protection applications, *i.e.* high coefficient of nonlinearity (α = 45–50) and low leakage current (I_L = 2–4 μA).

Acknowledgements

This work was supported by the Slovenian Research Agency under The Project No. J1-6742 and is based in part on the Ph.D. Thesis of S. Tominc under the contract No. 0106/37484.

References

[1] Z.M. Jarzebski, J.P. Marton, Physical properties of SnO_2 materials I. Preparation and defect structure, J. Electrochem. Soc. 123 (1976) 199C–205C.
[2] M. Batzill, U. Diebold, The surface and materials science of tin oxide, Prog. Surf. Sci. 79 (2005) 47–154.
[3] S.A. Pianaro, P.R. Bueno, E. Longo, J.A. Varela, A new SnO_2-based varistor system, J. Mater. Sci. Lett. 14 (1995) 692–694.
[4] D.R. Clarke, Varistor ceramics, J. Am. Ceram. Soc. 82 (1999) 485–502.
[5] M. Tao, B. Ai, O. Dorlanne, A. Loubiere, Different "single grain junctions" within a ZnO varistor, J. Appl. Phys. 61 (1987) 1562–1567.
[6] Y.M. Chiang, W.D. Kingery, L.M. Levnison, Compositional changes adjacent to grain boundaries during electrical degradation of a ZnO varistor, J. Appl. Phys. 53 (1982) 1765–1768.
[7] P.R. Bueno, J.A. Varela, E. Longo, SnO2, ZnO and related polycrystalline compound semiconductors: an overview on the voltage dependent resistance (non-ohmic) feature, J. Eur. Ceram. Soc. 28 (2008) 505–529.
[8] S.A. Pianaro, P.R. Bueno, E. Longo, J.A. Varela, A new SnO_2-based varistor system, J. Mater. Sci. Lett. 14 (1995) 692–694.
[9] P.R. Bueno, M.R. de Cassia-Santos, E. Longo, J. Bisquert, G. Garcia-Belmonte, F. Fabregant-Santiago, Nature of the Schottky-type barrier of highly dense SnO2 systems displaying nonohmic behavior, J. Appl. Phys. 88 (2000) 6545–6548.
[10] P.R. Bueno, E.R. Leite, M.M. Oliveira, M.O. Orlandi, E. Longo, Role of oxygen at the grain boundary of metal oxide varistors: a potential barrier formation mechanism, Appl. Phys. Lett. 79 (2001) 48–50.
[11] P.R. Bueno, M.A. Santos, M.A. Ramirez, R. Tararam, E. Longo, J.A. Varela, Relationship between grain-boundary capacitance and bulk shallow donors in SnO_2 polycrystalline semiconductor, Phys. Stat. Solidi a 205 (2008) 1694–1698.
[12] J.S. Vasconcelos, N.S.L.S. Vasconcelos, M.O. Orlandi, P.R. Bueno, J.A. Varela, E. Longo, C.M. Barrado, E.R. Leite, Electrostatic force microscopy as a tool to estimate the number of active potential barriers in dense non-Ohmic polycrystalline Sn_O2 devices, Appl. Phys. Lett. 89 (2006) (152102_1-152102_3).
[13] M. Nagasawa, S. Shionoya, S. Makishima, Vapor reaction growth of SnO_2 single crystals and their properties, Jpn. J. Appl. Phys. 4/3 (1965) 195–202.
[14] C.I.. Hoenig, A.W. Searcy, Knudsen and Langmuir evaporation studies of stannic oxide, J. Am. Ceram. Soc. 49 (1966) 128–134.
[15] J.A. Varela, O.J. Whittemore, E. Longo, Pore size evolution during sintering of ceramic oxides, Ceram. Int. 16 (1990) 177–189.
[16] E.R. Leite, J.A. Cerri, E. Longo, J.A. Varela, C.A. Paskocima, Sintering of ultrafine undoped SnO_2 powder, J. Eur. Ceram. Soc. 21 (2001) 669–675.
[17] P. Chentri, B. Choudhury, A. Choudhury, Room temperature ferromagnetism in SnO_2 nanoparticles: an experimental and density functional study, J. Mater. Chem. C. 2 (2014) 9294–9302.
[18] J.H. Lee, S.J. Park, K. Hirota, Temperature dependence of electrical conductivity in polycrystalline tin oxide, J. Am. Ceram. Soc. 73 (1990) 2771–2774.
[19] R. Muccillo, E.N.S. Muccillo, Electric field-assisted flash sintering of tin dioxide, J. Eur. Ceram. Soc. 34 (2014) 915–923.
[20] J.A. Cerri, E.R. Leite, D. Gouvêa, E. Longo, Effect of cobalt(II) oxide and manganese (IV) oxide on sintering of tin(IV) oxide, J. Am. Ceram. Soc. 79 (1996) 799–804.
[21] J.A. Varela, J.A. Cerri, E.R. Leite, E. Longo, M. Shamsuzzoha, R.C. Bradt, Microstructural evolution during sintering of CoO doped SnO_2 ceramics, Ceram. Int 25 (1999) 253–256.
[22] B.C. Kim, J.I. Jung, J.H. Lee, J.J. Kim, Precipitate concentration of Co_2SnO_4 in CoO-doped SnO_2 ceramics at different oxygen chemical potentials, Sol. State Ion. 144 (2001) 321–327.
[23] T.S. Zhang, L.B. Kong, X.C. Song, Z.H. Du, W.Q. Xu, S. Li, Densification behavior and sintering mechanisms of Cu- or Co-doped SnO_2: a comparative study, Acta Mater. 62 (2014) 81–88.
[24] R. Metz, D. Koumeir, J. Morel, J. Pansiot, M. Houabes, Hassanzadeh. Electrical barriers formation at the grain boundaries of Co-doped SnO_2 varistor ceramics, J. Eur. Ceram. Soc. 28 (2008) 829–835.
[25] P.R. Bueno, S.A. Pianaro, E.C. Pereira, L.O.S. Bulhões, E. Longo, J.A. Varela, Investigation of the electrical properties of SnO_2 varistor system using impedance spectroscopy, J. Appl. Phys. 84 (1998) 3700–3705.
[26] S.A. Pianaro, P.R. Bueno, P. Olivi, E. Longo, J.A. Varela, Electrical properties of the SnO_2-based varistor, J. Mater. Sci: Mater. Electron. 9 (1998) 159–165.
[27] G. Branković, Z. Branković, M.R. Davolos, M. Cilense, J.A. Varela, Influence of the common varistor dopants (CoO, Cr_2O_3 and Nb_2O_5) on the structural properties of SnO_2 ceramics, Mater. Charact. 52 (2004) 243–251.
[28] D.G. Chang, J.H. Lee, J.J. Kim, Grain growth kinetics of cobalt-doped SnO_2 by varying Nb_2O_5 content, Mater. Sci. Forum 534–536 (2007) 529–532.
[29] J. Fayat, M.S. Castro, Defect profile and microstructural development in SnO_2-based varistors, J. Eur. Ceram. Soc. 23 (2003) 1585–1591.
[30] J.A. Varela, D. Gouvea, E. Longo, N. Dolet, M. Onillon, J.P. Bonnet, The effect of additives on the sintering of tin oxide, Solid State Phenom. 25–26 (1992) 259–268.
[31] M.K. Paria, S. Basu, A. Paul, Enhanced sintering of tin dioxide with additives under isothermal condition, Trans. Indian Ceram. Soc. 42 (1983) 90–95.

[32] D. Gouvea, J.A. Varela, C.V. Santilli, E. Longo, Effect of niobia on the sintering of Sn_O2, Sci. Sintering (1989) 529–536 (New directions for materials processing and microstructural control).
[33] T. Kimura, S. Inada, T. Yamaguchi, Microstructure development in SnO_2 with and without additives, J. Mater. Sci. 24 (1989) 220–226.
[34] P.R. Bueno, M.O. Orlandi, L.G.P. Simoes, E.R. Leite, E. Longo, J.A. Cerri, Nonohmic behavior of SnO_2-MnO polycrystalline ceramics. I. Correlations between microstructural morphology and nonohmic fea-tures, J. Appl. Phys. 96 (2004) 2693–2699.
[35] M.O. Orlandi, M.R.D. Bomio, E. Longo, P.R. Bueno, Nonohmic behavior of SnO_2-MnO polycrystalline ce-ramics. II. Analysis of admittance and dielectric spectroscopy, J. Appl. Phys. 96 (2004) 3811–3817.
[36] A. Rečnik, N. Daneu, S. Bernik, Microstructural engineering of ZnO-based varistors ceramics, J. Mater. Sci. 47 (2012) 1655–1668.
[37] F. Kawamura, M. Kamei, I. Yasui, Effect of impurity cations on the growth and habits of SnO_2 crystals in the SnO_2-Cu_2O flux system, J. Am. Ceram. Soc. 82 (1999) 774–776.
[38] N. Daneu, A. Rečnik, S. Bernik, D. Kolar, Microstructural development in SnO_2-doped ZnO–Bi_2O_3 ceramics, J. Am. Ceram. Soc. 83 (2000) 3165–3171.
[39] N. Daneu, A. Rečnik, S. Bernik, Grain growth control in Sb_2O_5-doped zinc oxide, J. Am. Ceram. Soc. 86 (2003) 1379–1384.
[40] S. Bernik, J. Bernard, N. Daneu, A. Rečnik, Microstructure development in low Sb_2O_3-doped ZnO ceramics, J. Am. Ceram. Soc. 90/10 (2007) 3239–3247.
[41] N. Daneu, A. Rečnik, S. Bernik, Grain growth phenomena in ZnO ceramics in the presence of inversion boundaries, J. Am. Ceram. Soc. 94 (2011) 1619–1626.
[42] J.K. MacKenzie, Statistics associated with the random disorientation of cubes, Biometrika 45/1 (1958) 229–240.
[43] J.M. LeBeau, S. Stemmer, Experimental quantification of annular dark-field images in scanning transmission electron microscopy, Ultramicroscopy 108 (2008) 1653–1658.
[44] T. Rojac, A. Benčan, G. Dražić, N. Sakamoto, H. Uršič, B. Jančar, G. Tavčar, M. Makarovič, J. Walker, B. Malič, D. Damjanović, Domain-wall conduction in ferroelectric $BiFeO_3$ controlled by accumulation of charged defects, Nat. Mater. 16 (2017) 322–327.
[45] A. Rečnik, M. Čeh, D. Kolar, Polytype induced exaggerated grain growth in ceramics, J. Eur. Ceram. Soc. 21 (2001) 2117–2121.
[46] E.R. Leite, A.M. Nascimento, P.R. Bueno, E. Longo, J.A. Varela, The influence of sintering process and atmosphere on the non-ohmic properties of SnO_2 based varistor, J. Mater. Sci. – Mater. Electron. 10 (1999) 321–327.
[47] A. Rečnik, N. Daneu, T. Walther, W. Mader, Structure and chemistry of basal-plane inversion boundaries in Sb_2O_3-doped ZnO, J. Am. Ceram. Soc. 84 (2001) 2657–2668.
[48] S. Drev, A. Rečnik, N. Daneu, Twinning and epitaxial growth of taaffeite-type modulated structures in BeO-doped $MgAl_2O_4$, CrystEngComm 15 (2013) 2657–2668.
[49] N. Daneu, A. Rečnik, W. Mader, Atomic structure and formation mechanism of (101) rutile twins from Diamantina (Brazil), Am. Mineral. 99 (2014) 612–624.
[50] N. Stanković, A. Rečnik, N. Daneu, Topotaxial reactions during oxidation of ilmenite single crystal, J. Mater. Sci. 51 (2016) 958–968.
[51] M. Nespolo, B. Souvignier, Structural rationale for the occurrence of the elbow twins in cassiterite and rutile, J. Mineral. Pet. Sci. 110 (2015) 157–165.
[52] H. Iwanaga, M. Egashira, K. Suzuki, M. Ichihara, S. Takeuchi, Twins in SnO_2 whiskers, J. Mater. Sci. Lett. 8 (1989) 1179–1181.
[53] K. Suzuki, M. Ichihara, S. Takeuchi, High-resolution electron microscopy of lattice defects in TiO_2 and SnO_2, Philos. Mag. A 63 (1991) 657–665.
[54] J.G. Zheng, X. Pan, M. Schweizer, F. Zhou, U. Weimar, W. Göpel, M. Rühle, Growth twins in nanocrystalline SnO_2 thin films by high-resolution transmission electron microscopy, J. Appl. Phys. 79 (1996) 7688–7694.
[55] W.J. Tseng, P. Shen, S.Y. Chen, Defect generation of rutile-type SnO_2 nanocondensates: imperfect oriented attachment and phase transformation, J. Sol. St Chem. 179 (2006) 1237–1246.
[56] W.J. Tseng, P. Shen, S.Y. Chen, Fabrication and transformation of dense SnO_2 via laser ablation condensation, J. Phys. Chem. Sol. 70 (2009) 334–339.
[57] V.V. Tomaev, A.I. Glazov, Morphology of polycrystalline cassiterite films, Nanomater. Ceram. 59 (2014) 819–823.
[58] F. Kawamura, I. Yasui, M. Kamei, I. Sunagawa, Habit modifications of SnO_2 crystals in SnO_2–Cu_2O flux system in the presence of trivalent impurity cations, J. Am. Ceram. Soc. 84/6 (2001) 1341–1346.
[59] M.M. Oliveira, P.C. Soares Jr, P.R. Bueno, E.R. Leite, E. Longo, J.A. Varela, Grain-boundary segregation and precipitates in La_2O_3 and Pr_2O_3 doped SnO_2-CoO-based varistors, J. Eur. Ceram. Soc. 23 (2003) 1875–1880.
[60] M. Hillert, On the driving force for diffusion induced grain boundary migration, Scrip Metall. 17 (1983) 237–240.
[61] C.M. Wang, J.F. Wang, W.B. Su, Microstructural morphology and electrical properties of copper- and niobium-doped tin dioxide polycrystalline varistors, J. Am. Ceram. Soc. 89 (2006) 2502–2508.
[62] A.C. Antunes, S.R.M. Antunes, S.A. Pianaro, Effect of La_2O_3 doping on the microstructure and electrical properties of a SnO_2-based varistors, J. Mat. Sci: Mat. Electron. 12 (2001) 69–74.
[63] S.A. Pianaro, P.R. Bueno, P. Olivi, E. Longo, J.A. Varela, Effect of Bi_2O_3 addition on the microstructure and electrical properties of the SnO_2-CoO-Nb_2O_5 varistor system, J. Mater. Sci. Lett. 16 (1997) 634–638.
[64] H. Bastami, E. Taheri-Nassay, Effect of Sm_2O_3 on the microstructure and electrical properties of SnO_2-based varistors, Ceram. Int 38 (2012) 265–270.
[65] I. Safaee, M.A. Bahrevar, M.M. Shahraki, S. Baghshahi, K. Ahmadi, Microstructural characteristics and grain growth kinetics of Pr_6O_{11} doped SnO_2-doped varistors, Solid State Ion. 189 (2011) 13–18.

Chapter 4

Charge Compensation and Electrical Characteristics of Ta_2O_5-Doped SnO_2-CoO Ceramics

In Chapter 3, I have shown that sinterability of SnO_2-based varistor ceramics is enhanced by a balanced addition of donor (Nb^{5+}) and acceptor (Co^{2+}) dopants (in 4:1 ratio), reaching pore-free ceramics with excellent electric properties for high voltage applications. In this Chapter, I studied a similar pentavalent donor dopant Ta_2O_5 in the SnO_2-CoO ceramic system and its influence on the microstructure development and electrical characteristics. Furthermore, I proposed the most probable charge compensation mechanism for the SnO_2-CoO-Ta_2O_5 ceramic system. I identified several important distinctions from the Nb_2O_5 system:

I. Solid solubility

Considerably lower solid solubility of Ta_2O_5 in SnO_2 and approximately two times higher acceptor: donor elemental ratio is measured in SnO_2 grains, suggesting that Co^{2+} is the only divalent cation that compensates charge of Ta^{5+} on Sn–sites. Furthermore, if the amount of Co^{2+} is limited, a surplus of Ta^{5+} is accumulated at the grain boundaries, preventing densification and this in effect causes unwanted intergranular porosity.

II. Lattice parameters and Co_2SnO_4 secondary phase

XRD data of the samples was quantified by Rietveld refinement to determine the change of lattice parameters and to trace the amount of Co_2SnO_4 secondary phase with increasing Ta_2O_5 addition. Reflections of the spinel-type secondary phase Co_2SnO_4 occurred in the samples with CoO only and those with the addition of ≤ 1 mol% Ta_2O_5. Its formation has important implications to microstructure development and indicates an excess of CoO that is not incorporated into the SnO_2 structure.

III. Electric and dielectric characteristics

Since grain conductivity and nonlinearity are low in the binary SnO_2-CoO system, introduction of Ta_2O_5 into this system drastically affects the conductivity and grain size. With the lowest addition of Ta_2O_5 (0.05 mol%), the average grain size increases 3-times, similarly to the SnO_2-CoO-Nb_2O_5 system. The nonlinear coefficient also increases, and the maximum dielectric constant is observed in this sample. With attention in the varistor ceramics community, we were able to obtain SnO_2-based ceramics suitable for low voltage

applications. Based on the proposed charge compensation mechanism, we were able to propose significant improvements needed to increase densification and optimize related electrical properties of this system.

More on this topic is provided in the article entitled "Charge compensation and electrical characteristics of Ta_2O_5-doped SnO_2-CoO ceramics", written by S. Tominc, A. Rečnik, S. Bernik, M. Mazaj and N. Daneu [170]. For this article, I performed sample preparation, solid-state sintering, XRD sample preparation, heating microscope sample preparation, density measurements, polishing and thermal etching of the samples, SEM/TEM sample preparation, SEM/TEM observations, TEM/EDS analyses, average grain size determination, varistor (I-U) measurements and processing and interpretation of the obtained data together with the listed co-authors. The article is presented on page 47, and its Supporting Information under Appendix B.

Journal of the European Ceramic Society 40 (2020) 355–361

Contents lists available at ScienceDirect

Journal of the European Ceramic Society

journal homepage: www.elsevier.com/locate/jeurceramsoc

Original Article

Charge compensation and electrical characteristics of Ta_2O_5–doped SnO_2–CoO ceramics

Sara Tominc[a,b,*], Aleksander Rečnik[a], Slavko Bernik[a], Matjaž Mazaj[c], Nina Daneu[d]

[a] Jožef Stefan Institute, Department for Nanostructured Materials, Jamova cesta 39, Ljubljana, Slovenia
[b] Jožef Stefan International Postgraduate School, Jamova cesta 39, Ljubljana, Slovenia
[c] National Institute of Chemistry, Department of Inorganic Chemistry and Technology, Hajdrihova 19, Ljubljana, Slovenia
[d] Jožef Stefan Institute, Advanced Materials Department, Jamova cesta 39, Ljubljana, Slovenia

ARTICLE INFO

Keywords:
SnO_2 ceramics
Grain growth
Point defects
Rietveld analysis
Electrical properties

ABSTRACT

We investigated the effect of pentavalent donor dopant Ta_2O_5 on microstructure development, electric and dielectric characteristics of SnO_2–CoO based ceramics. Already low additions of Ta_2O_5 (0.05 mol%) effectively reduce the porosity, improve densification and dielectric permittivity and trigger a 3–fold increase in SnO_2 growth rate. Rietveld analysis shows that the amount of Co_2SnO_4 spinel phase drops with the addition of Ta_2O_5 due to incorporation of Co^{2+} and Ta^{5+} into SnO_2 structure. With higher additions, however, Ta_2O_5 segregates to the grain boundaries and hinders SnO_2 grain growth, which in turn improves electrical properties. TEM/EDS analysis shows that above 0.5 mol% of Ta_2O_5 the Co:Ta ratio in SnO_2 grains is constant 1:2, which means that a twice lower amount of Ta^{5+} is incorporated in the SnO_2 structure compared to the Nb_2O_5-doped SnO_2–CoO system. Accordingly, the following charge compensation mechanism is proposed: 3 $Sn(IV)_{Sn\ (IV)} \leftrightharpoons Co(II)_{Sn}^{''}{}_{(IV)} + 2\ Ta(V)_{Sn\ (IV)}^{'}$.

1. Introduction

Tin dioxide (SnO_2) is an n–type semiconductor with important technological applications due to its wide band gap (~3.5 eV) and high electron mobility [1]. With its microstructural and electrical features, SnO_2–based varistors are promising materials to substitute multi-component ZnO varistors [2–4], especially in high energy applications. SnO_2 crystallizes in the rutile–type structure, so it is expected that SnO_2 would show similar varistor behavior and dielectric properties as TiO_2, which have shown high dielectric constants and nonohmic properties, making it one of the best candidates for diverse capacitor–varistor applications [5,6]. The main problem in SnO_2 ceramics appears to be poor sinterability, sluggish grain growth, and rather high electrical resistivity [7–9]. To address these issues, various dopants, *e.g.* CoO [10–14], MnO_2 [10,15], CuO [14,16], ZnO [17] and Bi_2O_3 [18], that form solid solution with SnO_2, are used to improve densification of SnO_2 ceramics. Further, transition metal oxides, such as Ta_2O_5 or Nb_2O_5, are used to improve electrical conductivity of SnO_2 varistor ceramics [3,11,16,19–26]. Also, the effects of rare earth oxides additions to (Nb/Ta)-doped SnO_2 ceramics were widely studied [19–21].

At high temperatures, undoped SnO_2 densifies poorly due to the surface reduction, and SnO evaporation [27], so it is necessary to stabilize its structure by combined Co and Ta/Nb doping. With the addition of CoO, that acts as an acceptor dopant, densification of SnO_2 is promoted up to 90% and more, through solid state–diffusion [25,28]. In this process, Co^{2+} ions replace Sn^{4+} ions on their regular lattice sites and trigger the formation of charge compensating oxygen vacancies, $V_O^{\cdot\cdot}$, while with donor doping, pentavalent Ta^{5+} (or Nb^{5+}) ions substitute Sn^{4+} and form Sn–site vacancies, $V_{Sn}^{''''}$, that improve electron conductivity of SnO_2 grains [28].

In CoO–Nb_2O_5 doped SnO_2 ceramics, we have recently shown that Nb^{5+} ions compensate for Co^{2+} and Sn^{2+} in an equimolar ratio according to the following charge compensation mechanism: 6 $Sn(IV)_{Sn\ (IV)} \leftrightharpoons Sn(II)_{Sn}^{''}{}_{(IV)} + Co(II)_{Sn}^{''}{}_{(IV)} + 4\ Nb(V)_{Sn\ (IV)}^{'}$ [25]. Comparing electrical properties of Nb, Co-doped SnO_2 varistor system [3], Antunes et al. [22] studied low (0.05 and 0.075 mol%) additions of Ta_2O_5 to the SnO_2-CoO system and demonstrated that Ta_2O_5 can substitute Nb_2O_5 without substantial changes in the electronic properties of SnO_2. In SnO_2 addition of Ta_2O_5 generates $Ta(V)_{Sn\ (IV)}^{'}$ donor defects that increase lattice conductivity of the ceramics [10]. Furthermore, Wang et al. investigated the effects of Ta_2O_5 on the grain size in the SnO_2-Co_2O_3 system and achieved promising electrical characteristics with the addition of 1 mol% of Ta_2O_5, suggesting that an increase of Ta_2O_5 decreases the grain size due to Ta segregation at the grain boundaries.

* Corresponding author at: Department for Nanostructured Materials, Jožef Stefan Institute, Jamova cesta 39, 1000, Ljubljana, Slovenia.
E-mail address: sara.tominc@ijs.si (S. Tominc).

https://doi.org/10.1016/j.jeurceramsoc.2019.09.028
Received 12 July 2019; Received in revised form 13 September 2019; Accepted 15 September 2019
Available online 17 September 2019

In this work we studied the effect of higher additions of Ta_2O_5 (0.05, 0.1, 0.5, 0.75 and 1 mol%) on densification, grain growth, and electrical properties of CoO–Ta_2O_5 doped SnO_2 ceramics, and proposed the most probable charge compensation mechanism based on quantitative energy dispersive spectroscopy analysis. X-ray diffraction data was quantified by Rietveld refinement to determine the change of lattice parameters as well as to trace the amount of Co_2SnO_4 phase with increasing Ta_2O_5 addition. Investigations were aimed to identify experimental conditions to achieve fully dense, pore–free SnO_2–based ceramics with promising electric and dielectric properties for surge protection applications.

2. Experimental procedure

The samples with compositions of (99–x) mol% SnO_2 + 1 mol% CoO + x mol% Ta_2O_5, where x = 0.05, 0.1, 0.5, 0.75 and 1.0, were prepared according to the conventional solid–state sintering method. All compositions were prepared via a standard ceramic procedure by mixing powders of initial oxides SnO_2 (Alfa Aesar, 99.9%, nanopowder), CoO (Alfa Aesar, 95%) and Ta_2O_5 (Alfa Aesar, 99%) in appropriate ratios in an agate mortar, using an agate pestle and homogenized in an absolute ethanol, dried at room temperature and pressed uniaxially at a pressure 150 MPa into 3 mm thick pellets with diameter of 8 mm. The samples were sintered at 1430 °C in an air for 5 h with heating/cooling rates of 5 °C/min.

Densification characteristics of all compositions were recorded using a heating–stage microscope (Hesse Instruments, Osterode am Harz, Germany) up to the maximum operating temperature 1480 °C at a heating rate of 5 °C/min. Phase composition of the sintered samples was analyzed by X–ray diffractometer (PANalytical X'Pert PRO a1 MPD), using Cu–Kα_1 radiation in the range 2θ = 20–80° with a step of 0.034° and recording time of 100 s/step. Quantification of the involved phases were based on the collected powder XRD data and performed by Rietveld analysis within Topas Academic v.6 software package. In the first step, the Rietveld refinement included the whole pattern profile fit, followed by unit cell parameters fit of SnO_2 structure. The structure was modified by replacing Sn^{4+} sites by Ta^{5+} and Co^{2+} atoms in the 2:1 ratio as observed by our EDS analysis, using their total molar contributions above 0.5 mol% Ta_2O_5, while for the samples with lower concentration of Ta_2O_5, due to insignificant contributions, the occupancies of the dopant atoms were not considered in the unit cell refinement procedure. Relative densities (ρ_{rel}) of the sintered samples were measured using the Archimedes method according to the equation $\rho_{rel} = \rho/\rho_{theor} \cdot 100\%$, where ρ_{theor} = 6.95 g/cm^3.

For microstructural observations, the samples were cut in half and mounted in acrylic resin. Cross–sections of the samples were mechanically ground and polished down to 0.25 μm roughness. Polished cross–sections were then thermally etched at 1280 °C for 10 min to reveal the microstructural features. The samples were investigated on field–emission scanning electron microscope (FEG–SEM; JSM–7600 F, Jeol Ltd., Tokyo, Japan) and transmission electron microscopy (TEM) using a 200–kV FEG–TEM (JEM–2010 F, Jeol Ltd., Tokyo, Japan) with an energy dispersive X–ray spectrometer (EDS; Oxford Instruments ISIS 300 EDS) for semi-quantitative chemical analysis of grain boundaries and grains.

For electrical characterization, silver electrodes were deposited on both faces of sintered pellets and fired at 600 °C for 15 min. Current–voltage measurements were taken using a high–voltage source meter (Keithley 2410, Keithley Instruments Inc., Cleveland, USA). Nominal varistor voltages (U_N) were measured at current densities J_1 = 1 mA/cm^2 and J_2 = 10 mA/cm^2, leakage currents I_L (μA) at 0.75 U_N (1 mA/cm^2) and sample thickness d (mm). The threshold voltage was calculated as $U_T = U_N/d$, and coefficient α was obtained by $\alpha = d\log J/d\log U$. Dielectric properties were measured using inductance/capacitance/resistance (LCR) meter (Model 4284A; Hewlett–Packard, USA) at frequencies from 20 Hz to 1 MHz at room temperature. Dielectric permittivity (ε) was calculated by the equation $\varepsilon = C{\cdot}d/A{\cdot}\varepsilon_0$, where C is the capacitance, d is the thickness of the sample, A is the surface of the sample and $\varepsilon_0 = 8.854 \cdot 10^{-12}$ F/m is the permittivity of a vacuum. The dielectric loss was measured as tan δ, where δ represent the phase angle between the signal of the sample and the signal, expected for an ideal lossless capacitor.

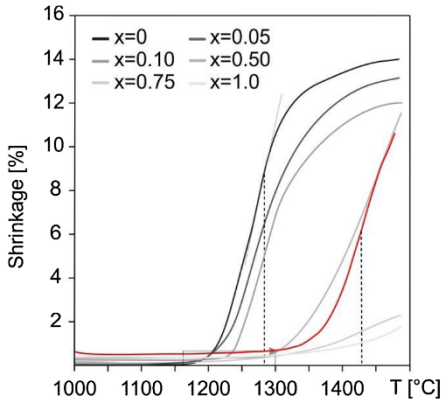

Fig. 1. Densification curves of investigated SnO_2–CoO–Ta_2O_5 samples. With the addition of Ta_2O_5 the onset of densification is shifted to higher temperatures while densification is becoming slow. Sintering curve for SnO_2–CoO–1 mol% Nb_2O_5 ceramics (red line, from Ref. [25]) is shown for comparison.

3. Results

3.1. Densification and microstructure development

Densification curves of investigated samples are shown in Fig. 1. The binary composition of SnO_2 with 1 mol% CoO starts to densify at ~1160 °C, and reaches the maximum densification rate at 1280 °C. The smallest addition of 0.05 mol% Ta_2O_5 does not affect the onset of densification, however the shrinking rate is suppressed. Higher additions of Ta_2O_5 shift the onset of sintering to higher temperatures; *i.e.* the sample with 0.5 mol% Ta_2O_5 starts to densify above 1300 °C, while even higher Ta_2O_5 additions are reflected in a further increase of the onset of densification. It is interesting to note that the sample with 0.5 mol% Ta_2O_5 addition shows similar densification behavior as the sample with 1 mol% Nb_2O_5 (twice as high addition of a donor dopant) clearly indicating different roles of Ta_2O_5 and Nb_2O_5 on densification and microstructure development in the SnO_2–CoO system. Based on the results of densification analysis, the optimum sintering temperature of 1430 °C was selected for our study.

Phase compositions of the samples sintered at 1430 °C for 5 h are shown on Fig. 2. A predominant phase is tetragonal SnO_2 (cassiterite; $P4_2/mnm$) with rutile-type structure and approximate unit-cell parameters: a = 4.739 Å and c = 3.188 Å. As expected, the addition of CoO and small quantities of Ta_2O_5 (up to 0.01%) does not change the unit cell parameters significantly, since the contribution of dopants are too low to have any notable effect on SnO_2 structure (Table 1). With higher amounts of Ta_2O_5 (≥ 0.5%), the changes in unit cell parameters become apparent, showing a decrease in c-axis with increasing Ta_2O_5 additions (*see* Table 1); most probably due to the smaller ionic radii of Ta^{5+} and Co^{2+} in comparison to that of Sn^{4+}. Moreover, the addition of CoO to SnO_2 causes the formation of significant amounts of Co_2SnO_4, a cubic cobalt stannate phase with a spinel-type structure, that is indicated by weak reflections in XRD patterns (Fig. 2). The contribution of this phase within the bulk samples consistently decreases as the

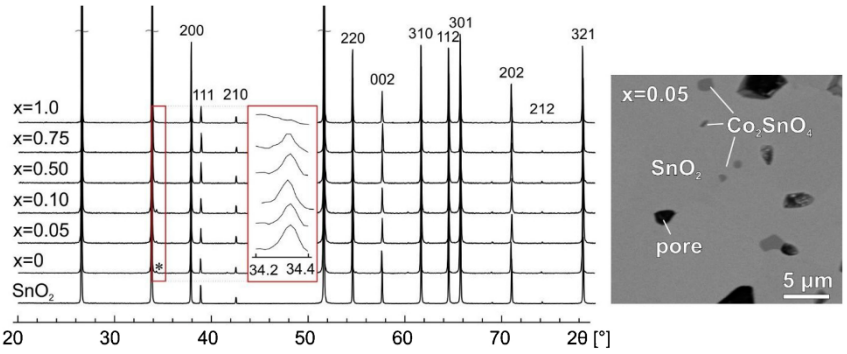

Fig. 2. X–ray diffraction patterns of the samples with compositions (99–x)% SnO_2 + 1% CoO + x% Ta_2O_5 after sintering at 1430 °C for 5 h. Outlined reflections with asterisk denote reflections of Co_2SnO_4 appearing for compositions below x = 1.0 at 2θ ≈ 34.3°. Back-scattered SEM image (on the right) showing the presence of micron-sized dark-grey Co_2SnO_4 spinel phase in light-grey SnO_2 matrix, as well as at the GBs of the polished SnO_2-CoO sample with the addition of Ta_2O_5 (x = 0.05 mol%).

Table 1
Results of SnO_2 unit cell dimensions and quantification of SnO_2/Co_2SnO_4 phase content (mol %) for all (99–x)% SnO_2 + 1% CoO + x% Ta_2O_5 compositions after Rietveld refinement.

Sample	Unit cell dimensions for SnO_2 ($P4_2/mnm$ symmetry) a(Å) c(Å) V(Å^3)	Phase content (mol %) SnO_2 Co_2SnO_4
SnO_2	4.73925(5) 3.18777(3) 71.599(2)	100 -
SnO_2 + 1% CoO	4.73931(6) 3.18785(5) 71.602(2)	99.77(2) 0.23(2)
… + 0.05%Ta_2O_5	4.73916(8) 3.18780(6) 71.597(2)	99.80(1) 0.20(1)
… + 0.10%Ta_2O_5	4.73941(8) 3.18780(6) 71.604(3)	99.84(2) 0.16(2)
… + 0.50% Ta_2O_5	4.73931(7) 3.18707(5) 71.585(2)	99.90(2) 0.10(2)
… + 0.75% Ta_2O_5	4.73924(7) 3.18664(5) 71.573(2)	99.96(1) 0.04(1)
… + 1.00% Ta_2O_5	4.73926(6) 3.18662(5) 71.574(2)	99.97(2) 0.03(2)

amount of added Ta_2O_5 is increasing.

The presence of Co_2SnO_4 phase is observed in XRD below 1.0 mol% of Ta_2O_5, while for higher additions its intensity drops below the background. In comparison to the similar SnO_2–CoO–Nb_2O_5 system [25], the peaks of Co_2SnO_4 spinel phase were not observed with Nb_2O_5 additions higher than 0.5 mol%. Decrease of the spinel phase formation is directly related to simultaneous incorporation of lower (2+ or 3+) and higher (5+) charge dopants with respect to the Sn^{4+} into the SnO_2 structure. The results suggest that at identical CoO addition, a lower amount of tantalum is incorporated into SnO_2 in comparison to Nb_2O_5.

To further investigate this issue, we examined the composition of grain boundaries (GBs) and SnO_2 grains by TEM/EDS analysis (Fig. 3). We observe, that the amount of Ta in SnO_2 grains is about one-half lower than in the Nb_2O_5-system for similar sintering conditions and comparable additions of dopants, indicating that less Ta^{5+} is incorporated in SnO_2 than Nb^{5+}. In the sample with 0.1 mol% addition of Ta_2O_5 (Fig. 3a), lower amounts of both dopants were detected in SnO_2 grains, so the quantification of the results was not reliable due to low amounts of both dopants. For the samples that show only 0.03-0.04 mol % of secondary Co_2SnO_4 phase (x ≥ 0.75 mol%) the compositions with respect to the Co:Ta ratio within SnO_2 grains are steady and approach the value of 1:2, whereas at the GBs, the amount of Co is higher, indicating lower GB diffusivity of tantalum in comparison to niobium [25]. Consistently with GB segregation study in Ta_2O_5–doped SnO_2 ceramics, by Filho et al. [30,31], we observe that the concentration of Co and Ta at GBs is ~2-times higher than that in the adjacent SnO_2 grains, which is also reflected in the fact that the Co_2SnO_4 spinel reflections disappear from XRD with the increasing addition of Ta_2O_5.

The influence of Ta_2O_5 additions on the microstructural characteristics of SnO_2–CoO ceramics was further investigated by SEM. The microstructures of the samples are shown in Fig. 4. Binary SnO_2–CoO sample has a fine grained microstructure with SnO_2 grains with an average grain size of about 3.4 μm and ~10% intergrannular porosity. By the smallest addition of Ta_2O_5 (x = 0.05) the porosity is significantly reduced, while the average grain size abruptly increases to 9.3 μm, with individual SnO_2 grains reaching 20 μm. Twin boundaries (TBs) are common. With increasing addition of Ta_2O_5 fully dense microstructure is never achieved; SnO_2 grain size gradually decreases, while the porosity increases, reaching 33% for the x = 1.0 sample. This indicates a strong influence of Ta_2O_5 doping on diffusion processes in the SnO_2–CoO system. Relative densities (ρ_{rel}) and average grain sizes (d) of the samples are listed in Table 2.

Along with drastic microstructural changes, the increasing addition of Ta_2O_5 is also reflected in abundant twinning of SnO_2 [32]. Fig. 5a shows TBs visible in SnO_2 grains. Cyclic twins, similar to those observed in the Nb_2O_5-doped SnO_2 [25] are common. Bright-field TEM image with the corresponding electron diffraction pattern (Fig. 5b) confirms that TBs lie in (101) planes. No dopant could be detected in excess amounts at the TB planes by EDS, even with 0.2 nm beam diameter located at the TB, suggesting that the twin boundaries are not chemically induced.

3.2. Electric and dielectric characteristics of Ta_2O_5-doped SnO_2 ceramics

Pure SnO_2 does not show nonlinear behavior, however, already the addition of CoO generates a measurable varistor effect with a threshold voltage U_T of 69 V/mm and nonlinearity coefficient α = 6. Varistor properties of SnO_2 ceramics are improved by addition of Ta_2O_5. Already at x = 0.05, U_T and α increase for a factor of 2, while with higher Ta_2O_5 additions the coefficients only slightly increase up to x = 1.0, where the varistor properties start to deteriorate (Fig. 6). This suggests that only appropriate addition of Ta_2O_5 can improve nonohmic behavior, while beyond that limit the nonlinearity is destroyed. Mean values of α, U_T and voltage drop per grain boundary U_{GB}, determined by: $U_{GB} = U_T/N$, are summarized in Table 2. U_{GB} increased to 1.73 V for x = 0.75 sample, where the optimum nonlinear characteristics were obtained for our compositions.

To examine the relation between grain size and the electrical characteristics of ceramics, we measured the impedance at room temperature and at fixed frequency of 1 kHz for all samples with different Ta_2O_5 additions. The obtained results (Fig. 7) show that dielectric permittivity (ε) is increased only slightly from 2675 for the SnO_2–CoO sample to 3062

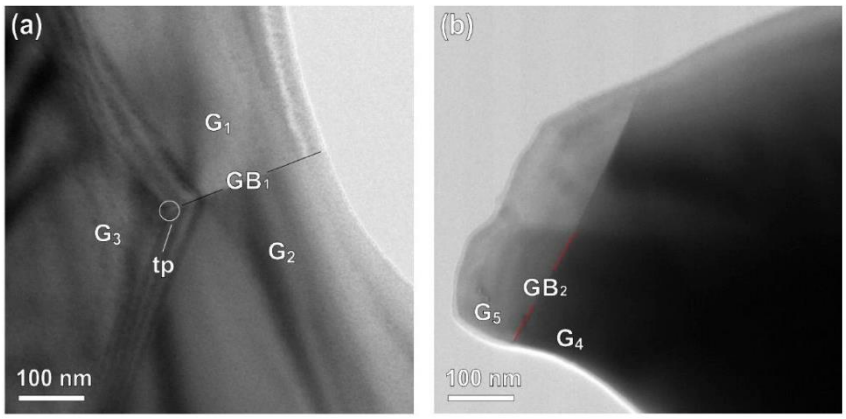

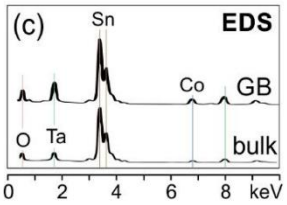

Location	G1	G2	G3	Gb_1	tp	G4	G5	Gb_2
Co-K [at%]	0.23	0.19	0.06	1.13	0.18	0.91	1.00	2.44
Ta-K [at%]	0.08	0.12	0.03	0.20	0.07	1.95	1.98	3.55
Ta/Co	0.35	0.63	0.50	0.18	0.39	2.14	1.98	1.45

Fig. 3. TEM/EDS analysis of grains and GBs in SnO_2–1 mol% CoO samples with the addition of (a) 0.1 mol% and (b) 1 mol% of Ta_2O_5, where Co^{2+} and Ta^{5+} began to dominate at the GBs, as well as in the SnO_2 grains, and consequently the secondary phase Co_2SnO_4 disappeared. (c) EDS spectra in bulk SnO_2 and at the GB with corresponding EDS analysis from locations marked in (a) and (b).

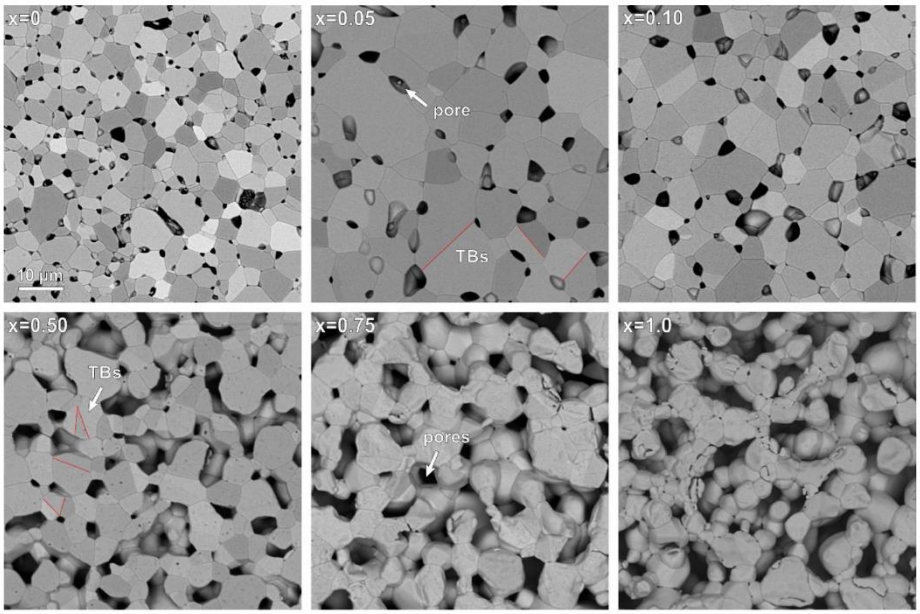

Fig. 4. SEM/BSE images of thermally etched cross–sections of SnO_2–1 mol% CoO ceramics with different Ta_2O_5 additions (x = 0–1.0 mol%). The presence of twin boundaries (TBs) in the samples is marked by red lines. All samples show some porosity, increasing with x.

Table 2
Relative density ρ_{rel}, average grain size d, with basic varistor properties: threshold voltage U_T, non–linearity coefficient α, leakage current I_L, voltage drop per grain boundary U_{GB} and dielectric permittivity ε at fixed frequency 1 kHz with dielectric losses tan δ of the Ta_2O_5-doped SnO_2–CoO samples.

Sample	ρ_{rel}* [%]	d [μm]	U_T [V/mm]	α	I_L [μA]	U_{GB} [V]	ε	tan δ
SnO_2 [25]	55.7 ± 2.1	~0.1 ÷ 1.0	n/a	n/a	n/a	n/a	n/a	n/a
SnO_2 + 1% CoO [25]	90.3 ± 1.3	3.4 ± 1.5	69 ± 1	6	66.5	0.24	2675	0.085
… + 0.05% Ta_2O_5	97.3 ± 1.0	9.3 ± 3.9	152 ± 2	14	9.6	1.41	3062	0.066
… + 0.10% Ta_2O_5	89.1 ± 1.6	6.9 ± 3.0	155 ± 3	15	8.7	1.07	2922	0.069
… + 0.50% Ta_2O_5	76.1 ±1.3	5.6 ± 1.9	271 ± 5	15	5.7	1.51	949	0.069
… + 0.75% Ta_2O_5	72.4 ± 1.5	~5.0 ÷ 3.0	346 ± 8	18	5.9	1.73	548	0.061
… + 1.00% Ta_2O_5	66.4 ±1.9	~5.0 ÷ 1.0	232 ± 9	7	68.0	0.46	361	0.059

* theoretical density: $\rho_{theor} = 6.95\ g/cm^3$.

for the lowest addition of Ta_2O_5 (x = 0.05), with low dielectric loss of 0.066 at frequency of 1 kHz. With further addition of Ta_2O_5 (x > 0.1), the dielectric permittivity decreases, which is related to the increasing sample porosity and grain size of the samples (*see* Table 2).

4. Discussion

4.1. The effect of Ta_2O_5 doping on microstructure development of SnO_2 ceramics

Similar to the Nb_2O_5–doped system [25], Ta_2O_5-doped SnO_2–CoO ceramics shows a strong dependence on dopant additions and ratios. As both dopants are pentavalent, we could expect same charge compensation mechanism and similar tendencies in grain growth. Like in Nb_2O_5, already the smallest addition of Ta_2O_5 to SnO_2–CoO ceramics triggered exaggerated grain growth and improved densification of the ceramic, while for higher additions reduction of grain size and the increase of porosity is observed [33]. This effect has been explained by enhanced tin self–diffusion for low concentrations of V + dopants, whereas higher additions may have an inhibiting effect through GB segregation [26,34,35]. Decreased SnO_2 grain size at higher Ta_2O_5 additions suggests, that Ta^{5+} segregates to grain boundaries and hinders diffusion processes. Moreover, a simple densification study indicated additional retarding effect in the case of Ta_2O_5 additions, suggesting sluggish GB mobility compared to the Nb_2O_5 system, that could also be responsible for the observed increase of intergrannular porosity [34].

Since the solid solubility limit of CoO in SnO_2 is ~0.5 mol% [12,36], another distinction from the Nb_2O_5 system are considerably lower solid solubility of Ta in SnO_2 and consistently higher Co:Ta ratio, as shown by our TEM/EDS analysis. With the addition of Ta_2O_5, the secondary Co_2SnO_4 phase is formed as long as some Co remains unincorporated in the SnO_2 structure. Co_2SnO_4 grains can be found at GBs as well as inside the SnO_2 grains [12,36,37], having no drastic influence to GB mobility and microstructure development. Together with segregated Ta^{5+}, it probably inhibits grain growth, however, with higher Ta_2O_5 doping, Co_2SnO_4 phase slowly disappears, due to charge compensation between $Co(II)_{Sn}^{''}{}_{(IV)}$ and $Ta(V)_{Sn}^{\cdot}{}_{(IV)}$ [12,25].

While in Nb_2O_5-doped SnO_2 the amount of dissolved Nb in SnO_2 grains is ~4 at% [25], amount of Ta that is dissolved in Ta_2O_5-doped SnO_2 is 2× lower. On the other hand, the amount of Co^{2+} drawn with Ta^{5+} to compensate for $Sn(IV)_{Sn}^{\cdot\cdot}{}_{(IV)}$ vacancies that are generated at the surface of SnO_2 grains is equal than that in the Nb_2O_5 system [25], *i.e.* Co:Ta = 1:2 in Ta_2O_5-doped SnO_2 and Co:Nb = 1:4 in Nb_2O_5-doped SnO_2, respectively, both co-doped with 1 mol% of CoO. 2× higher Co:Ta ratio suggests that Co^{2+} is the only divalent cation that compensates the charge of Ta^{5+} on Sn–sites, according to the following charge compensation mechanism:

$$3\ Sn(IV)_{Sn}^{\cdot}{}_{(IV)} \leftrightharpoons Co(II)_{Sn}^{''}{}_{(IV)} + 2\ Ta(V)_{Sn}^{\cdot}{}_{(IV)} \quad (3)$$

This suggests that unlike in the Nb_2O_5 system, where four Nb^{5+} stabilized one Sn^{2+} and one Co^{2+} on Sn-sites [25], here $2e^-$ charged Sn–sites, changed by acceptor dopant Co^{2+}, are compensated by two positively charged Sn–sites, occupied by donor dopant Ta^{5+}, while Sn^{2+} evaporates. While Sn^{2+} evaporates under low oxygen partial pressures at temperatures >1300 °C unless it is stabilized with CoO [14,27], Ta^{5+}, like Nb^{5+} [12], is expected to have an inhibiting effect on densification of SnO_2. If Sn^{2+} evaporates and the amount of Co^{2+} is limited, a surplus of Ta^{5+} is accumulated at the GBs, preventing densification and causing intergrannular porosity in this system [34].

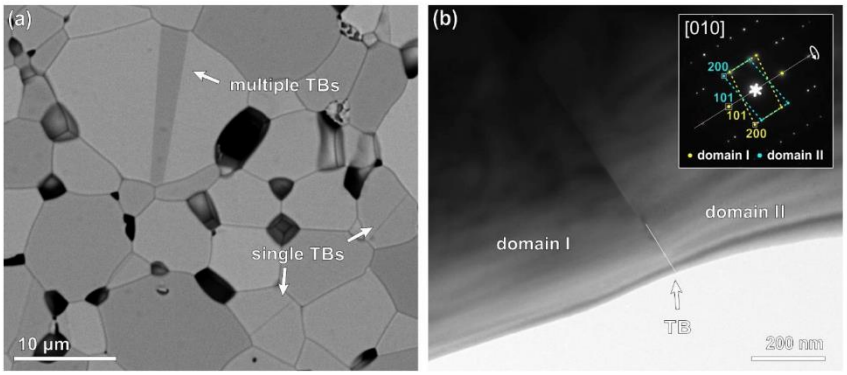

Fig. 5. Twinning in (Co,Ta)–doped SnO_2 ceramics. (a) SEM/BSE image of the x = 0.1 sample. Multiple and single twin boundaries are observed in SnO_2 grains due to different orientation of SnO_2 domains. (b) Low–magnification TEM image (x = 1.0) of (101) twin boundary with the corresponding electron diffraction pattern.

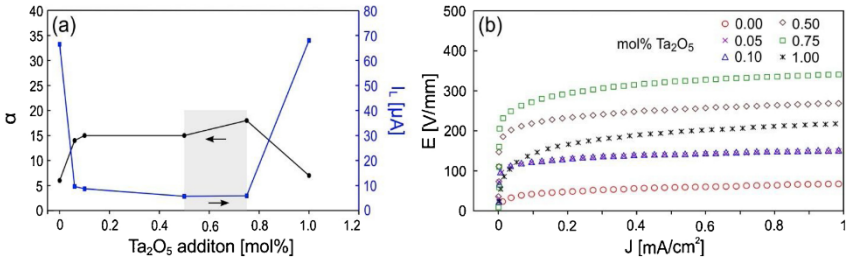

Fig. 6. (a) Nonlinear coefficient, α and leakage current, I_L of the SnO_2–1 mol% CoO samples doped with different amounts of Ta_2O_5 (x = 0.0 ÷ 1.0 mol%), sintered at 1430 °C for 5 h. Samples with Ta_2O_5 additions between 0.5 and 0.75 mol% show best nonlinear properties (shaded area). (b) Applied electric field, E, as a function of current density, J, of the SnO_2–1 mol% CoO–x mol% Ta_2O_5 samples.

4.2. Electric and dielectric characteristics

Defect formation by CoO and Ta_2O_5 additions in SnO_2 ceramics is responsible for the origin of the potential barriers at GBs. While ionic radius of Co^{2+} is close to the ionic radius of Sn^{4+}, Co^{2+} easily dissolves in the SnO_2 lattice and thus facilitates the formation of oxygen vacancies, leading to better densification. The introduction of small amounts of Ta^{5+} to the SnO_2–CoO system leads to the concentration of electrons and $V_{S}^{\cdot\cdot}{}_{n}$, which improves electrical conductivity of SnO_2 [22]. To generate varistor effect in SnO_2, it is crucial to add CoO to produce electron charge barriers at grain boundaries and form solid solution, which in turn influences SnO_2 grain growth. The addition of CoO creates oxygen vacancies $V_O^{\cdot\cdot}$, which substitute Sn^{4+} ions on their regular sites. However, acceptor additives lead to highly resistive material [5–9]. When there are no secondary phases at the GBs, defect formation by acceptor and donor dopants in the SnO_2 matrix should be responsible for the origin of the Schottky barriers at the GBs [28,30,33]. The electric conductivity of the SnO_2–CoO–Ta_2O_5 system thus be greatly increased with Ta_2O_5 doping [38,39], where the amount of Co_2SnO_4 secondary phase consistently decreased. With Ta_2O_5 addition until 0.05 mol% the average grain size and nonlinear coefficient increases. Larger amounts of Ta_2O_5 introduced in the SnO_2–CoO system, however, results in inhibited grain growth [29], while the excess of Ta_2O_5 (1 mol%) also reduces the conductivity.

The electric behavior of the system without Ta_2O_5 shows weak nonlinearity and very low breakdown voltage due to weakly conductivity of the grains, while introduction of 0.05 mol% of Ta_2O_5 drastically increases the grain size and decreases grain resistance. 3–times larger average grain size reflects in a 6–fold increase of the nominal breakdown voltage per GB (U_{GB} = 1.41 V). The coefficient of nonlinearity increases from 6 to 14. In the samples with 0.10 ÷ 0.75 mol% of Ta_2O_5, the nonlinear coefficient increases only slightly to 18, due to high porosity of the samples. The reason for increased porosity may be the surplus of donors at the grain boundaries, which suppress the grain growth [30]. In addition, the increase of the threshold voltage U_T to ~350 V/mm with increased Ta_2O_5 doping up to 0.75 mol% is mainly attributed to the decrease in grain size. For this composition also the average U_{GB} increases to 1.73 V. Higher addition of Ta_2O_5 (1.0 mol%) results in a complete collapse of nonlinearity and a drastic increase of leakage current.

In addition to varistor properties, the Ta_2O_5-doped SnO_2 samples also show a colossal dielectric permittivity (CP $>10^3$) that has attracted a lot of attention. CP has been observed in (Zn + Co) and (Al + Nb) co–doped SnO_2 ceramics [40,41] with a low dielectric loss across a wide range of frequencies. In our SnO_2–CoO– 0.05 mol% Ta_2O_5 sample we observed comparable values with the CPs ~3000 and low dielectric losses of 0.06 at 1 kHz, however the permittivity gradually decreased with increasing Ta doping concentration. In the dielectric behavior in CP ceramics, the resistance of the grains and grain boundaries play an important role. Ta doping in SnO_2 as donor dopant introduce many n–type carriers, while Co as an acceptor dopant can capture the electrons introduced by Ta donor doping, increasing the resistance of GB and grain. Therefore, by varying the ratio between Ta^{5+} and Co^{2+}, we could get high dielectric permittivity and low dielectric losses [41].

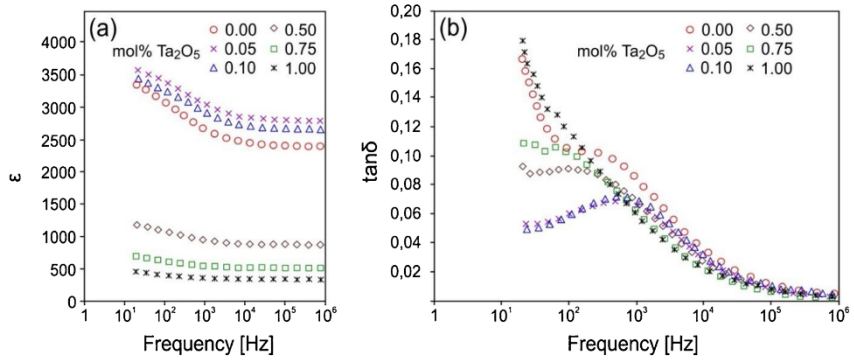

Fig. 7. (a) Dielectric permittivity versus frequency with different content of Ta_2O_5 dopant. (b) Dielectric loss versus frequency for all SnO_2–1 mol% CoO–x mol% Ta_2O_5 samples.

5. Conclusions

(Co,Ta)–doped SnO_2 ceramics were investigated with special attention on charge compensation mechanism and electrical characteristics. The results confirmed that proper amount of donor dopant Ta_2O_5 (0.05 mol%) and acceptor dopant CoO (1.0 mol%) enhanced the sintering and promoted the grain growth. Hence, this composition reaches the highest relative density (98%) and best dielectric characteristics. The increasing amount of Ta_2O_5 dopant has strong influence on the grain growth process and hinders diffusion processes. TEM/EDS analysis confirmed segregation of Ta^{5+} at the GBs, shifting the maximum shrinkage temperature higher than 1480 °C, which results to increase of porosity. The incorporation of Ta^{5+} and Co^{2+} in constant 2:1 ratio suggests that lower amount of tantalum is incorporated in the SnO_2 structure compared to the Nb_2O_5-doped SnO_2-CoO system. Although the Ta_2O_5 doped SnO_2–CoO based varistor is suitable for low voltage applications, the work for further improving the densities and increase the performance of this system is under way.

Acknowledgements

The authors gratefully acknowledge David Fabjan for dielectric measurements and Silvo Zupančič for recording densification characteristics on heating-stage microscope (both from the Advanced Materials Department, Jožef Stefan Institute). This work was supported by the Slovenian Research Agency under The Project No. J1-9177 and Z1-4202 and is based in part on the Ph.D. Thesis of S. Tominc under the contract No. 0106/37484.

References

[1] H. Wang, A.L. Rogach, Hierarchical SnO_2 nanostructures: recent advances in design, synthesis, and applications, Chem. Mater. 26 (2014) 123–133.
[2] P.R. Bueno, J.A. Varela, E. Longo, SnO_2, ZnO and related polycrystalline compound semiconductors: An overview on the voltage dependent resistance (non–ohmic) feature, J. Eur. Ceram. Soc. 28 (2008) 505–529.
[3] S.A. Pianaro, P.R. Bueno, E. Longo, J.A. Varela, A new SnO_2–based varistor system, J. Mater. Sci. Lett. 14 (1995) 692–694.
[4] Z.Y. Lu, A.B. Glot, A.I. Ivon, Z.Y. Zhou, Electrical properties of new tin dioxide varistor ceramics at high currents, J. Eur. Ceram. Soc. (2012) 3801–3807.
[5] Z. Yao, Z. Song, H. Hao, Zh. Yu, M. Cao, Sh. Zhang, M.T. Lanagan, H. Liu, Homogeneous/ inhomogeneous-structured dielectrics and their energy-storage performances, Adv. Mater. 1601727 (2017) 1–15.
[6] A.B. Glot, R. Bulpett, A.I. Ivon, P.M. Gallegos-Acevedo, Electrical properties of SnO_2 ceramics for low voltage varistors, Phys. B: Phys. Condens. Matter. 457 (2015) 108–112.
[7] J.A. Varela, O.J. Whittemore, E. Longo, Pore size evolution during sintering of ceramic oxides, Ceram. Int. 16 (1990) 177–189.
[8] E.R. Leite, J.A. Cerri, E. Longo, J.A. Varela, C.A. Paskocima, Sintering of ultrafine undoped SnO_2 powder, J. Eur. Ceram. Soc. 21 (2001) 669–675.
[9] E. Medvedovski, Tin oxide–based ceramics of high density obtained by pressureless sintering, Ceram. Int. 43 (2017) 8396–8405.
[10] J.A. Cerri, E.R. Leite, D. Gouvêa, E. Longo, Effect of cobalt(II) oxide and manganese (IV) oxide on sintering of tin(IV) oxide, J. Am. Ceram. Soc. 79 (1996) 799–804.
[11] G. Branković, Z. Branković, M.R. Davolos, M. Cilense, J.A. Varela, Influence of the common varistor dopants (CoO, Cr_2O_3 and Nb_2O_5) on the structural properties of SnO_2 ceramics, Mater. Charact. 52 (2004) 243–251.
[12] D.G. Chang, J.H. Lee, J.J. Kim, Grain growth kinetics of cobalt–doped SnO_2 by varying Nb_2O_5 content, Mater. Sci. Forum. 534–536 (2007) 529–532.
[13] R. Metz, D. Koumeir, J. Morel, J. Pansiot, M. Houabes, M. Hassanzadeh, Electrical barriers formation at the grain boundaries of Co–doped SnO_2 varistor ceramics, J. Eur. Ceram. Soc. 28 (2008) 829–835.
[14] T.S. Zhang, L.B. Kong, X.C. Song, Z.H. Du, W.Q. Xu, S. Li, Densification behavior and sintering mechanisms of Cu– or Co–doped SnO_2: a comparative study, Acta Mater. 62 (2014) 81–88.
[15] A.L.W. Buonocore, R. Mouta, J.C. Gomes, C.C. dos Santos, E.M. Diniz, M.C. Castro Junior, J.H.G. Rangel, F.M.R. Borges, F.H. Silva Sales, M.M. Oliveira, Varistor behavior in a ternary system based on SnO_2 doped with a hexavalent donor: SnO_2-MnO_2-WO_3, J. Alloys Compd. (2019), https://doi.org/10.1016/j.jallcom.2019.07.250.
[16] C.M. Wang, J.F. Wang, W.B. Su, G.Z. Zang, P. Qi, Effects of Ta_2O_5 on the electrical properties of SnO_2-CuO ceramics, J. Phys. D Appl. Phys. 38 (2005) 1485–1488.
[17] C.R. Foschini, L. Perazolli, J.A. Varela, Sintering of tin oxide using zinc oxide as a densification aid, J. Mater. Sci. 39 (2004) 5825–5830.
[18] M. Malekí Shahraki, M.A. Bahrevar, S.M.S. Mirghafourian, A.B. Glot, Novel SnO_2 ceramic surge absorbers for low voltage applications, Mater. Lett. 145 (2015) 355–358.
[19] C.M. Wang, J.F. Wang, H.C. Chen, W.B. Su, G.Z. Zang, P. Qi, Effects of Er_2O_3 on electrical properties of the SnO_2-CoO-Ta_2O_5 varistor system, Chin. Phys. Lett. 21 (2004) 716.
[20] C.M. Wang, J.F. Wang, W.B. Su, H.C. Chen, C.L. Wang, J.L. Zhang, G.Z. Zang, P. Qi, Z.G. Gai, B.Q. Ming, Improvement in the nonlinear electrical characteristics of SnO_2 ceramic varistors with Dy_2O_3 additive, Mater. Sci. Eng. B 127 (2006) 112–116.
[21] I.P. Silva, A.Z. Simões, F.M. Filho, E. Longo, J.A. Varela, L. Perazolli, Dependence of La_2O_3 content on the nonlinear electrical behaviour of ZnO, CoO and Ta_2O_5 doped SnO_2 varistors, Mater. Lett. 61 (2007) 2121–2125.
[22] A.C. Antunes, S.R.M. Antunes, S.A. Pianaro, M.R. Rocha, E. Longo, J.A. Varela, Nonlinear electrical behaviour of the SnO_2-CoO-Ta_2O_5 system, J. Mater. Sci. Lett. 17 (1998) 577–579.
[23] C.M. Wang, J.F. Wang, W.B. Su, H.C. Chen, G.Z. Zang, P. Qi, Microstructure development and nonlinear electrical characteristics of the SnO_2-CuO-Ta_2O_5 based varistors, J. Mater. Sci. 40 (2005) 6459–6462.
[24] M.G. Masteghin, R.C. Bertinotti, M.O. Orlandi, High-performance and low-voltage SnO_2-based varistors, Ceram. Int. 43 (2017) 13759–13764.
[25] S. Tominc, A. Rečnik, Z. Samardžija, G. Dražić, M. Podlogar, S. Bernik, N. Daneu, Twinning and charge compensation in Nb_2O_5–doped SnO_2–CoO ceramics exhibiting promising varistor characheristics, Ceram. Int. 44/2 (2018) 1603–1613.
[26] A.E. Bondarchuk, A.B. Glot, A.R. Velasco–Rosales, Effects of Sb and Nb dopants on electrical and microstructural properties of low–voltage varistor ceramics based on SnO_2, Ceram. Int. 44 (2018) 7844–7859.
[27] C.L. Hoenig, A.W. Searcy, Knudsten and Langmuir evaporation studies of stannic oxide, J. Am. Ceram. Soc. 49 (1966) 177–189.
[28] S.R. Dhage, V. Choube, V. Ravi, Nonlinear I–V characteristics of doped SnO_2, Mater. Sci. Eng. B 110 (2004) 168–171.
[29] C. Wang, J. Wang, H. Chen, W. Wang, W. Su, G. Zang, P. Qi, Effects of Ta_2O_5 on the grain size and electrical properties of SnO_2-based varistors, J. Phys. D Appl. Phys. 36 (2003) 3069–3072.
[30] F.M. Filho, A.Z. Simões, A. Ries, E.C. Souza, L. Perazolli, M. Cilense, E. Longo, J.A. Varela, Investigation of electrical properties of tantalum doped SnO_2 varistor system, Ceram. Int. 31 (2005) 399–404.
[31] F.M. Filho, A.Z. Simões, A. Ries, I.P. Silva, L. Perazolli, E. Longo, J.A. Varela, Influence of Ta_2O_5 on the electrical properties of ZnO– and CoO–doped SnO_2 varistors, Ceram. Int. 30 (2004) 2277–2281.
[32] F. Kawamura, M. Kamei, I. Yasui, Effect of impurity cations on the growth and habits of SnO_2 crystals in the SnO_2–Cu_2O flux system, J. Am. Ceram. Soc. 82 (1999) 774–776.
[33] A.C. Antunes, S.M. Antunes, S.A. Pianaro, E. Longo, J.A. Varela, Effect of Ta_2O_5 doping on the electrical properties of $0.99SnO_2 \cdot 0.01CoO$ ceramic, J. Mater. Sci. 35 (2000) 1453–1458.
[34] A.E. Montes Mejía, M.I. Pech–Canul, M.B. Hernández, S. García–Villarreal, C. Gómez Rodríguez, J.A. Aguilar–Martínez, Grain refinement and non–ohmic properties in (Co,Ta)–doped SnO_2 ceramics by Cr_2O_3 additions and the in situ formation of $CoCr_2O_4$, Appl. Phys. A 124 (2018) 474.
[35] G. Hu, J. Zhu, H. Yang, F. Wang, Effect of Cr_2O_3 addition on the microstructure and electrical properties of SnO_2-based varistor, J. Mater. Sci. Mater. Electron. 24 (2013) 1735–1740.
[36] B.C. Kim, J.I. Jung, J.H. Lee, J.J. Kim, Precipitate concentration of Co2SnO4 in CoO-doped SnO_2 ceramics at different oxygen chemical potentials, Solid State Ion. 144 (2001) 321–327.
[37] M.L. Moreira, S.A. Pianaro, A.V.C. Andrade, A.J. Zara, Crystal phase analysis of SnO_2-based varistor ceramic using the Rietveld method, Mater. Charact. 57 (2006) 193–198.
[38] A. Dibb, S.M. Tebcherani, M.R. Santos, M. Cilense, J.A. Varela, E. Longo, MnO_2 influence on the electrical propertis of SnO_2–based ceramic system, Key Eng. Mater. 189–191 (2001) 161–165.
[39] S.R. Dhage, V. Ravi, Influence of various donors on nonlinear I-V characteristics of tin dioxide ceramics, Appl. Phys. Lett. 83 (2003) 4539–4541.
[40] K. Rajwali K, M.H. Fang, Dielectric and magnetic properties of (Zn,Co) co–doped SnO_2 nanoparticles, Chin. Phys. B 24 (2015) 127803.
[41] Y. Song, X. Wang, X. Zhang, X. Qi, Z. Liu, L. Zhang, Y. Zhang, Y. Wang, Y. Sui, B. Song, Colossal dielectric permittivity in (Al + Nb) co–doped rutile SnO_2 ceramics with low loss at room temperature, Appl. Phys. Lett. 109 (2016) 142903.

Chapter 5

Microstructure Development in (Co,Ta)-Doped SnO_2-Based Ceramics with Promising Electric and Dielectric Properties

In Chapter 4, I have shown that Co^{2+} compensates the surplus charge of Ta^{5+} on Sn-sites according to the following compensation mechanism:

$$3\ \mathrm{Sn(IV)}^{\times}_{\mathrm{Sn\,(IV)}} \rightleftharpoons\ \mathrm{Co(II)}^{''}_{\mathrm{Sn\,(IV)}} + 2\ \mathrm{Ta(V)}^{\cdot}_{\mathrm{Sn\,(IV)}}$$

In this Chapter, I studied the effects of higher additions of CoO (1-4 mol%) on densification and grain growth to find the optimal experimental conditions for improved varistor and dielectric properties of Ta_2O_5-doped SnO_2 ceramics. I have made several improvements compared to the previous study [170]:

I. Densification behavior and diffusion processes

In Ta-doped samples with lower CoO addition, the total dopant addition is too low to provide fast grain boundary diffusion and enhanced SnO_2 grain growth, whereas with higher addition of CoO (4 mol%), this condition appears to be satisfied. The resulting Ta/Co ratio inside SnO_2 grains is slightly below 2, indicating that the predominant mechanism of dopant incorporation into the SnO_2 grains follows a different charge compensation mechanism, described in chapter 4. A similar Ta/Co ratio was also measured at the grain boundaries, indicating that excess Ta does not accumulate at the grain boundaries, and thus does not hinder the diffusion processes, which in turn leads to better densification and increased relative densities of the samples.

II. Electric and dielectric characteristics

Balanced addition of acceptor and donor dopants strongly influences varistor and dielectric properties. In this chapter, dense SnO_2-based ceramics with a high relative density ($\rho_{rel} \sim$ 97 %), high nonlinear coefficient ($\alpha = 40$) and extremely low leakage current ($I_L = 1.2\ \mu A$) were obtained by the addition of 4 mol% CoO and 1 mol% Ta_2O_5. This sample showed promising properties for low-voltage varistors applications and indicated how important it is to add balanced addition of both dopants in order to improve varistor properties. For example, in the sample with the same addition of Ta_2O_5 and lower addition of CoO (1 mol%), as demonstrated in Chapter 3, nonlinear coefficient reached only a value 7 with

similar grain size distribution, threshold voltage and extremely high porosity (~33 %). The best dielectric properties with high dielectric constant and low dielectric losses ($\varepsilon = 6525$; $\tan \delta = 0.057$ at 1kHz) were obtained for the sample with the largest SnO_2 grains (with the addition of 4 mol% CoO and 0.10 mol% Ta_2O_5).

More on this topic is provided in the article entitled "'Microstructure development in (Co,Ta)-doped SnO_2-based ceramics with promising varistor and dielectric properties", written by S. Tominc, A. Rečnik, S. Bernik, M. Mazaj, M. Spreitzer and N. Daneu [173]. For this article, I performed sample preparation, solid-state sintering, XRD sample preparation, density measurements, polishing and thermal etching of the samples, SEM/TEM sample preparation, SEM/TEM observations, TEM/EDS analyses, average grain size determination, varistor (I-U) measurements and processing and interpretation of the obtained data together with the listed co-authors. The article is presented on page 57.

Journal of the European Ceramic Society 40 (2020) 5518–5522

Contents lists available at ScienceDirect

Journal of the European Ceramic Society

journal homepage: www.elsevier.com/locate/jeurceramsoc

Original article

Microstructure development in (Co,Ta)-doped SnO_2-based ceramics with promising varistor and dielectric properties

Sara Tominc[a,b,*], Aleksander Rečnik[a], Slavko Bernik[a], Matjaž Mazaj[c], Matjaž Spreitzer[d], Nina Daneu[d]

[a] Jožef Stefan Institute, Department for Nanostructured Materials, Jamova Cesta 39, Ljubljana, Slovenia
[b] Jožef Stefan International Postgraduate School, Jamova Cesta 39, Ljubljana, Slovenia
[c] National Institute of Chemistry, Department of Inorganic Chemistry and Technology, Hajdrihova 19, Ljubljana, Slovenia
[d] Jožef Stefan Institute, Advanced Materials Department, Jamova Cesta 39, Ljubljana, Slovenia

ARTICLE INFO

Keywords:
SnO_2 ceramic
Dopants
Microstructures
Varistors
Dielectric properties

ABSTRACT

Following the $3\,Sn(IV)_{Sn(IV)}^{x} \leftrightharpoons Co(II)_{Sn(IV)}^{'} + 2\,Ta(V)_{Sn(IV)}^{\cdot}$ charge compensation mechanism we optimized densification and electrical properties of Ta_2O_5-doped SnO_2–CoO ceramics. We show that incorporation of acceptor dopant Co^{2+} in SnO_2 is promoted after the addition of donor dopant like Ta^{5+}, whereas any surplus of Co would form secondary Co_2SnO_4 phase. A balanced addition of both dopants is needed to promote densification, and any surplus of donor dopants that remain present at the grain boundaries retard the grain growth and deteriorate electrical properties. Varistor and dielectric properties are then strongly influenced by donor doping. Optimum varistor properties (α = 40, U_T = 272 V/mm, I_L = 1.2 μA) were measured for the sample with 1 mol% Ta_2O_5 and the best dielectric properties (ε = 6525; tan(δ) = 0.057@1kHz) were measured for the sample with 0.10 mol% Ta_2O_5 with the largest SnO_2 grain sizes.

1. Introduction

Owing to favourable electrical properties and thermal stability, tin oxide (SnO_2)-based ceramics is gaining advantage among metal oxide semiconductors for varistor and dielectric applications [1]. Since the varistor properties of polycrystalline ceramics arise from the grain boundaries, a high fraction of active grain boundaries is crucial, and hence dense microstructures with minimized porosity are desired [2]. Despite its promising properties, the widespread use of SnO_2-based ceramics for varistor and dielectric applications is challenged by low intergranular diffusivity, leading to poor densification and porosity of microstructures [3–6].

In the last two decades, a vast number of reports addressed the influence of different dopants on sinterability and related electrical properties of SnO_2-based ceramics [7–20]. The addition of acceptor dopants, such as CoO, is essential to generate double Schottky barriers by accumulation of oxygen vacancies, $V_O^{\cdot\cdot}$, at the surface of SnO_2 grains; whereas donor dopants, such as Ta_2O_5 [8–17], Nb_2O_5 [11,18,19] and Sb_2O_3 [11,18,20] improve conductivity of SnO_2 grains by creating free electrons in the lattice. Through generation of $V_O^{\cdot\cdot}$ both grain boundary mobility and densification are improved, while the addition of donor dopants was reported to play a significant role in SnO_2 grain growth [8–14,18,19]. Therefore, a balanced addition of both donors and acceptors is required. Zang et.al. [21], showed that 0.1 mol% Co_2O_3 addition is not sufficient for densification of SnO_2 ceramics, while 1.2 mol % of Co_2O_3 significantly improved relative density of the sample, however the nonlinear coefficient reached a value of only ~13. Furthermore, Aguilar-Martinez et al. [22] showed that with higher addition of Co_3O_4 to SnO_2 the porosity decreased, with nonlinear coefficient ranging between 6–12.

In CoO–Ta_2O_5 doped SnO_2 ceramics, we have recently shown, that due to surface Sn^{2+} evaporation, Co^{2+} compensates the surplus charge of Ta^{5+} on Sn-sites according to the following compensation mechanism: $3\,Sn(IV)_{Sn(IV)}^{x} \leftrightharpoons Co(II)_{Sn(IV)}^{'} + 2\,Ta(V)_{Sn(IV)}^{\cdot}$ [17]. This essentially new charge compensation mechanism does not involve a divalent tin, compared to the Nb_2O_5-doped SnO_2-CoO system, where donors are also compensated by Sn^{2+}: $6\,Sn(IV)_{Sn(IV)}^{x} \leftrightharpoons Sn(II)_{Sn(IV)}^{'} + Co(II)_{Sn(IV)}^{'} + 4\,Nb(V)_{Sn(IV)}^{\cdot}$ [19]. Here, Co^{2+} is the only divalent cation that plays this role, and if the amount of Co^{2+} is too low, the surplus of Ta^{5+} segregates at the GBs and hinders the grain-boundary mobility [23].

In this work, we investigated Ta_2O_5- doped SnO_2-CoO system to improve sample densities by increasing CoO addition (4 mol%) and to increase the performance of this system, suitable for low voltage

* Corresponding author at: Department for Nanostructured Materials, Jožef Stefan Institute, Jamova cesta 39, 1000 Ljubljana, Slovenia.
E-mail address: sara.tominc@ijs.si (S. Tominc).

https://doi.org/10.1016/j.jeurceramsoc.2020.03.062
Received 11 December 2019; Received in revised form 21 March 2020; Accepted 27 March 2020
Available online 28 April 2020

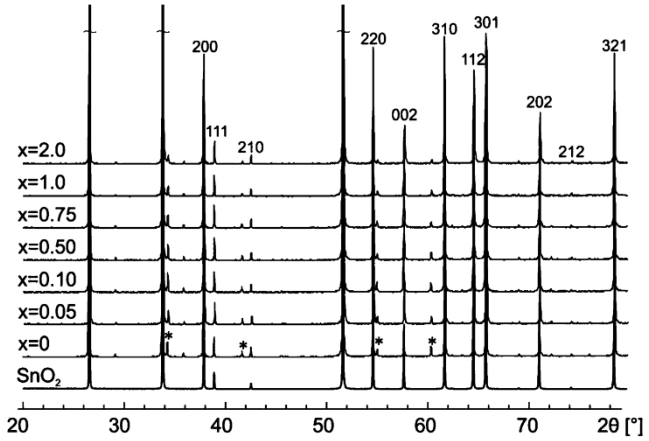

Fig. 1. X-ray diffraction patterns of SnO_2–4 mol% CoO–x Ta_2O_5 ceramics. Asterisk denotes reflections of Co_2SnO_4 appearing for compositions x = 0.0–2.0 mol% at 2θ ≈ 34.3°, 41.7°, 55.1° and 60.5°.

applications. With special attention on the charge compensation mechanisms from previous works [17,19], we have found optimal experimental conditions for the significantly improved varistor and dielectric properties of Ta_2O_5-doped SnO_2 ceramics.

2. Experimental procedure

We prepared Ta_2O_5-doped SnO_2 ceramics with different amounts of CoO (1,2,3 and 4 mol%) in order to find conditions of optimum densification. The highest density of the samples was obtained in the composition with 4 mol % of CoO for all additions of Ta_2O_5: (96-x) mol % SnO_2 + 4 mol% CoO + x mol% Ta_2O_5, where x = 0.05, 0.10, 0.50, 0.75, 1.0 and 2.0. The initial oxides used were SnO_2 (Alfa Aesar, 99.9 %, nanopowder), CoO (Alfa Aesar, 95 %) and Ta_2O_5 (Alfa Aesar, 99 %). Ceramic pellets were prepared according conventional solid-state process and sintered in tube furnace for 5 h at 1430 °C in air atmosphere.

Relative densities (ρ_{rel}) of the samples were measured using the Archimedes method. Phase composition was analysed by X-ray diffractometer (PANalytical X'Pert PRO MPD), using Cu-Kα_1 radiation in the range 2θ = 20–80° with a step of 0.034° and recording time of 100 s/step. X-ray diffraction data was quantified by Rietveld refinement (within Topas Academic v.6 software package) to determine the change of lattice parameters and to quantify the involved phases. The Rietveld refinement included modified structure by replacing Sn^{4+} sites by Ta^{5+} and Co^{2+} atoms in the 2:1 ratio, using their total molar contributions above 0.5 mol% Ta_2O_5, while for the samples with lower concentration of Ta_2O_5, due to insignificant contributions, the occupancies of the dopant atoms were not considered in the unit cell refinement procedure.

The microstructures were examined by field-emission gun scanning electron microscope (FEG-SEM; JSM-7600 F, Jeol Ltd., Tokyo, Japan). Chemical composition of SnO_2 grains and grain boundaries was studied in transmission electron microscope (TEM; JEM-2010 F, Jeol Ltd., Tokyo, Japan) equipped with energy dispersive spectrometer (EDS; Oxford Instruments ISIS 300).

For measurements of varistor and dielectric properties of the sample, silver electrodes were applied on the opposite sides of the sintered pellets and fired at 600 °C for 15 min. High-voltage source meter (Keithley 2410, Keithley Instruments Inc., Cleveland, USA) was used for *U-I* measurements. Bulk dielectric properties were measured using inductance/capacitance/resistance meter (LCR Model 4284A; Hewlett–Packard, USA) at frequencies from 20 Hz to 1 MHz at the room temperature.

3. Results and discussion

3.1. Densification and microstructure development

Fig. 1 shows phase compositions of the SnO_2–4 mol% CoO–x Ta_2O_5 ceramics samples sintered at 1430 °C for 5 h. The main reflections can be assigned to tetragonal SnO_2 (cassiterite; $P4_2/mnm$). In addition, weak reflections from spinel-type Co_2SnO_4 phase are observed as a result of the reaction 2 CoO + SnO_2 → Co_2SnO_4 [24]. The SnO_2 unit-cell parameters and fraction of the spinel phase in the samples with different additions of Ta_2O_5 were determined using Rietveld refinement (Table 1). The results show that unit cell parameters of the main SnO_2 phase remain practically constant due to balanced incorporation of Co^{2+} and Ta^{5+} into SnO_2 grains in dual co-doped samples. This is being the main reason for changing quantity of the secondary Co_2SnO_4 phase in the samples. The amount of Co_2SnO_4 phase mainly depends on the addition of CoO. In the samples with lower CoO addition of 1 mol%, the amount of secondary phase was around 0.2 mol% [17], whereas in this study, where a higher CoO addition of 4 mol% was used, the fraction of the Co_2SnO_4 phase in the sample reaches 1.3 mol% (without Ta_2O_5 addition), while with higher additions of Ta_2O_5, it drops to 0.9 mol % (sample with 2 mol% Ta_2O_5).

Table 1
Results of SnO_2 unit cell dimensions and quantification of SnO_2/Co_2SnO_4 phase content (mol %) for all compositions (96-x) mol% SnO_2 + 4 mol% CoO + x mol% Ta_2O_5 after Rietveld refinement.

Sample	Unit cell dimensions for SnO_2 (*P42/mnm* symmetry)			Phase content (mol %)	
	a(Å)	*c*(Å)	*V*(Å^3)	SnO_2	Co_2SnO_4
SnO_2	4.73963(5)	3.18804(4)	71.616(2)	100	–
4% CoO	4.73956(7)	3.18797(6)	71.613(2)	98.7(2)	1.3(2)
0.05 % Ta_2O_5	4.73963(3)	3.18809(5)	71.618(2)	98.9(1)	1.1(1)
0.1 % Ta_2O_5	4.73999(6)	3.18819(5)	71.630(2)	98.9(1)	1.1(1)
0.5 % Ta_2O_5	4.73995(6)	3.18742(6)	71.612(2)	98.9(1)	1.1(1)
0.75 % Ta_2O_5	4.73995(5)	3.18692(4)	71.601(2)	99.0(1)	1.0(1
1% Ta_2O_5	4.74015(5)	3.18611(4)	71.589(2)	99.0(2)	1.0(2)
2% Ta_2O_5	4.73954(9)	3.18361(7)	71.514(3)	99.1(3)	0.9(2)

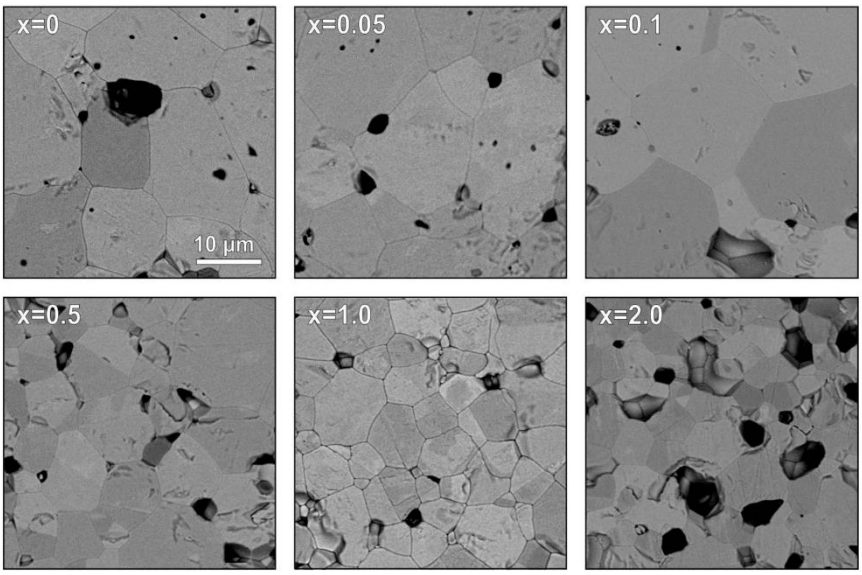

Fig. 2. SEM/BSE images of thermally etched cross-sections of SnO_2–4 mol% CoO ceramics with different Ta_2O_5 additions. **(a)** SnO_2 – 1 mol% CoO, with no Ta_2O_5 addition, **(b)** 0.05 mol% Ta_2O_5 addition, **(c)** 0.1 mol% Ta_2O_5 addition, **(d)** 0.5 mol% Ta_2O_5 addition, **(e)** 1.0 mol% Ta_2O_5 addition, and **(f)** 2.0 mol% Ta_2O_5 addition. With lower Ta_2O_5 additions **(b)** and **(c)**, coarse-grained microstructures are obtained, while with higher Ta_2O_5 additions **(d-f)**, microstructures are fine-grained. Compositions with 0.1 mol% **(c)** and 1.0 mol% Ta_2O_5 **(e)** are highly dense with only 3-4% of porosity.

The influence of CoO and Ta_2O_5 additions on the microstructure of SnO_2-based ceramics was further investigated by SEM. The main microstructural parameters including relative density and average grain size of the samples are listed in Table 2. Already a small addition of CoO (1 mol%) to SnO_2 significantly improves densification and SnO_2 grains size [17], while with the addition of 4 mol% CoO the average grain size increases 4-fold (16 µm) and has a characteristic coarse-grained microstructure (Fig. 2a). At the same time, the porosity is reduced from 10 % for SnO_2-1 mol% CoO composition [17], to only 5% in the SnO_2 - 4 mol% sample. SEM analysis has shown that pores are mostly located at triple points. Small additions of 0.05 and 0.10 mol% Ta_2O_5 to the SnO_2–4 mol% CoO composition have only a minor effect on the density and SnO_2 grain size, which increases to ~20 µm (Fig. 2c). This can be explained by incorporation of tantalum into SnO_2 grains, where as a result, tin self-diffusion is enhanced. With increasing additions of Ta_2O_5 (> 0.5 mol%) to given SnO_2-CoO composition, reduction of the grain

Table 3
Results of the EDS analyses for the SnO_2-4 mol% CoO-1 mol% Ta_2O_5 composition with the displayed ratio of dissolved Ta/Co (in at %) in SnO_2 grains and at the GB.

	Co-K [at%]	Ta-K [at%]	Ta/Co ratio
Grains	1.50	2.38	1.6
	1.28	1.96	1.5
	1.44	2.52	1.8
	1.10	2.02	1.8
	1.55	2.63	1.7
	1.20	2.17	1.8
	1.37	2.31	1.7
	1.73	2.95	1.71
GB	1.74	2.98	1.71

Table 2
Relative density ρ_{rel}, average grain size d, with basic varistor properties: threshold voltage U_T, non–linearity coefficient α, leakage current I_L and dielectric permittivity ε at fixed frequency 1 kHz with dielectric losses tan δ of the Ta_2O_5-doped SnO_2–CoO samples.

Sample	ρ_{rel}* [%]	d[µm]	U_T[V/mm]	α	I_L [µA]	ε	tanδ
SnO_2	55.7 ± 2.1	~0.1 – 1.0	n/a	n/a	n/a	n/a	n/a
SnO_2 + 4% CoO	95.1 ± 0.3	16.0 ± 5.6	126 ± 6	13	7.3	3312	0.059
+ 0.05 % Ta_2O_5	95.3 ± 0.1	17.3 ± 5.5	102 ± 9	12	16.5	5636	0.049
+ 0.10 % Ta_2O_5	96.2 ± 0.2	19.1 ± 5.0	77 ± 1	11	16.2	**6525**	0.057
+ 0.50 % Ta_2O_5	93.3 ± 0.2	9.8 ± 2.9	148 ± 2	12	16.3	3118	0.055
+ 0.75 % Ta_2O_5	92.5 ± 0.7	7.5 ± 2.0	210 ± 12	17	7.9	2276	0.071
+ 1.0 % Ta_2O_5	97.2 ± 0.2	6.3 ± 2.1	272 ± 2	**40**	1.2	1810	0.042
+ 2.0 % Ta_2O_5	88.5 ± 0.3	4.5 ± 1.4	10 ± 1	2	158	402	0.029

* theoretical density: ρ_{theor} = 6.95 g/cm.

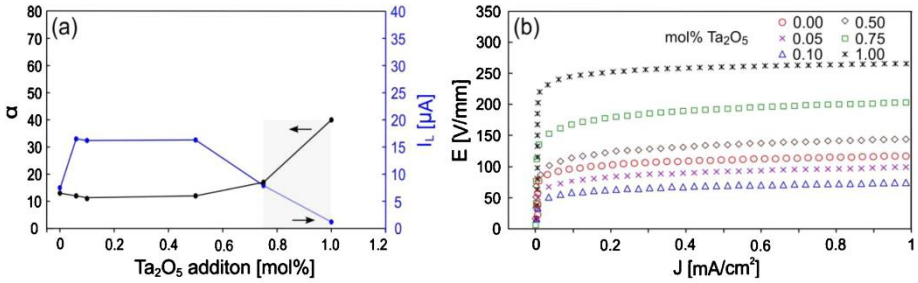

Fig. 3. (**a**) Nonlinear coefficient, α and leakage current, I_L of the SnO_2–4 mol% CoO samples doped with different amounts of Ta_2O_5 (x = 0.0–1.0 mol%). Sample with 1 mol% of Ta_2O_5 addition show the best nonlinear properties (shaded area). (**b**) Applied electric field, E, as a function of current density, J, of the SnO_2–4 mol% CoO–x mol% Ta_2O_5 samples.

sizes is observed. The sample with addition of 1 mol% Ta_2O_5 has the highest density (Fig. 2e), which can be explained only by optimal dopants ratio for balanced incorporation of both aliovalent dopants into SnO_2 grain. Similar to Nb_2O_5-doped SnO_2-CoO ceramics [19], higher additions of Ta_2O_5 (2 mol%) have an inhibiting effect on densification and SnO_2 grain growth (Fig. 2f).

In the Ta-doped samples with lower CoO addition (1 mol%), the total dopant addition is too low to ensure fast grain boundary diffusion processes and enhanced SnO_2 grain growth [17] and the ceramics does not reach the regime of good densification, however, on higher addition of CoO this condition is satisfied and at the same sintering temperature SnO_2 ceramics is fully dense.

EDS analyses of the samples were performed to study the local chemical composition of the grains and grain boundaries. In the samples with the addition of just CoO, the presence of Co inside SnO_2 grains was not detected [17,19]. Incorporation of acceptor dopant Co^{2+} into SnO_2 grains is triggered only after the addition of donor dopants like Nb^{5+} or Ta^{5+}, whereas any surplus of Co would form secondary Co_2SnO_4 phase, as shown by our XRD analysis.

In our previous work [17], EDS analyzes showed that above the 0.5 mol% Ta_2O_5 addition, the Ta/Co ratio in SnO_2 grains is constant 2:1. Based on these results, we verified the Ta/Co ratio in SnO_2 grains for the sample with sufficiently high dopant addition (1 mol% Ta_2O_5).The EDS results show that the resulting Ta/Co ratio inside SnO_2 grains is slightly below 2 (Table 3), indicating that the prevailing mechanism of dopant incorporation into the SnO_2 grains follows:$3\,Sn(IV)_{Sn(IV)}^{\times} \leftrightharpoons Co(II)_{Sn(IV)}^{''} + 2\,Ta(V)_{Sn(IV)}^{\cdot}$ charge compensation [17]. However, additional effects, including partial oxidation of CoO reactant to Co_3O_4, changing the molar ratio, and nonequilibrium distribution of dopants in SnO_2 grains, cannot be excluded. In addition, a similar Ta/Co ratio was also measured at the grains boundaries, indicating that excess Ta is not accumulating at the GBs, and thus it is not hindering the diffusion processes, which consequently leads to better densification and increased relative densities of the samples (Table 2).

3.2. Varistor and dielectric properties

While low amounts of CoO (1 mol%) in SnO_2 ceramics generate a measurable varistor effect with a threshold voltage U_T of 69 V/mm and nonlinearity coefficient α = 6 [19], higher addition of CoO (4 mol%) increases the nonlinear coefficient and threshold voltage by a factor of 2. With the addition of 0.05 – 0.5 mol% of donor dopant Ta_2O_5, varistor properties of SnO_2 ceramics remain similar as in the binary SnO_2-CoO system with the nonlinearity coefficient around 12. With 0.10 mol% of Ta_2O_5 addition, the lowest threshold voltage of 77 V/mm was measured due to coarse-grained microstructure (average grain size 19.1 ± 5.0 μm). With further increase of Ta_2O_5, the breakdown electric field increases [18,25]. Optimal varistor properties were achieved for 1 mol% of Ta_2O_5 addition. This composition displays high nonlinearity (α = 40), highest threshold voltage of 272 V/mm and low leakage current 1.2 μA (Fig. 3) due to low porosity and more uniform grain size distribution. For comparison, in porous SnO_2-1% CoO-1% Ta_2O_5 sample,

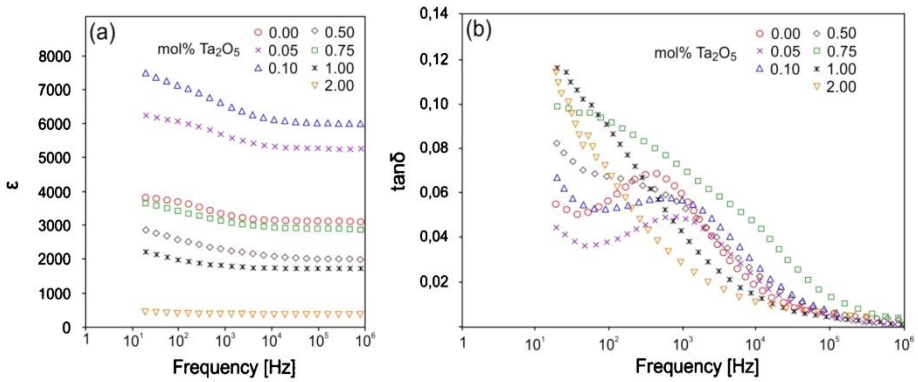

Fig. 4. (**a**) Frequency dependence of dielectric permittivity with different content of Ta_2O_5 dopant and 4% addition of CoO. (**b**) Dielectric loss tangent, tan δ, of all sintered SnO_2–4 mol% CoO–x mol% Ta_2O_5 samples.

the nonlinearity coefficient α reached only a value of 7 with similar threshold voltage and grain size distribution [17]. This indicates how important is to add acceptor and donor dopant not only in suitable ratio but also in absolute amounts in order to improve the varistor properties. In the sample with 2 mol% Ta_2O_5, the varistor properties are significantly deteriorate due to the high porosity and small grain size. Mean values of α, U_T and I_L are summarized in Table 2.

In addition to excellent varistor properties, the SnO_2 - 4% CoO ceramics doped with Ta_2O_5 displays also good dielectric characteristics. While the best varistor properties were measured for the sample with 1 mol% Ta_2O_5 (Ta/Co ratio of 2:1), the highest dielectric permittivity of 6525 in combination with low dielectric losses of 0.057 at 1 kHz were measured for the sample with low addition of 0.10 mol% Ta_2O_5, where the largest SnO_2 grain size (~20 μm) was observed (Fig. 4). With the increasing additions of Ta_2O_5, dielectric permittivity rapidly decreases to the value of undoped SnO_2 along with the reduction of the average grain size.

4. Conclusions

We have studied SnO_2 ceramics with the addition of 4 mol% CoO and varying additions of Ta_2O_5. SnO_2 with 4 mol% CoO is characterized by coarse-grained microstructure with average SnO_2 grain size of 16 microns. In binary compositions, Co mainly segregates to the grain boundaries and reacts with SnO_2 to form secondary Co_2SnO_4 spinel phase. Small additions (0.05 and 0.10 mol%) of Ta_2O_5 to the SnO_2 – 4 mol% CoO system enhance the densification and SnO_2 grain growth. In SnO_2 ceramics with 0.10 mol% Ta_2O_5 and the largest average grain size of around ~20 μm exhibits the best dielectric properties with dielectric permittivity of 6525 and low dielectric losses of 0.057 at 1 kHz. In the samples with higher additions of Ta_2O_5, the SnO_2 grain size decreases. The sample with the addition of 4 mol% CoO and 1 mol% Ta_2O_5 in the Ta/Co ratio of 2:1 has the highest density and shows the best varistor properties with nonlinearity coefficient ($\alpha = 40$), threshold voltage of 272 V/mm and low leakage current ($I_L = 1.2$ μA).

Declaration of Competing Interest

The authors declare that they have no known competing financial interests or personal relationships that could have appeared to influence the work reported in this paper.

Acknowledgements

The authors gratefully acknowledge David Fabjan for dielectric measurements (from the Advanced Materials Department, Jožef Stefan Institute). This work was supported by the Slovenian Research Agency under The Project No. J1-9177 and Z1-4202 and is based in part on the Ph.D. Thesis of S. Tominc under the contract No. 0106/37484.

References

[1] P.R. Bueno, J.A. Varela, E. Longo, Admittance and dielectric spectroscopy of polycrystalline semiconductors, J. Eur. Ceram. Soc. 27 (2007) 4313–4320.
[2] M.S. Mihaiu, O. Scarlat, S. Zuca, M. Zaharescu, C. Sikalidis (Ed.), Advanced SnO2-Based Ceramics: Synthesis, Structure, Properties, Advances in Ceramics- Synthesis and Characterization, Processing and Specific Applications, InTech, 2011, pp. 101–126.
[3] M. Nagasawa, S. Shionoya, S. Makishima, Vapor reaction growth of SnO_2 single crystals and their properties, J. Appl. Phys. 4/3 (1965) 195–202.
[4] C.L. Hoenig, A.W. Searcy, Knudsen and Langmuir evaporation studies of stannic oxide, J. Am. Ceram. Soc. 49 (1966) 128–134.
[5] J.A. Varela, O.J. Whittemore, E. Longo, Pore-size evolution during sintering of ceramic oxides, Ceram. Int. 16 (1990) 177–189.
[6] E.R. Leite, J.A. Cerri, E. Longo, J.A. Varela, C.A. Paskocima, Sintering of ultrafine undoped SnO_2 powder, J. Eur. Ceram. Soc. 21 (2001) 669–675.
[7] S.A. Pianaro, P.R. Bueno, P. Olivi, E. Longo, J.A. Varela, Effect of Bi_2O_3 addition on the microstructure and electrical properties of the SnO_2·CoO·Nb_2O_5 varistor system, J. Mat. Sci. Lett. 16 (1997) 634–638.
[8] A.C. Antunes, S.M. Antunes, S.A. Pianaro, E. Longo, J.A. Varela, Effect of Ta_2O_5 doping on the electrical properties of 0.99SnO_2·0.01CoO ceramic, J. Mat. Sci. 35 (2000) 1453–1458.
[9] A. Dibb, S.M. Tebcherani, W. Lacerda Jr, M. Cilense, J.A. Varela, E. Longo, Influence of the rare-earths oxides doped on the SnO_2CoOMn$O_2Ta_2O_5$ varistor system, J. Mat. Sci.: Mat. Electron. 13 (2002) 567–570.
[10] C.P. Li, J.F. Wang, W.B. Su, H.C. Chen, W.X. Wang, G.Z. Zang, L. Xu, Nonlinear electrical properties of SnO_2·Li_2O·Ta_2O_5 varistors, Ceram. Int. 28 (2002) 521–526.
[11] S.R. Dhage, V. Ravi, Influence of various donors on nonlinear I-V characteristics of tin dioxide ceramics, Appl. Phys. Lett. 83 (2003) 4539–4541.
[12] C. Wang, J. Wang, H. Chen, W. Su, G. Zang, P. Qi, M. Zhao, Effects of CuO on the grain size and electrical properties of Sno2- based varistors, Mat. Si. Eng: B 116 (2005) 54–58.
[13] F.M. Filho, A.Z. Simões, A. Ries, L. Perazolli, E. Longo, J.A. Varela, Nonlinear electrical behaviour of the Cr_2O_3, ZnO, CoO and Ta_2O_5-doped SnO_2 varistors, Ceram. Int. 32 (2006) 283–289.
[14] I.P. Silva, A.Z. Simões, F.M. Filho, E. Longo, J.A. Varela, L. Perazolli, Dependence of La_2O_3 content on the nonlinear electrical behaviour of ZnO, CoO and Ta_2O_5 doped SnO_2 varistors, Mat. Lett. 61 (2007) 2121–2125.
[15] J. He, Z. Peng, Z. Fu, C. Wang, X. Fu, Effect of ZnO doping on the microstructural and electrical properties of SnO_2-Ta_2O_5 based varistors, J. All. Comp. 528 (2012) 79–83.
[16] J. Zhang, L. Bian, W. Ren, L. Wang, J. Xu, Improvement in the non-linear electrical characteristics of the SnO_2 · Co_2O_3 · Ta_2O_5 varistor material with Pr_6O_{11} additive, Ceram. Int. 41 (2015) 9399–9402.
[17] S. Tominc, A. Rečnik, S. Bernik, N. Daneu, Charge compensation and electrical characteristics of Ta_2O_5–doped SnO_2–CoO ceramics, J. Eur. Ceram. Soc. 40/2 (2020) 355–361.
[18] A.N. Bondarchuk, A.B. Glot, A.R. Velasco-Rosales, Effects of Sb and Nb dopants on electrical and microstructural properties of low- voltage varistor ceramics based on SnO2, Ceram. Int. 44 (2018) 7844–7850.
[19] S. Tominc, A. Rečnik, Z. Samardžija, G. Dražić, M. Podlogar, S. Bernik, N. Daneu, Twinning and charge compensation in Nb_2O_5–doped SnO_2–CoO ceramics exhibiting promising varistor characteristics, Ceram. Int. 44 (2018) 1603–1613.
[20] M.B. Hernández, A. García-Villareal, R.F. Cienfuegos-Pelaes, C. Gómez-Rodríguez, J.A. Aguilar-Martínez, Structural, microstructure and electric properties of SnO_2-Sb_2O_5-Cr_2O_3 varistor ceramics doped with Co_2SnO_4 spinel phase previously synthesized, J. All. Comp. 699 (2017) 738–744.
[21] G.Z. Zang, J.F. Wang, H.C. Chen, W.B. Su, C.M. Wang, P.Qi, Effect of Co_2O_3 on the microstructure and electrical properties of Ta-doped SnO_2 varistors, J. Phys. D Appl. Phys. 38 (2005) 1072–1075.
[22] J.A. Aguilar-Martínez, P. Zambrano-Robledo, S. García-Villarreal, M.B. Hernández, E. Rodríguez, L.Falcon-Franco, Effect of high content of Co_3O_4 on the structure, morphology, and electrical properties of (Cr,Sb)-doped SnO_2 varistors, Ceram. Int. 42 (2016) 7576–7582.
[23] A.E. Montes Mejía, M.I. Pech-Canul, M.B. Hernández, S. García-Villarreal, C. Gómez Rodríguez, J.A. Aguilar-Martínez, Grain refinement and non–ohmic properties in (Co,Ta)–doped SnO_2 ceramics by Cr_2O_3 additions and the in situ formation of $CoCr_2O_4$, Appl. Phys. A 124 (2018) 474.
[24] J.A. Aguilar-Martínez, M.I. Pech-Canul, M. Esneider, A. Toxqui, S. Shaji, Synthesis, structure parameter and reaction pathway for spinel-type Co_2SnO_4, Mat. Lett. 78 (2012) 28–31.
[25] M.M. Shahraki, S. Alipour, P. Mahmoiudi, A. Karimi, Novel multifunctional capacitor-varistor ceramics based on SnO_2, Ceram. Int. 44 (2018) 20386–20390.

Chapter 6

Conclusions

In scientific literature, there is no study till now, where the mechanism of twinning in natural SnO_2 (cassiterite) has been explained. Also, no similar research has been done to explain twinning in synthesized SnO_2 formed with specific twin-forming dopants (such as Nb_2O_5, Ta_2O_5, ...). SnO_2 has an excellent combination of interesting properties such as high melting point, transparency, semi-conductivity, high thermal conductivity and wide band-gap, which allow its use in many applications, however there is no research on how the presence of twin affects final physical properties of SnO_2-based ceramics. Thus, in my doctoral dissertation, I aimed to show how the presence of twin boundaries can affect the electrical properties of SnO_2 materials used in diverse technological applications.

Through experimental work I was able to resolve the following:

- Ionic charge compensation mechanism for the SnO_2-CoO-Nb_2O_5 system is not the same as for SnO_2-CoO-Ta_2O_5 due to considerably lower solid solubility of Ta_2O_5 in SnO_2.
- Twin boundaries are not directly induced by the addition of donor dopant (chemically induced). The dopants are merely segregated to them.
- TBs in SnO_2 are formed in the nucleation stage and have a benign role in ceramic microstructure evolution.
- A balanced addition of acceptor and donor dopants is required to improve SnO_2 densification and to achieve optimum varistor properties.

SnO_2 ceramics were prepared using solid-state synthesis and conventional (pressureless) sintering. The first step was to achieve optimal conditions for dense SnO_2-based ceramics. The key processes to achieve this goal are sufficiently high sintering temperature, sintering time and a balanced addition of acceptor and donor dopants. In this part of my doctoral dissertation, I focused mainly on the study of point defects in SnO_2-based ceramics. Essential results that enabled me to resolve the charge compensation mechanisms were obtained by TEM/EDS analysis, where I showed that the amount of Co dissolved in SnO_2 grains is about 4-times lower than the amount of incorporated Nb, which corresponds to the ratio of Co^{2+} and Nb^{5+} to produce an equal amount of vacancies on O and Sn sites in SnO_2. In the case of Ta_2O_5 doping, the amount of dissolved Ta has been shown to be twice lower due to the lower solid solubility of Ta in SnO_2. Based on equilibria of point defects and well-known point defect compensation in SnO_2 ceramics, I proposed the most probable charge compensation mechanisms for both systems.

The purpose of the doctoral dissertation was to clarify the local atomic structure of planar defects (twin boundaries) and to understand their mechanism of formation in SnO_2. I was able to refute the fundamental hypothesis that the twinning in SnO_2 is chemically induced by the addition of donor dopants, similar to IBs in ZnO. An important result of this study is the evidence of complex {101} twinning, using TEM and EBSD analysis.

While many of these twins were typical contact twins, the majority are multiple, mainly cyclic twins. Using atomic-scale HAADF-STEM, I showed that the donor dopants are segregated to the vicinity of the twin plane and are not strictly localized to it. Even though, at first glance, the effect of donor dopants in SnO_2-based ceramics appears similar to the effect of IB-forming dopants in ZnO-based ceramics, I confirmed by additional analyses that the proportion of twinned grains in SnO_2-based ceramics never exceeds 50% of the microstructure, and furthermore, no anisotropic grain growth is observed along the TBs, as this is otherwise typical of IBs in ZnO. All this proof suggests that TBs are formed by nucleation on a yet unknown precursor in the initial stages of grain growth and are likely the result of a yet unexplained sequence of topotaxial replacement reactions, similar to that in isostructural rutile (TiO_2). The exact formation mechanism remains unclear and further studies at the atomic level with emphasis on nucleation of the precursor phase will be required.

I also investigated the effect of twin boundaries on microstructure development and electrical properties of SnO_2-based ceramics and concluded that the fraction of twinned grains depends on the amount of added donor dopant. With equimolar addition of acceptor (CoO) and donor (Nb_2O_5 or Ta_2O_5) dopant, the microstructure is tightly packed with SnO_2 grains, where multiple and cyclic twins are common. Finally, the studied SnO_2 materials were optimized for their electrical and dielectric properties for use in varistor applications. I have shown that a small addition of donor dopant (Nb_2O_5 or Ta_2O_5) causes about 3 times larger average grain size and most grains here are single, untwinned crystallites. Accordingly, the increase in the average grain size led to a higher dielectric permittivity, while the electrical properties were still weak. The nonlinear behavior of varistor ceramics was further increased by additional donor doping (up to 1 mol%) until the optimal varistor properties and thus the highest nonlinear coefficients were achieved. Higher addition of donor additives ($>$ 1 mol%) drastically reduced the grain size, increased the porosity and caused a collapse of nonlinearity.

Through my doctoral work, I have shown how important it is to add acceptor and donor dopant not only in the appropriate ratio, but also in absolute amounts, to improve varistor properties. Through my analysis, I have shown that SnO_2-based ceramics have excellent varistor properties comparable to commercial ZnO-based varistors, as well as good dielectric characteristics important for use in microelectronics applications. I confirmed that donor dopants enhance the formation of twin boundaries, but do not cause their formation. Thus, based on the current results, I can conclude that the formation of SnO_2 twins is triggered by nucleation on an unknown precursor phase. By determining the exact mechanism of twinning, I could control the formation of TBs in SnO_2 ceramics and consequently also the grain size and development of microstructures.

Appendix A

Twinning and Charge Compensation in Nb_2O_5–Doped SnO_2–CoO Ceramics Exhibiting Promising Varistor Characteristics

Data presented in this chapter supplement the article introduced in Chapter 3.

A.1 Article`s Supporting Information

Solid state synthesis method

For the synthesis, I used the solid-state method, commonly used for ceramic materials preparation. I weighed the calculated values of the starting input oxides (SnO_2, CoO, and Nb_2O_5) at specific molar ratios (*see* Table A1 and Figure A1 a). The powder mixture was homogenized in an agate mortar with the addition of absolute ethanol and dried at room temperature (Figure A1 b). The homogenization process was repeated three times. The powder mixture (0.5 g) was then pressed into pellets at a pressure of 150 MPa. The pellets were 8 mm in diameter and 3 mm thick (Figure A1 c, d). The pellets were fired in a tube furnace (Fig. A1 e), according to the temperature regime shown in Fig. A2. The samples were heated to temperature 1430 °C with a heating rate 5 °C/min then isothermally sintered at this temperature for 5 hours and slowly cooled to room temperature with a cooling rate 5 °C/min.

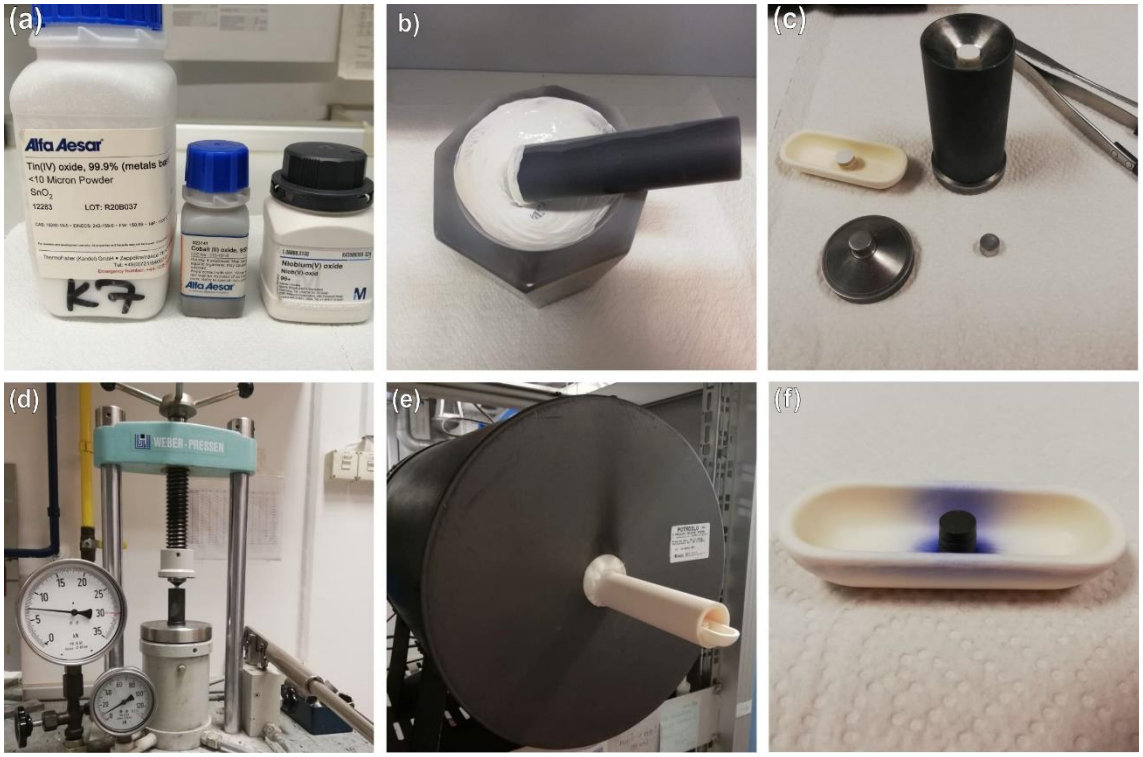

Figure A1: Conventional sintering of ceramic materials.

Table A1: Molar ratios of input oxides for the synthesis of SnO_2-based ceramics

SnO_2 (mol%)	**CoO (mol%)**	**Nb_2O_5 (mol%)**
100	0	0
99.0	1.0	0
98.9	1.0	0.1
98.5	1.0	0.5
98.25	1.0	0.75
98.0	1.0	1.0
97.0	1.0	2.0

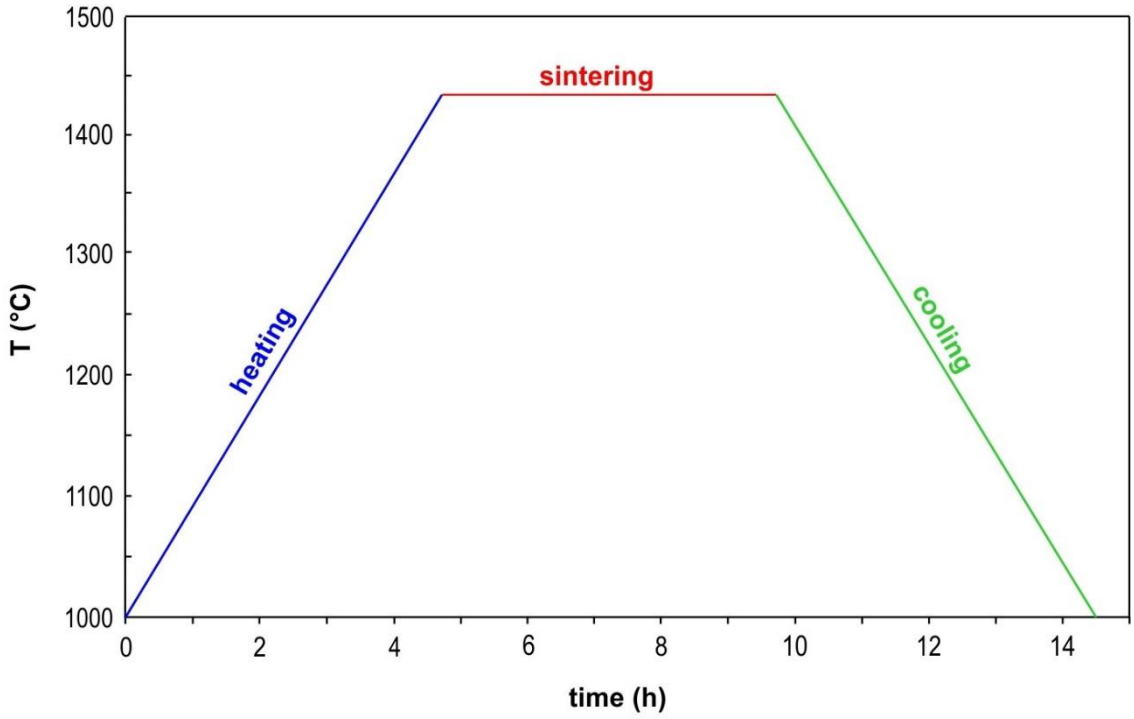

Figure A2: Temperature sintering regime for sintering SnO_2-based ceramics.

Densification behavior

To determine the maximum densification rate value of SnO_2-1 mol% CoO and SnO_2- 1 mol% CoO- 1 mol% Nb_2O_5 compositions, we plotted the linear shrinkage rate $d((L_0 - L_1)/L_0)/dT$, which was calculated from the data presented in Figure 1 in the article, with respect to the sintering temperature. It is observed that the maximum densification rate for the sample doped with CoO only is at T_{max}= 1315 °C, while additional doping with Nb shifts the curve to T_{max}= 1430 °C.

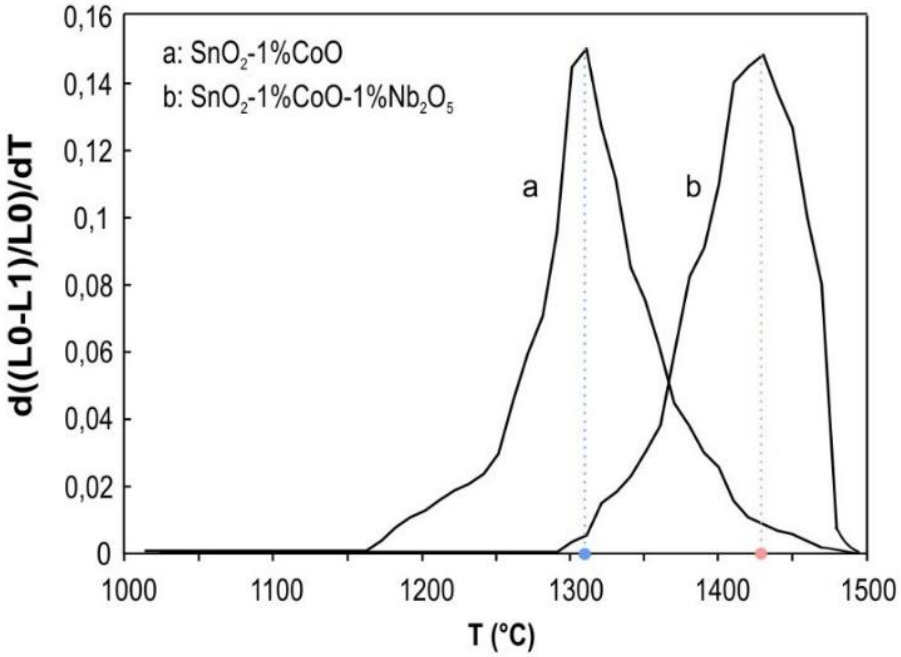

Figure A3: Linear shrinkage rate as a function of temperature (T) for **(a)** SnO_2-1 mol% CoO and **(b)** SnO_2-1 mol% CoO- 1 mol% Nb_2O_5.

Sample preparation for EBSD study

For the EBSD study, the samples were sintered for 5 hours in an air atmosphere at 1430 °C and cooled down slowly with 5 °C/min. The cross-sections of the samples were mechanically ground and polished down to 3 µm with a final polishing step using a colloidal silica of 0.05 µm grade to obtain smooth, fine sample surface. Samples were thermally etched at 1280 °C for 5 minutes to prevent the formation of an amorphous layer.

EBSD study of SnO_2 twins

To obtain information about crystallographic orientation of SnO_2 grains, 3231 Kikuchi patterns were recorded within the EBSD area analysis (Figure A3). Further analysis of local misorientations across the grain boundaries between neighboring grains confirmed the presence of elbow twins, where the angle between the [100] directions on the two twin individuals is 67.8° [107].

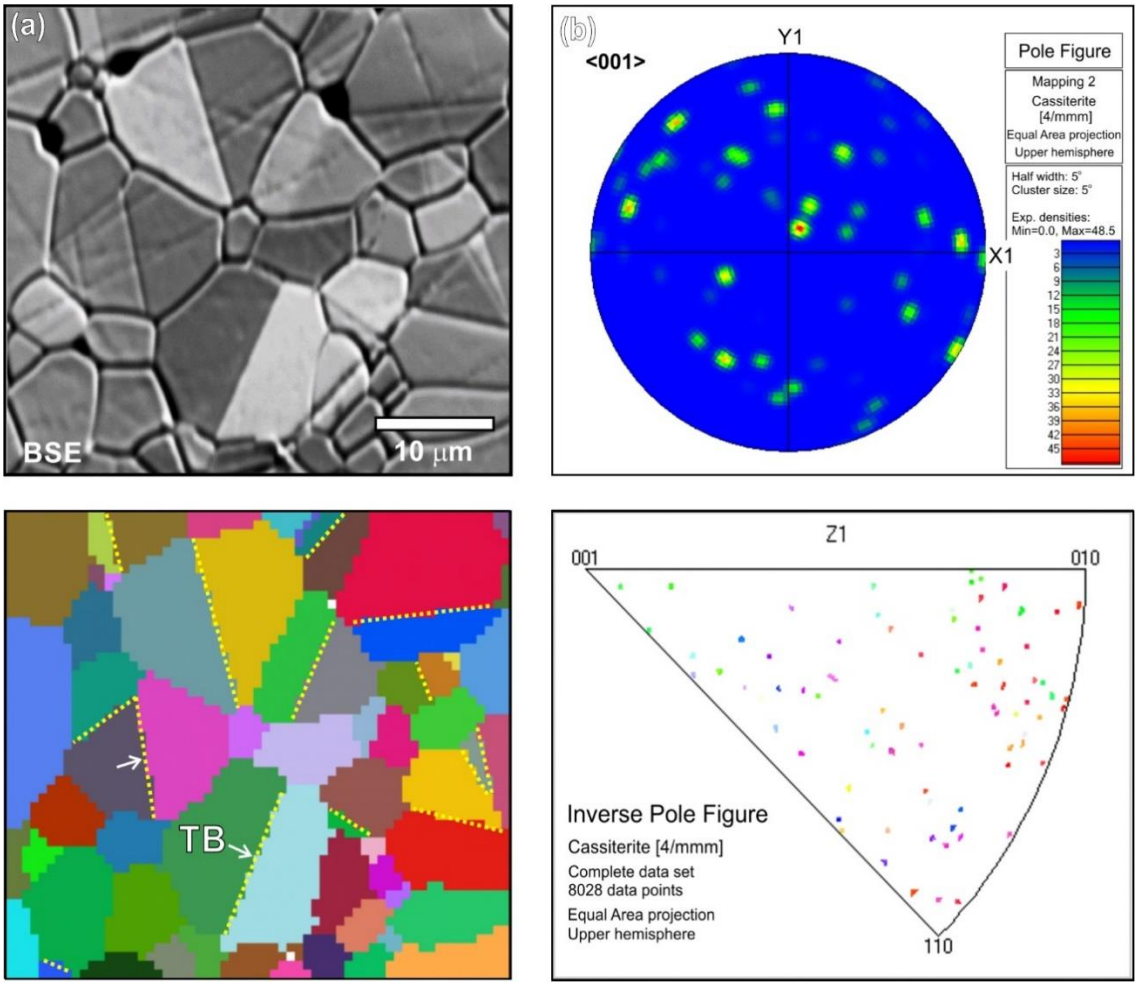

Figure A4: EBSD area analysis about grain orientation in SnO_2-1 mol% CoO-1 mol% Nb_2O_5 ceramics. **(a)** EBSD map of the selected area. Yellow lines indicate TBs, where the grains are met in {101} twin orientation. **(b)** The inverse pole figure diagram revealed random spatial distribution of the crystallographic orientations of SnO_2 grains.

The following Table A2 and Figure A5 provide additional information about the dielectric properties of Nb_2O_5-doped SnO_2–CoO samples, which are not included in the article.

Characterization method and calculations of the dielectric permittivity and dielectric losses

For DC current-voltage (I-U) characterization and dielectric measurements, silver paste electrodes were painted on both sides of the sintered pellets and fired at 600 °C for 15 min. Varistor properties of the samples were measured using high-voltage source meter (Keithley 2410, Keithley Instruments Inc., Cleveland, USA). To determine the threshold voltage U_T (V/mm) and the non-linear coefficient (α) we measured nominal varistors voltages U_N (V) at current densities $J_1 = 1$ mA/cm^2 and $J_2 = 10$ mA/cm^2, leakage currents I_L (μA) at 0.75 U_N (1 mA/cm^2) and sample thickness d (mm). The threshold voltage was calculated by the equation [75]:

$$U_T = \frac{U_N}{d} \tag{S1}$$

and coefficient of nonlinearity by the equation:

$$\alpha = \frac{d\ logJ}{d \log U} \tag{S2}$$

Dielectric measurements were performed using an inductance/capacitance/resistance (LCR) meter (Model 4284A; Hewlett–Packard, USA) at frequencies from 20 Hz to 1 MHz at room temperature. Dielectric permittivity (ε) was calculated by the equation:

$$\varepsilon = \frac{C\ d}{A\ \varepsilon_0} \tag{S3}$$

where C is the capacitance, d is the thickness of the sample, A is the surface of the sample and $\varepsilon_0 = 8.854 \cdot 10^{-12}$ F/m is the vacuum permittivity. The dielectric loss is described as tan δ, where δ represents the phase angle between the signal of the sample and the signal, expected for an ideal lossless capacitor.

To examine the relation between the grain size and the electrical characteristics of ceramics, we measured the impedance at room temperature and at a fixed frequency of 1 kHz for the samples with different Nb_2O_5 additions. The obtained results reflect in a 2-fold increase of the dielectric permittivity (ε) from 2675 for the SnO_2–CoO sample to 5131 with the lowest addition of Nb_2O_5 (x=0.1). On the other hand, dielectric loss reduced from 0.085 (SnO_2-CoO sample) to 0.040 at a frequency of 1 kHz. With further additions of Nb_2O_5 (x > 0.1), dielectric permittivity decreases, while a fine-grained ceramic (x = 2.0) shows a higher dielectric loss (*see* Table A1) [174].

Table A2: Dielectric permittivity ε at a fixed frequency 1 kHz with dielectric losses tan δ of the Nb_2O_5-doped SnO_2–CoO samples.

Sample	**ε**	**tan δ**
SnO_2 + 1% CoO	2675	0.085
… + 0.1% Nb_2O_5	5131	0.040
… + 0.5 % Nb_2O_5	2869	0.034
… + 0.75 % Nb_2O_5	2559	0.023
… + 1.0 % Nb_2O_5	888	0.061
… + 2.0 % Nb_2O_5	1092	0.289

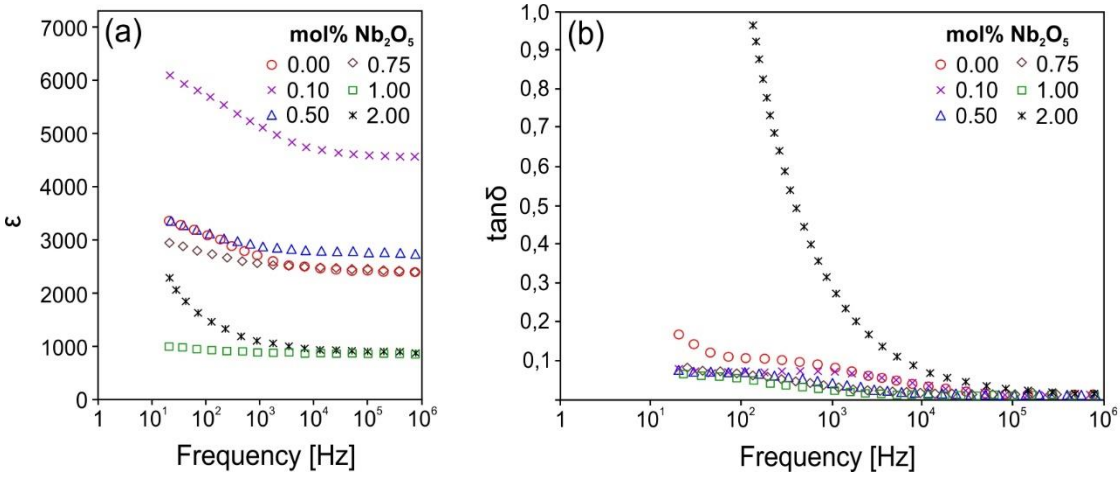

Figure A5: (a) Dielectric permittivity versus frequency with a different content of the Nb_2O_5 dopant. (b) Dielectric loss vs. frequency for SnO_2–1 mol% CoO–x mol% Nb_2O_5 samples.

Appendix B

Charge Compensation and Electrical Characteristics of Ta_2O_5-Doped SnO_2-CoO Ceramics

Data presented in this Chapter supplement the article introduced in Chapter 3.

B.1 Article`s Supporting Information

To improve the densification of the samples and to avoid sintering at high temperatures, I prepared the sample with the most porous composition SnO_2 - 1 mol% CoO - 1 mol% Ta_2O_5 by spark plasma sintering (SPS). For the SPS experiment, 0.75 g of powder was placed in a cylindrical graphite mold with an inner diameter of 10 mm and spark-plasma processed (Dr. Sinter, Fuji Electronic Industrial Co. Ltd) under vacuum (~20 Pa) and with 80 MPa of uniaxial applied pressure. The temperature, measured using a K-type thermocouple inserted into the graphite die close to the sample, was 900 °C with a heating rate approximately 100 °C/min and the time spent at the desired temperature (holding time) was 5 min. For SEM observations, the samples were thermally etched at 1280 °C for 15 minutes.

With SPS I can reach a significantly better densification (~ 90 %) compared to conventional sintering (CS), where the achieved relative density is about 66 %. The reason for better densification of SnO_2 ceramics with SPS is a fast heating rate (~ 100 °C/min), which provides a fast start of densification (GB diffusion) together with non-densification processes (surface diffusion and evaporation-condensation at the GB). However, even if fast densification for SnO_2-based ceramics is achieved by SPS, ceramics microstructure is not uniform due to the decomposition and partial evaporation of SnO_2 leading to structural and compositional inhomogeneities [6], as seen in Figure B2. Due to the high heating rate, low sintering temperature and short annealing time, a metastable compound $Sn_2Ta_2O_7$ is formed as the secondary phase by the SPS processing [118], while with CS, no secondary phases are observed. In addition, as a result of SPS processing, carbon is detected in my ceramic samples due to the use of graphite cell.

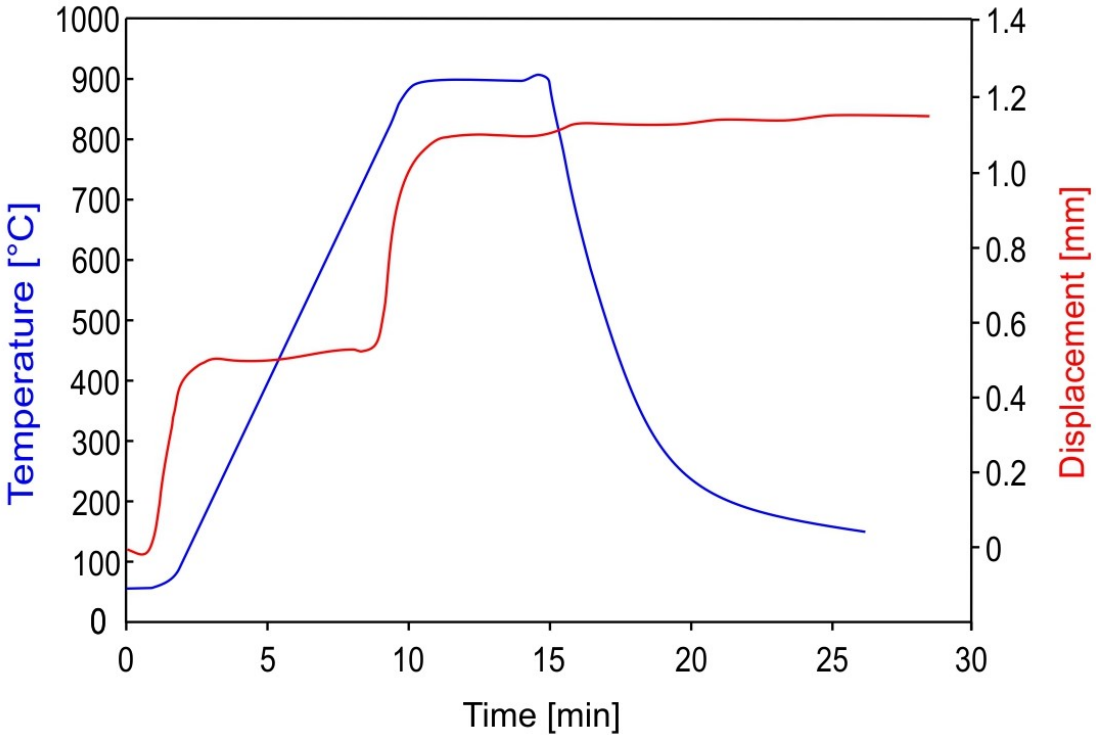

Figure B1: Sintering behavior of (Co,Ta)-doped SnO_2: temperature (*see* the blue curve) and displacement (*see* the red curve) as a function of sintering time.

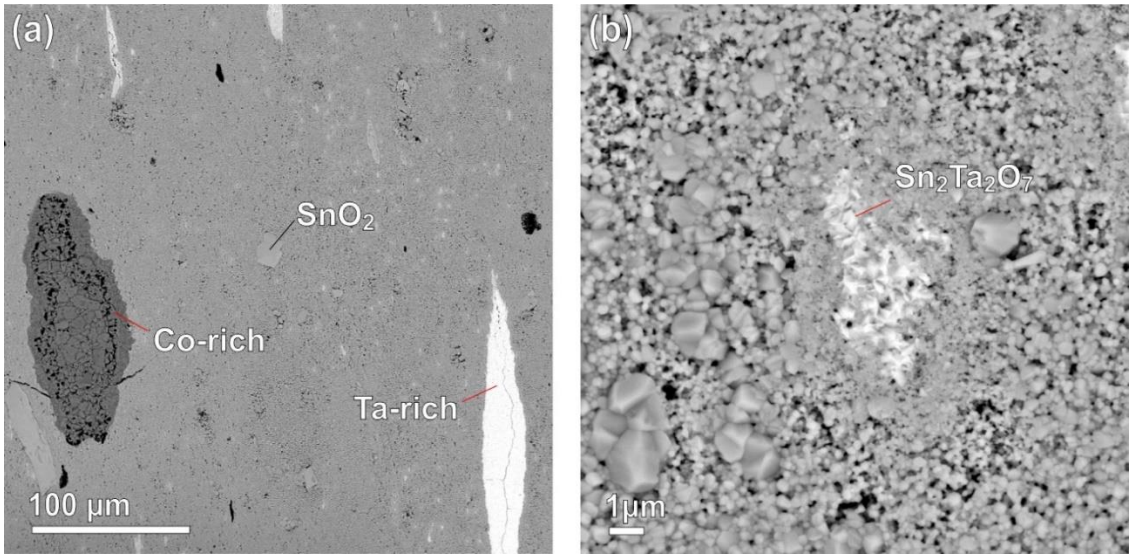

Figure B2: SEM images of thermally etched cross-sections of the SnO_2-1 mol% CoO-1 mol% Ta_2O_5 composition after SPS sintering at 900 °C/5 min: **(a)** Highly dense ceramics is obtained by SPS, however the uniformity of ceramics is structural inhomogeneous (marked by red lines). (b) Unlike CS, a metastable compound $Sn_2Ta_2O_7$ is produced by the SPS.

References

[1] W. Göpel and K. D. Schierbaum, "SnO_2 sensors: current status and future prospects," *Sens. Actuators B: Chem.*, vol. 26, no. 1–3. pp. 1–12, 1995.

[2] J. Q. Hu *et al.*, "Large-scale rapid oxidation synthesis of SnO_2 nanoribbons," *J. Phys. Chem. B*, vol. 106, no. 15, pp. 3823–3826, 2002.

[3] Y. Suda, H. Kawasaki, J. Namba, K. Iwatsuji, K. Doi, and K. Wada, "Properties of palladium doped tin oxide thin films for gas sensors grown by PLD method combined with sputtering process," *Surf. Coatings Technol.*, vol. 174–175, no. 03, pp. 1293–1296, 2003.

[4] V. Juttukonda *et al.*, "Facile synthesis of tin oxide nanoparticles stabilized by dendritic polymers," *J. Am. Chem. Soc.*, vol. 128, no. 2, pp. 420–421, 2006.

[5] S. Das and V. Jayaraman, "SnO_2: A comprehensive review on structures and gas sensors," *Prog. Mater. Sci.*, vol. 66, pp. 112–255, 2014.

[6] Y. Idota, T. Kubota, and A. Matsufuji, "Tin-Based Amorphous Oxide : A High-Capacity Lithium-lon-Storage Material," *Science*, vol. 276, no. 5317, pp. 1395–1397, 1997.

[7] Y. Zhang, Y. Liu, and M. Liu, "Nanostructured columnar tin oxide thin film electrode for lithium ion batteries," *Chem. Mater.*, vol. 18, no. 19, pp. 4643–4646, 2006.

[8] J. S. Chen and X. W. Lou, "SnO_2-based nanomaterials: Synthesis and application in lithium-ion batteries," *Small*, vol. 9, no. 11, pp. 1877–1893, 2013.

[9] U. Betz, M. Kharrazi Olsson, J. Marthy, M. F. Escolá, and F. Atamny, "Thin films engineering of indium tin oxide: Large area flat panel displays application," *Surf. Coatings Technol.*, vol. 200, no. 20–21, pp. 5751–5759, 2006.

[10] Z. Banyamin, P. Kelly, G. West, and J. Boardman, "Electrical and Optical Properties of Fluorine Doped Tin Oxide Thin Films Prepared by Magnetron Sputtering," *Coatings*, vol. 4, no. 4, pp. 732–746, 2014.

[11] K. Sekizawa, H. Widjaja, S. Maeda, Y. Ozawa, and K. Eguchi, "Low temperature oxidation of methane over Pd/SnO_2 catalyst," *Appl. Catal. A Gen.*, vol. 200, no. 1, pp. 211–217, 2000.

[12] Y. Fu, H. Ma, Z. Wang, W. Zhu, T. Wu, and G. J. Wang, "Characterization and reactivity of SnO_2-doped V_2O_5/γ-Al_2O_3 catalysts in dehydrogenation of isobutane to isobutene," *J. Mol. Catal. A Chem.*, vol. 221, no. 1–2, pp. 163–168, 2004.

[13] F. Lan, X. Wang, X. Xu, R. Zhang, and N. Zhang, "Preparation and characterization of SnO_2 catalysts for CO and CH_4 oxidation," *React. Kinet. Mech. Catal.*, vol. 106, no. 1, pp. 113–125, 2012.

[14] C. S. Maheswari, C. Shanmugapriya, K. Revathy, and A. Lalitha, "SnO_2

nanoparticles as an efficient heterogeneous catalyst for the synthesis of 2H-indazolo[2,1-b]phthalazine-triones," *J. Nanostructure Chem.*, vol. 7, no. 3, pp. 283–291, 2017.

[15] Y. Fukai, Y. Kondo, S. Mori, and E. Suzuki, "Highly efficient dye-sensitized SnO_2 solar cells having sufficient electron diffusion length," *Electrochem. commun.*, vol. 9, no. 7, pp. 1439–1443, 2007.

[16] J. Qian *et al.*, "TiO_2-coated multilayered SnO_2 hollow microspheres for dye-sensitized solar cells," *Adv. Mater.*, vol. 21, no. 36, pp. 3663–3667, 2009.

[17] H. J. Snaith and C. Ducati, "SnO_2-Based dye-sensitized hybrid solar cells exhibiting near unity absorbed photon-to-electron conversion efficiency," *Nano Lett.*, vol. 10, no. 4, pp. 1259–1265, 2010.

[18] B. Roose *et al.*, "Mesoporous SnO_2 electron selective contact enables UV-stable perovskite solar cells," *Nano Energy*, vol. 30, pp. 517–522, 2016.

[19] Q. Jiang, X. Zhang, and J. You, "SnO_2: A Wonderful Electron Transport Layer for Perovskite Solar Cells," *Small*, vol. 14, no. 31, pp. 1–14, 2018.

[20] S. A. Pianaro, P. R. Bueno, E. Longo, and J. A. Varela, "A new SnO_2-based varistor system," *J. Mater. Sci. Lett.*, vol. 14, no. 10, pp. 692–694, 1995.

[21] A. C. Antunes *et al.*, "Nonlinear electrical behaviour of the $SnO_2{\cdot}CoO \cdot Ta_2O_5$ system," *J. Mater. Sci. Lett.*, vol. 17, pp. 577–579, 1998.

[22] E. R. Leite *et al.*, "The infuence of sintering process and atmosphere on the non-ohmic properties of SnO_2 based varistor," *J. Mater. Sci. Mater. Electron*, vol. 10, pp. 1764–1769, 1999.

[23] J. Fayat and M. S. Castro, "Defect profile and microstructural development in SnO_2-based varistors," *J. Eur. Ceram. Soc.*, vol. 23, no. 10, pp. 1585–1591, 2003.

[24] M. M. Oliveira, J. C. Soares, P. R. Bueno, E. R. Leite, E. Longo, and J. A. Varela, "Grain-boundary segregation and precipitates in La_2O_3 and Pr_2O_3 doped $SnO_2 \cdot$ CoO-based varistors," *J. Eur. Ceram. Soc.*, vol. 23, no. 11, pp. 1875–1880, 2003.

[25] F. M. Filho *et al.*, "Investigation of electrical properties of tantalum doped SnO_2 varistor system," *Ceram. Int.*, vol. 31, no. 3, pp. 399–404, 2005.

[26] J. F. Wang, H. C. Chen, W. Bin Su, G. Z. Zang, B. Wang, and R. W. Gao, "Effects of Sr on the microstructure and electrical properties of (Co, Ta)-doped SnO_2 varistors," *J. Alloys Compd.*, vol. 413, no. 1–2, pp. 35–39, 2006.

[27] H. Bastami and E. Taheri-Nassaj, "Effect of Sm_2O_3 on the microstructure and electrical properties of SnO_2-based varistors," *Ceram. Int.*, vol. 38, no. 1, pp. 265–270, 2012.

[28] A. N. Bondarchuk, A. B. Glot, and A. R. Velasco-Rosales, "Effects of Sb and Nb dopants on electrical and microstructural properties of low-voltage varistor ceramics based on SnO_2," *Ceram. Int.*, vol. 44, no. 7, pp. 7844–7850, 2018.

[29] M. Batzill and U. Diebold, "The surface and materials science of tin oxide," *Prog. Surf. Sci.*, vol. 79, no. 2–4, pp. 47–154, 2005.

[30] H. Cachet, "Films and powders of fluorine-doped tin dioxide," in *Florinated Materials for Energy Conversion*, 2005, pp. 513–534.

[31] Y. C. Ji, H. X. Zhang, X. H. Zhang, and Z. Q. Li, "Structures, optical properties, and electrical transport processes of SnO2 films with oxygen deficiencies," *Phys.*

Status Solidi (B): Basic Res., 2013. .

[32] B. A. D. Williamson *et al.*, "Resonant Ta Doping for Enhanced Mobility in Transparent Conducting SnO_2," *Chem. Mater.*, vol. 32, no. 5, pp. 1964–1973, 2020.

[33] H. T. Tung, T. P. Nguyen, P. D. Huu, and T. Le, "Optical, electrical, and structural properties of Ta-doped SnO_2 films against substrate temperature using direct current magnetron sputtering," *Surf. Interfaces*, vol. 23, p. 100943, 2021.

[34] M. Nagasawa, S. Shionoya, and S. Makishima, "Vapor Reaction Growth of SnO_2 Single Crystals and Their Properties," *Jpn. J. Appl. Phys.*, vol. 4, no. 3, pp. 195–202, 1965.

[35] C. L. Hoenig and A. W. Searchy, "Knudsen and Langmuir Evaporation Studies of Stannic Oxide," *J. Am. Ceram. Soc.*, vol. 49, no. 3, pp. 128–134, 1966.

[36] J. A. Varela, O. J. Whittemore, and E. Longo, "Pore Size Evolution during Sintering of Ceramic Oxides," *Ceram. Int.*, vol. 16, pp. 177–189, 1990.

[37] E. R. Leite, J. A. Cerri, E. Longo, J. A. Varela, and C. A. Paskocima, "Sintering of ultrafine undoped SnO_2 powder," vol. 21, pp. 669–675, 2001.

[38] E. Medvedovski, "Tin oxide-based ceramics of high density obtained by pressureless sintering," *Ceram. Int.*, vol. 43, pp. 8396–8405, 2017.

[39] S. A. Pianaro, P. R. Bueno, and P. et. al. Olivi, "Electrical properties of the SnO_2-based varistor," *J. Mater. Sci. Mater. Electron.*, vol. 9, pp. 159–165, 1998.

[40] P. R. Bueno, S. A. Pianaro, E. C. Pereira, L. O. S. Bulhões, E. Longo, and J. A. Varela, "Investigation of the electrical properties of SnO_2 varistor system using impedance spectroscopy Investigation of the electrical properties of SnO_2 varistor system using impedance spectroscopy," *J. Appl. Phys.*, vol. 84, no. 7, pp. 3700–3705, 1998.

[41] G. Brankovic, Z. Brankovic, M. R. Davolos, M. Cilense, and J. A. Varela, "Influence of the common varistor dopants (CoO, Cr_2O_3 and Nb_2O_5) on the structural properties of SnO_2 ceramics," *Mater. Char.*, vol. 52, no. 4–5, pp. 243–251, 2004.

[42] I. P. Silva, A. Z. Simões, F. M. Filho, E. Longo, J. A. Varela, and L. Perazolli, "Dependence of La_2O_3 content on the nonlinear electrical behaviour of ZnO, CoO and Ta_2O_5 doped SnO_2 varistors," *Mat. Lett.*, vol. 61, no. 10, pp. 2121–2125, 2007.

[43] F. M. Filho *et al.*, "Influence of Ta_2O_5 on the electrical properties of ZnO- and CoO-doped SnO_2 varistors," *Ceram. Int.*, vol. 30, no. 8, pp. 2277–2281, 2004.

[44] D. G. Chang, J. H. Lee, and J. J. Kim, "Grain Growth Kinetics of Cobalt-Doped SnO_2 by Varying Nb_2O_5 Content," *Mater. Sci. Forum*, vol. 534–536, pp. 529–532, 2007.

[45] P. R. Bueno, M. O. Orlandi, L. G. P. Simões, E. R. Leite, E. Longo, and J. A. Cerri, "Nonohmic behavior of SnO_2-MnO polycrystalline ceramics. I. Correlations between microstructural morphology and nonohmic features," *J. Appl. Phys.*, vol. 96, no. 5, pp. 2693–2700, 2004.

[46] F. Kawamura, M. Kamei, I. Yasui, and I. Sunagawa, "Effect of Impurity Cations on the Growth and Habits of SnO_2 Crystals in the SnO_2-Cu_2O Flux System," *J. Am. Ceram. Soc.*, vol. 82, no. 3, pp. 774–776, 1999.

[47] F. Kawamura, I. Yasui, M. Kamei, and I. Sunagawa, "Habit Modifications of SnO_2 Crystals in SnO_2-Cu_2O Flux System in the Presence of Trivalent Impurity Cations,"

J. Am. Ceram. Soc., vol. 84, no. 6, pp. 1341–1346, 2001.

[48] V. V. Tomaev and A. I. Glazov, "Morphology of polycrystalline cassiterite films," *Crystallogr. Reports*, vol. 59, no. 5, pp. 749–752, 2014.

[49] S. Zhang, "Study of fluorine-doped tin oxide (FTO) thin films for photovoltaics applications," Technische Universität (Darmstadt, Allemagne), 2018.

[50] H. M. King, "Cassiterite - Mineral Properties - Used as an Ore of Tin," 2020. [Online]. Available: https://geology.com/minerals/cassiterite.shtml. [Accessed: 01-Feb-2021].

[51] H. Giefers, F. Porsch, and G. Wortmann, "Thermal disproportionation of SnO under high pressure," vol. 176, pp. 1327–1332, 2005.

[52] I. Erdem, H. H. Kart, and T. Cagin, "First principles studies of SnO at different structures," *Arch. Mater. Sci. Eng.*, vol. 45, no. 2, pp. 108–113, 2010.

[53] H. Li *et al.*, "Direct Imaging of the Passivating Film and Microstructure of Nanometer − Scale SnO Anodes in Lithium Rechargeable Batteries," *Electrochem. Solid-State Lett.*, vol. 1, no. 6, pp. 241–243, 1998.

[54] J. et. al. Chouvin, "Lithium intercalation in tin oxide," *J. Power Sources*, vol. 81–82, pp. 277–281, 1999.

[55] Z. Han, N. Guo, F. Li, W. Zhang, H. Zhao, and Y. Qian, "Solvothermal preparation and morphological evolution of stannous oxide powders," *Mater. Lett.*, vol. 48, no. 2, pp. 99–103, 2001.

[56] "Romarchite: Mineral information, data and localities." [Online]. Available: https://www.mindat.org/min-254.html. [Accessed: 29-Jan-2021].

[57] R. A. Ramik, R. M. Organ, and J. A. Mandarino, "On type romarchite and hydroromarchite from Boundary Falls, Ontario, and notes on other occurrences," *Can. Mineral.*, vol. 41, no. 3, pp. 649–657, 2003.

[58] "Cassiterite: Mineral information, data and localities." [Online]. Available: https://www.mindat.org/min-955.html. [Accessed: 25-Jan-2021].

[59] E. C. P. E. Rodrigues and P. Olivi, "Preparation and characterization of Sb-doped SnO_2 films with controlled stoichiometry from polymeric precursors," *J. Phys. Chem. Solids*, vol. 64, no. 7, pp. 1105–1112, 2003.

[60] R. Al-Gaashani, S. Radiman, N. Tabet, and A. R. Daud, "Optical properties of SnO_2 nanostructures prepared via one-step thermal decomposition of tin (II) chloride dihydrate," *Mater. Sci. Eng. B Solid-State Mater. Adv. Technol.*, vol. 177, no. 6, pp. 462–470, 2012.

[61] L. M. Fang *et al.*, "Microstructure and luminescence properties of Co-doped SnO_2 nanoparticles synthesized by hydrothermal method," *J. Mater. Sci. Mater. Electron.*, vol. 19, pp. 868–874, 2008.

[62] M. Krishna and S. Komarneni, "Conventional- vs microwave-hydrothermal synthesis of tin oxide, SnO_2 nanoparticles," *Ceram. Int.*, vol. 35, pp. 3375–3379, 2009.

[63] T. B. Nguyen, T. T. B. Le, and N. L. Nguyen, "The preparation of SnO_2 and SnO_2: Sb nanopowders by a hydrothermal method," *Adv. Nat. Sci. Nanosci. Nanotechnol.*, vol. 1, pp. 1–5, 2010.

[64] N. Talebian and F. Jafarinezhad, "Morphology-controlled synthesis of SnO_2

nanostructures using hydrothermal method and their photocatalytic applications," *Ceram. Int.*, vol. 39, pp. 8311–8317, 2013.

[65] S. Wang *et al.*, "One-pot synthesis of 3D hierarchical SnO_2 nanostructures and their application for gas sensor," *Sens. Actuators B: Chem.*, vol. 207, pp. 83–89, 2015.

[66] J. Zhang and L. Gao, "Synthesis and characterization of nanocrystalline tin oxide by sol-gel method," *J. Solid State Chem.*, vol. 177, pp. 1425–1430, 2004.

[67] M. Aziz, S. Saber Abbas, and W. R. Wan Baharom, "Size-controlled synthesis of SnO_2 nanoparticles by sol-gel method," *Mater. Lett.*, vol. 91, pp. 31–34, 2013.

[68] H. Köse, Ş. Karaal, A. O. Aydin, and H. Akbulut, "Structural properties of size-controlled SnO_2 nanopowders produced by sol-gel method," *Mater. Sci. Semicond. Process.*, vol. 38, pp. 404–412, 2015.

[69] T. Kimura, S. Inada, and T. Yamaguchi, "Microstructure development in SnO_2 with and without additives," *J. Mater. Sci.*, vol. 24, pp. 220–226, 1989.

[70] F. Bueno, P. R., de Cassia-Santos, M.R., Leite, E.R., Longo, E., Bisquert, J., Garcia-Belmonte, G., and Fabregat-Santiago, "Nature of the Schottky-type barrier of highly dense SnO_2 systems displaying nonohmic behavior," *J. Appl. Phys.*, vol. 88, pp. 6545–6548, 2000.

[71] M. R. C. Santos, P. R. Bueno, E. Longo, and J. A. Varela, "Effect of oxidizing and reducing atmospheres on the electrical properties of dense SnO_2-based varistors," *J. Eur. Ceram. Soc.*, vol. 21, no. 2, pp. 161–167, 2001.

[72] Z. Lu, Z. Chen, and J. Wu, "SnO_2-based varistors capable of withstanding surge current," *J. Ceram. Soc. Japan*, vol. 117, no. 7, pp. 851–855, 2009.

[73] A. B. Glot, R. Bulpett, A. I. Ivon, and P. M. Gallegos-Acevedo, "Electrical properties of SnO_2 ceramics for low voltage varistors," *Phys. B Condens. Matter*, vol. 457, pp. 108–112, 2015.

[74] M. Maleki Shahraki, M. A. Bahrevar, S. M. S. Mirghafourian, and A. B. Glot, "Novel SnO_2 ceramic surge absorbers for low voltage applications," *Mater. Lett.*, vol. 145, pp. 355–358, 2015.

[75] S. Tominc *et al.*, "Twinning and charge compensation in Nb_2O_5–doped SnO_2–CoO ceramics exhibiting promising varistor characteristics," *Ceram. Int.*, vol. 44, pp. 1603–1613, 2018.

[76] Y. Chiang, D. P. Birnie, and W. D. Kingery, *Physical ceramics: Principles for Ceramic Science and Engineering*. John Wiley & Sons, Inc, 1997, pp. 165-182.

[77] C. Wagner and W. Schottky, "Theorie der geordneten Mischphasen," *J. Phys. Chem. B*, vol. 11, pp. 163–210, 1930.

[78] P. Kofstad and T. Norby, "Chapter 1: Bonding, structure, and defects," in *Defects and Transport in Crystalline Solids*, University of Oslo, 2009, pp. 1–40.

[79] R. E. Smallman and R. J. Bishop, "Chapter 4: Defects in solids," in *Modern Physical Metallurgy and Materials Engineering: Science, process, applications*, Sixth Edit., Reed Educational and Prefessional Publishing Ltd., Ed. 1999, pp. 84–125.

[80] F. A. Kröger and H. J. Vink, "Relations between the Concentrations of Imperfections in Crystalline Solids," *Solid State Phys. - Adv. Res. Appl.*, vol. 3, no. C, pp. 307–435, 1956.

[81] L. Zhigilei, "MSE 6020: Defects and Microstructure in Materials," *University of*

Virginia.[Online].Available:
http://people.virginia.edu/~lz2n/mse6020/notes/Ionic.pdf.[Accessed: 22-Dec-2020].

[82] A. Kar and A. Patra, "Recent development of core-shell SnO_2 nanostructures and their potential applications," *J. Mater. Chem. C*, vol. 33, no. 2, pp. 6706–6722, 2014.

[83] M. Weidner, "Fermi Level Determination in Tin Oxide by Photoelectron Spectroscopy," TU Darmstadt, 2016.

[84] M. E. Cherns, D., Hawkridge, "The structure and properties of dislocations in GaN," *J. Mater. Sci.*, vol. 41, pp. 2685–2690, 2006.

[85] Y. Ohno *et al.*, "Optical properties of dislocations in wurtzite ZnO single crystals introduced at elevated temperatures," *J. Appl. Phys.*, vol. 104, no. 7, pp. 073515-1–6, 2008.

[86] H. Iwanaga, M. Egashira, K. Suzuki, M. Ichihara, and S. Takeuchi, "Twins and dislocations in SnO_2 whiskers," *Philos. Mag. A Phys. Condens. Matter, Struct. Defects Mech. Prop.*, vol. 58, no. 4, pp. 683–690, 1988.

[87] J. G. Zheng, X. Pan, M. Schweizer, U. Weimar, W. Göpel, and M. Rühle, "Growth twins in nanocrystalline SnO_2 thin films by high-resolution transmission electron microscopy," *J. Appl. Phys.*, vol. 79, no. 10, pp. 7688–7694, 1996.

[88] W. J. Tseng, P. Shen, and S. Y. Chen, "Defect generation of rutile-type SnO_2 nanocondensates: Imperfect oriented attachment and phase transformation," *J. Solid State Chem.*, vol. 179, no. 4, pp. 1237–1246, 2006.

[89] W. J. Tseng, P. Shen, and S. Y. Chen, "Fabrication and transformation of dense SnO_2 via laser ablation condensation," *J. Phys. Chem. Solids*, vol. 70, no. 2, pp. 334–339, 2009.

[90] K. Suzuki, M. Ichihara, and S. Takeuchi, "High-resolution electron microscopy of lattice defects in TiO_2 and SnO_2," *Philos. Mag. A Phys. Condens. Matter, Struct. Defects Mech. Prop.*, vol. 63, no. 4, pp. 657–665, 1991.

[91] D. B. Williams, C. B. Carter, D. B. Williams, and C. B. Carter, "Planar Defects," in *Transmission Electron Microscopy*, 1996, pp. 379–399.

[92] M. Ohring, "Chapter 8: Epitaxy," in *Materials Science of Thin Films,* Second Edit., 2002, pp. 417–494.

[93] A. Rečnik, N. Daneu, T. Walther, and W. Mader, "Structure and Chemistry of Basal-Plane Inversion Boundaries in Antimony Oxide-Doped Zinc Oxide," *J. Am. Ceram. Soc.*, vol. 84, no. 11, pp. 2657–2668, 2001.

[94] A. Rečnik, M. Eh, and D. Kolar, "Polytype induced exaggerated grain growth in ceramics," *J. Eur. Ceram. Soc.*, vol. 21, no. 10–11, pp. 2117–2121, 2001.

[95] A. Rečnik, S. Bernik, and N. Daneu, "Microstructural engineering of ZnO-based varistor ceramics," *J. Mater. Sci.*, vol. 47, no. 4, pp. 1655–1668, 2012.

[96] N. Daneu and A. Recnik, "The atomic-scale aspects of twinning and polytypism in minerals," *Acta Mineral.*, vol. 7, no. April 2012, pp. 32–37, 2012.

[97] Y. Takeuchi, *Tropochemicalcell-twinning: A structure-building mechanism in crystalline solids.* Terra Scientific Publishing Company, 1997.

[98] N. Daneu, A. Rečnik, and W. Mader, "Atomic structure and formation mechanism of (101) rutile twins from Diamantina (Brazil)," *Am. Mineral.*, vol. 99, no. 4, pp. 612–624, 2014.

[99] N. Daneu, A. Rečnik, and H. Schmid, "Atomic structure and formation mechanism of (301) rutile twins from Diamantina (Brazil)," *Am. Mineral.*, vol. 92, pp. 1789–1799, 2007.

[100] V. Jordan, U. Javornik, J. Plavec, A. Podgornik, and A. Rečnik, "Self-assembly of multilevel branched rutile-type TiO_2 structures via oriented lateral and twin attachment," *Sci. Rep.*, pp. 1–13, 2016.

[101] D. Makovec, D. Kolar, and M. Trontelj, "Sintering and microstructural development of metal oxide varistor ceramics," *Mat. Res. Bull.*, vol. 28, pp. 803–811, 1993.

[102] D. Makovec and M. Trontelj, "Extended Defects in ZnO Ceramics Containing $Bi_4Ti_3O_{12}$ Additive," *J. Am. Ceram. Soc.*, vol. 77, no. 5, pp. 1202–1208, 1994.

[103] N. Daneu, A. Rečnik, S. Bernik, and D. Kolar, "Microstructural development in SnO_2-doped ZnO-Bi_2O_3 ceramics," *J. Am. Ceram. Soc.*, vol. 83, no. 12, pp. 3165–3171, 2000.

[104] S. Bernik and N. Daneu, "Characteristics of SnO_2-doped ZnO-based varistor ceramics," *J. Eur. Ceram. Soc.*, vol. 21, no. 10–11, pp. 1879–1882, 2001.

[105] S. Bernik, J. Bernard, N. Daneu, and A. Rečnik, "Microstructure development in low-antimony oxide-doped zinc oxide ceramics," *J. Am. Ceram. Soc.*, vol. 90, no. 10, pp. 3239–3247, 2007.

[106] N. Daneu, S. Bernik, and A. Renik, "Inversion boundary induced grain growth in ZnO ceramics: From atomic-scale investigations to microstructural engineering," *J. Phys. Conf. Ser.*, vol. 326, no. 1–16, 2011.

[107] M. Nespolo and B. Souvignier, "Structural rationale for the occurrence of the elbow twins in cassiterite and rutile," *J. Miner. Pet. Sci.*, vol. 110, no. 4, pp. 157–165, 2015.

[108] D. Kolar, *Tehnična keramika*. Zavod Republike Slovenije za šolstvo in šport, Ljubljana, 1993.

[109] M. S. M. Ghazali and et. al., "Chapter 4: Conventional Sintering Effects on the Microstructure and Electrical Characteristics of Low-Voltage Ceramic Varistor," in *Sintering Techology-Method and Application*, IntechOpen, 2018, pp. 65–83.

[110] A. Dibb, S. M. Tebcherani, W. Lacerda, M. Cilense, and J. A. Varela, "Influence of the rare-earths oxides doped on the $SnO_2CoOMnO_2Ta_2O_5$ varistor system," *J. Mater. Sci. Mater. Electron.*, vol. 13, pp. 567–570, 2002.

[111] C. Wang *et al.*, "Effects of Ta_2O_5 on the grain size and electrical properties of SnO_2-based varistors," *J. Phys. D Appl. Phys.*, vol. 36, no. 23, pp. 3069–3072, 2003.

[112] Z. Branković, G. Branković, S. Bernik, and M. Žunić, "ZnO varistors with reduced amount of additives prepared by direct mixing of constituent phases," *J. Eur. Ceram. Soc.*, vol. 27, pp. 1101–1104, 2007.

[113] F. Chen, X. Li, J. Wu, Q. Shen, J. M. Schoenung, and L. Zhang, "Effect of post-annealing on the electrical conductivity of spark plasma sintered antimony-doped tin oxide (ATO) ceramics," *Scr. Mater.*, vol. 68, pp. 297–300, 2013.

[114] H. Beltrán, M. Prades, N. Masõ, E. Cordoncillo, and A. R. West, "Enhanced conductivity and nonlinear voltage-current characteristics of nonstoichiometric $BaTiO_3$ ceramics," *J. Am. Ceram. Soc.*, vol. 94, no. 9, pp. 2951–2962, 2011.

[115] W. G. Fahrenholtz, "Ceramic Engineering 111 Sintering," 2004. [Online]. Available:

web.mst.edu/~billf/labrpt.pdf. [Accessed: 27-Aug-2019].

[116] B. Henriques, D. Soares, J. C. Teixeira, and F. S. Silva, "Effect of hot pressing variables on the microstructure, relative density and hardness of sterling silver (Ag-Cu alloy) powder compacts," *Mater. Res.*, vol. 17, no. 3, pp. 664–671, 2014.

[117] Q. Li, D. Zhnang, G. Luo, C. Li, Q. Shen, and L. Zhang, "Spark plasma sintering of undoped SnO_2 ceramics," *J. Wuhan Univ. Technol. Mater. Sci. Ed.*, vol. 26, pp. 315–318, 2011.

[118] H. Yoshida, K. Morita, B. N. Kim, and K. Soga, "Low temperature spark plasma sintering of tin oxide doped with tantalum oxide," *J. Ceram. Soc. Japan*, vol. 124, no. 9, pp. 932–937, 2016.

[119] K. Rubenis, S. Populoh, P. Thiel, S. Yoon, U. Müller, and J. Locs, "Thermoelectric properties of dense Sb-doped SnO_2 ceramics," *J. Alloys Compd.*, vol. 692, pp. 515–521, 2017.

[120] J. L. Shi, "Solid state sintering of ceramics: Pore microstructure models, densification equations and applications," *J. Mater. Sci.*, vol. 34, pp. 3801–3812, 1999.

[121] R. M. German, "Sintering. Encyclopedia of Materials: Science and Technology," 2001, pp. 8641–8643.

[122] J. Lalande, R. Ollitrault-Fichet, and P. Boch, "Sintering behaviour of CuO-doped SnO_2," *J. Eur. Ceram. Soc.*, vol. 20, pp. 2415–2420, 2000.

[123] J. A. Cerri *et al.*, "Effect of cobalt(II) oxide and manganese (IV) oxide on sintering of tin (IV) oxide," *J. Am. Ceram. Soc.*, vol. 79, no. 3, pp. 799–804, 1996.

[124] S. R. Dhage and V. Ravi, "Influence of various donors on nonlinear I–V characteristics of tin dioxide ceramics," *Appl. Phys. Lett.*, vol. 83, no. 22, pp. 4539–4541, 2003.

[125] C. M. Wang, J. F. Wang, W. Bin Su, H. C. Chen, G. Z. Zang, and P. Qi, "Microstructure development and nonlinear electrical characteristics of the $SnO_2 \cdot CuO \cdot Ta_2O_5$ based varistors," *J. Mater. Sci.*, vol. 40, no. 24, pp. 6459–6462, 2005.

[126] T. S. Zhang, L. B. Kong, X. C. Song, Z. H. Du, W. Q. Xu, and S. Li, "Densification behaviour and sintering mechanisms of Cu- or Co-doped SnO_2: A comparative study," *Acta Mater.*, vol. 62, no. 1, pp. 81–88, 2014.

[127] A. E. Montes Mejía, M. I. Pech-Canul, M. B. Hernández, S. García-Villarreal, C. G. Rodríguez, and J. A. Aguilar-Martínez, "Grain refinement and non-ohmic properties in (Co, Ta)-doped SnO_2 ceramics by Cr_2O_3 additions and the in situ formation of $CoCr_2O_4$," *Appl. Phys. A Mater. Sci. Process.*, vol. 124, no. 7, pp. 1–9, 2018.

[128] C. M. Wang *et al.*, "Effects of CuO on the grain size and electrical properties of SnO_2-based varistors," *Mater. Sci. Eng. B Solid-State Mater. Adv. Technol.*, vol. 116, no. 1, pp. 54–58, 2005.

[129] T. K. Gupta, "Application of Zinc Oxide Varistors," *J. Am. Ceram. Soc.*, vol. 73, no. 7, pp. 1817–1840, 1990.

[130] D. R. Clarke, "Varistor Ceramics," *J. Am. Ceram. Soc. Ceram. Soc.*, vol. 82, no. 3, pp. 485–502, 1999.

[131] M. Matsuoka, "Nonohmic Properties of Zinc Oxide Ceramics," *Jpn. J. Appl. Phys.*, vol. 10, no. 6, pp. 736–746, 1971.

[132] E. R. Leite, M. A. L. Nobre, E. Longo, and J. A. Varela, "Microstructural development of ZnO varistor during reactive liquid phase sintering," *J. Mater. Sci.*, vol. 31, pp. 5391–5398, 1996.

[133] K. Kang *et al.*, "Nonlinear Property of (Nb_2O_5, $SrCO_3$, Ge, GeO_2)-Codoped TiO_2-Based Varistor Ceramics," *J. Am. Ceram. Soc.*, vol. 99, no. 1, pp. 158–166, 2016.

[134] N. Wang, J. Li, J. Ning, and J. Liu, "Effect of Mn, Si on varistor-dielectric characteristics of Nb-doped $SrTiO_3$ ceramics," *Appl. Mech. Mater.*, vol. 239–240, pp. 1604–1608, 2013.

[135] V. V. Deshpande, M. M. Patil, and V. Ravi, "Low voltage varistors based on CeO_2," *Ceram. Int.*, vol. 32, no. 1, pp. 85–87, 2006.

[136] X. Dong, Y. Gan, Y. Wang, S. Peng, and L. Dong, "Effect of La_2O_3 on high-temperature thermoelectric properties of WO_3," *J. Alloy. Compd.*, vol. 581, pp. 52–55, 2013.

[137] G. Z. Zang *et al.*, "New $ZnSnO_3$-based varistor system," *J. Mater. Sci.*, vol. 39, no. 10, pp. 3537–3539, 2004.

[138] J. Zhang, L. Bian, W. Ren, L. Wang, and J. Xu, "Improvement in the non-linear electrical characteristics of the $SnO_2 \cdot Co_2O_3 \cdot Ta_2O_5$ varistor material with Pr_6O_{11} additive," *Ceram. Int.*, vol. 41, no. 8, pp. 9399–9402, 2015.

[139] P. R. Bueno, E. R. Leite, M. M. Oliveira, M. O. Orlandi, and E. Longo, "Role of oxygen at the grain boundary of metal oxide varistors: A potential barrier formation mechanism," *Appl. Phys. Lett.*, vol. 79, no. 1, pp. 48–50, 2001.

[140] A. Tao, M., Bui, Ai, Dorlanne, O., and Loubiere, "Different 'single grain junctions' within a ZnO varistor," *J. Appl. Phys.*, vol. 61, pp. 1562–1567, 1987.

[141] Y. M. Chiang, W. D. Kingery, and L. M. Levinson, "Compositional changes adjacent to grain boundaries during electrical degradation of a ZnO varistor," *J. Appl. Phys.*, vol. 53, pp. 1765–1768, 1982.

[142] D. Zhou, C. Zhang, and S. Gong, "Degradation phenomena due to dc bias in low-voltage ZnO varistors," *Mater. Sci. Eng. B*, vol. 99, pp. 412–415, 2003.

[143] M. B. Hernández, S. García-Villarreal, R. F. Cienfuegos-Pelaes, C. Gómez-Rodríguez, and J. A. Aguilar-Martínez, "Structural, microstructure and electric properties of SnO_2-Sb_2O_5-Cr_2O_3 varistor ceramics doped with Co_2SnO_4 spinel phase previously synthesized," *J. Alloy. Compd.*, vol. 699, pp. 738–744, 2017.

[144] C. Xu, J. Tamaki, N. Miura, and N. Yamazoe, "Grain size effects on gas sensitivity of porous SnO2-based elements," *Sens. Actuators B*, vol. 3, no. 2, pp. 147–155, 1991.

[145] P. R. Bueno, J. A. Varela, and E. Longo, "SnO_2, ZnO and related polycrystalline compound semiconductors: An overview and review on the voltage-dependent resistance (non-ohmic) feature," *J. Eur. Ceram. Soc.*, vol. 28, no. 3, pp. 505–529, 2008.

[146] M. Egashira, Y. Shimizu, Y. Takao, and Y. Fukuyama, "Hydrogen-sensitive breakdown voltage in the I-V characteristics of tin dioxide-based semiconductors," *Sensors Actuators B*, vol. 33, pp. 89–95, 1996.

[147] M. Egashira, Y. Shimizu, Y. Takao, and S. Sako, "Variations in I-V characteristics

of oxide semiconductors induced by oxidizing gases," *Sens. Actuators B: Chem.*, vol. 35, no. 1–3, pp. 62–67, 1996.

[148] R. Metz, D. Koumeir, J. Morel, J. Pansiot, M. Houabes, and M. Hassanzadeh, "Electrical barriers formation at the grain boundaries of Co-doped SnO_2 varistor ceramics," *J. Eur. Ceram. Soc.*, vol. 28, no. 4, pp. 829–835, 2008.

[149] A. L. W. Buonocore *et al.*, "Varistor behavior in a ternary system based on SnO_2 doped with a hexavalent donor: SnO_2-MnO_2-WO_3," *J. Alloy. Compd.*, vol. 811, pp. 1–12, 2019.

[150] C. M. Wang, J. F. Wang, W. Bin Su, G. Z. Zang, and P. Qi, "Effects of Ta_2O_5 on the electrical properties of $SnO_2 \cdot CuO$ ceramics," *J. Phys. D Appl. Phys.*, vol. 38, no. 9, pp. 1485–1488, 2005.

[151] C. R. Foschini, L. Perazolli, and J. A. Varela, "Sintering of tin oxide using zinc oxide as a densification aid," *J. Mater. Sci.*, vol. 39, no. 18, pp. 5825–5830, 2004.

[152] G. Zhang and M. Liu, "Effect of particle size and dopant on properties of SnO_2-based gas sensors," *Sens. Actuators B: Chem.*, vol. 69, no. 1, pp. 144–152, 2000.

[153] I. Saadeddin *et al.*, "Simultaneous doping of Zn and Sb in SnO_2 ceramics: Enhancement of electrical conductivity," *Solid State Sci.*, vol. 8, no. 1, pp. 7–13, 2006.

[154] P. R. Bueno, M. A. Santos, M. A. Ramírez, R. Tararam, E. Longo, and J. A. Varela, "Relationship between grain-boundary capacitance and bulk shallow donors in SnO_2 polycrystalline semiconductor," *Phys. Status Solidi Appl. Mater. Sci.*, vol. 205, no. 7, pp. 1694–1698, 2008.

[155] T. K. Gupta and W. G. Carlson, "A grain-boundary defect model for instability/stability of a ZnO varistor," *J. Mater. Sci.*, vol. 20, no. 10, pp. 3487–3500, 1985.

[156] S. A. Pianaro, P. R. Bueno, E. Longo, and J. A. Varela, "Microstructure and electric properties of a SnO_2 based varistor," *Ceram. Int.*, vol. 25, no. 1, pp. 1–6, 1999.

[157] B. C. Kim, J. I. Jung, J. H. Lee, and J. J. Kim, "Precipitate concentration of Co_2SnO_4 in CoO-doped SnO_2 ceramics at different oxygen chemical potentials," *Solid State Ion.*, vol. 144, no. 3–4, pp. 321–327, 2001.

[158] A. C. Antunes, S. R. M. Antunes, A. J. Zara, S. A. Pianaro, E. Longo, and J. A. Varela, "Effect of Fe_2O_3 doping on the electrical properties of a SnO_2 based varistor," *J. Mater. Sci.*, vol. 37, no. 12, pp. 2407–2411, 2002.

[159] J. F. Wang *et al.*, "(Pr, Co, Nb)-doped SnO_2 varistor ceramics," *J. Am. Ceram. Soc.*, vol. 88, no. 2, pp. 331–334, 2005.

[160] S. A. Pianaro, P. R. Bueno, P. Olivi, E. Longo, and J. A. Varela, "Effect of Bi_2O_3 addition on the microstructure and electrical properties of the $SnO_2 \cdot CoO \cdot Nb_2O_5$ varistor system," *J. Mater. Sci. Lett.*, vol. 16, pp. 634–638, 1997.

[161] S. R. Dhage, V. Ravi, and O. B. Yang, "Varistor property of $SnO_2 \cdot CoO \cdot Ta_2O_5$ ceramic modified by barium and strontium," *J. Alloys Compd.*, vol. 466, no. 1–2, pp. 483–487, 2008.

[162] J. Fan, D. Liu, X. Zhang, H. Zhao, Z. Zhang, and Y. Zheng, "The effects of B_2O_3 addition and sintering temperature on the electrical properties of SnO_2 based varistors," *Adv. Mater. Res.*, vol. 621, pp. 35–38, 2013.

[163] C. M. Wang *et al.*, "Effects of Pr_2O_3 on the nonlinear electrical characteristics and dielectric properties of $SnO_2 \cdot Co_2O_3 \cdot Ta_2O_5$ varistor systems," *Solid State Commun.*, vol. 132, no. 3–4, pp. 163–167, 2004.

[164] G. Q. Luo, J. Li, D. M. Zhang, Q. Shen, and L. M. Zhang, "Densification Mechanism of SnO_2 Ceramics Doped with 5.0 mol% MnO_2," *Key Eng. Mater.*, vol. 351, pp. 88–92, 2007.

[165] K. Rajwali and M. H. Fang, "Dielectric and magnetic properties of (Zn, Co) co-doped SnO_2 nanoparticles," *Chinese Phys. B*, vol. 24, no. 12, 2015.

[166] G. B. Kumar and S. Buddhudu, "Optical, thermal and dielectric properties of $Bi_4(TiO_4)_3$ ceramic powders," *Ceram. Int.*, vol. 36, no. 6, pp. 1857–1861, 2010.

[167] O. A. Desouky and K. E. Rady, "Synthesis, structure and dielectric properties of nanocrystalline SnO_2–CoO–Nb_2O_5 varistor doped with Cr_2O_3," *J. Mater. Sci. Mater. Electron.*, vol. 28, no. 5, pp. 4197–4203, 2017.

[168] Keysight Technologies, "Impedance Measurement Handbook A guide to measurement technology and techniques," in *A guide to measurement technology and techniques*, 5th Edit., 2009, pp. 1–15.

[169] G. Z. Zang *et al.*, "Varistor and dielectric properties of Cr_2O_3 doped SnO_2-Zn_2SnO_4 composite ceramics," *Curr. Appl. Phys.*, vol. 14, no. 12, pp. 1682–1686, 2014.

[170] S. Tominc, A. Rečnik, S. Bernik, M. Mazaj, and N. Daneu, "Charge compensation and electrical characteristics of Ta_2O_5–doped SnO_2–CoO ceramics," *J. Eur. Ceram. Soc.*, vol. 40, no. 2, 2020.

[171] N. Daneu, A. Rečnik, and S. Bernik, "Grain growth control in Sb_2O_3-doped zinc oxide," *J. Am. Ceram. Soc.*, vol. 86, no. 8, pp. 1379–1384, 2003.

[172] N. Daneu, A. Rečnik, and S. Bernik, "Grain-growth phenomena in ZnO ceramics in the presence of inversion boundaries," *J. Am. Ceram. Soc.*, vol. 94, no. 5, pp. 1619–1626, 2011.

[173] S. Tominc, A. Rečnik, S. Bernik, M. Mazaj, M. Spreitzer, and N. Daneu, "Microstructure development in (Co,Ta)-doped SnO_2-based ceramics with promising varistor and dielectric properties," *J. Eur. Ceram. Soc.*, vol. 40, no. 15, pp. 5518–5522, 2020.

[174] S. J. Penn *et al.*, "Effect of Porosity and Grain Size on the Microwave Dielectric Properties of Sintered Alumina," *J. Am. Ceram. Soc.*, vol. 80, no. 7, pp. 1885–1888, 1997.

Bibliography

Publications Related to the Thesis

Original scientific articles

S. Tominc, A. Rečnik, Z. Samardžija, G. Dražić, M. Podlogar, S. Bernik, N. Daneu, "Twinning and charge compensation in Nb_2O_5-doped SnO_2-CoO ceramics exhibiting promising varistor characteristics", *Ceramics International*, vol. 44, no. 2, pp. 1603-1613, 2018, doi: 10.1016/j.ceramint.2017.10.081.

S. Tominc, A. Rečnik, S. Bernik, M. Mazaj, N. Daneu, "Charge compensation and electrical characteristics of Ta_2O_5-doped SnO_2-CoO ceramics", *Journal of European Ceramic Society*, vol. 40, no. 2, pp. 355-361, 2020, doi: 10.1016/j.jeurceramsoc.2019.09.028.

S. Tominc, A. Rečnik, S. Bernik, M. Mazaj, M. Spreitzer, N. Daneu, "Microstructure development in (Co,Ta)-doped SnO2-based ceramics with promising varistor and dielectric properties", *Journal of European Ceramic Society*, vol. 40, no. 15, pp. 5518-5522, doi: 10.1016/j.jeurceramsoc.2020.03.062.

Published scientific conference contribution abstracts (2014 – 2021)

N. Daneu, S. Tominc, G. Dražić, F. Ruiz-Zepeda, M. Kawasaki, A. Rečnik, et al. "STEM study of (101) twins in natural and synthetic cassiterite," V: *2016 MRS Spring Meeting & Exhibit, March 28-April 1, 2016 Phoenix, Arizona*. Warrendale: Materials Research Society. 2016.

Z. Samardžija, S. Tominc, N. Daneu, A. Rečnik, "EBSD study of twins in SnO_2-cassiterite," V: A. Gajović (ur.). *Book of abstracts*, 13th Multinational Congress on Microscopy, September 24-29, 2017, Rovinj, Croatia. Zagreb: Ruđer Bošković Institute: Croatian Microscopy Society. 2017, pp. 527-528.

S. Tominc, A. Rečnik, Z. Samardžija, G. Dražić, N. Daneu, "Study of microstructure development and (101) twinning in Nb_2O_5/Ta_2O_5 doped SnO_2 ceramics with CoO additions using electron microscopy," V: L. Pirker (ur.), et al. *Knjiga povzetkov*, 3. slovensko posvetovanje mikroskopistov, 16. in 17. maj, Ankaran. 1. izd. Ljubljana: Slovensko društvo za mikroskopijo. 2019, pp. 78.

S. Tominc, A. Rečnik, Z. Samardžija, G. Dražić, M. Podlogar, S. Bernik, N. Daneu, "Microstructure development and twinning in Nb_2O_5-doped SnO_2-CoO ceramics exhibiting promising varistor characteristics," V: *Electroceramics XVI, July 9th-12th, 2018, Hasselt, Belgium: program & abstracts*. Hasselt: Hasselt University. 2018, pp. 264.

S. Tominc, M. Podlogar, G. Dražić, S. Bernik, N. Daneu, A. Rečnik, "Twinning and charge compensation in Nb_2O_5/Ta_2O_5-doped SnO_2−CoO varistor ceramics," V: M. Godec (ur.), et al. *Program and book of abstracts*, 26th International Conference on Materials and Technology, 3-5 October 2018, Portorož, Slovenia. 2018, pp. 130.

S. Tominc, M. Podlogar, A. Rečnik, S. Bernik, N. Daneu, "Characteristics of (Co,Nb)-doped SnO_2 varistor ceramics. V: S. Prpar Mihevc (ur.), M. Prunk (ur.), J. Pungerčar (ur.). *10th Young researchers' day, 31 March, 2016, Ljubljana: program and abstract book*. Ljubljana: Institut Jožef Stefan. 2016, pp. 45.

S. Tominc, N. Daneu, M. Podlogar, S. Bernik, A. Rečnik, "Effect of twin boundaries on the microstructure and electrical properties in (Co, Nb)-doped SnO_2 varistor ceramcs," V: *Electroceramics XV, June 27-28-29, 2015, Limoges, France: program & abstracts*. [S. l.: s. n.]. 2015, pp. 159.

S. Tominc, M. Podlogar, S. Bernik, G. Dražić, N. Daneu, A. Rečnik, "Microstructural and electrical properties in (Co,Nb)-doped SnO_2 varistor ceramics," V: M. Godec (ur.), et al. *Program and book of abstracts*, 24th International Conference on Materials and Technology, 28-30 September 2016, Portorož, Slovenia. Ljubljana: Inštitut za kovinske materiale in tehnologije, 2016, pp. 47.

S. Tominc, N. Daneu, A. Rečnik, "Structural investigations of (101) cassiterite twins from La Paz (Bolivia)," V: N. Kavčič (ur.), et al. *9th Young researchers' day, April 7, 2015, Ljubljana: program and abstract book*. Ljubljana: Institut Jožef Stefan. 2015, pp. 37.

S. Tominc, N. Daneu, A. Rečnik, "The role of twin boundaries in growth of natural and Fe-doped SnO_2 crystals," V: *Abstract book: program & abstract*. [S. l.: s. n.]. 2015. http://www.imem.cnr.it/eccg5/files/book.pdf.

S. Tominc, A. Rečnik, N. Daneu, "Structural investigations of (101) cassiterite twins from La Paz (Bolivia) by transmission electron microscopy," V: *Abstracts*, 12th Multinational Congress on Microscopy, Eger, Hungary, August 23-28, 2015. [S. l.: s. n. 2015], pp. 144-146.

S. Tominc, A. Rečnik, N. Daneu, "Transmission electron microscopy investigations of twin boundaries in cassiterite (SnO_2)," V: A. Šestan (ur.), et al. *Book of abstracts*, 1st Slovene Microscopy Symposium, 18-19 May 2015, Piran, Slovenia. [S. l.: s. n. 2015].

Monographs and Other Completed Works

Undergraduate thesis

S. Tominc, "Imobilizacija holesterol oksidaze na maghemitne nanodelce modificirane s hitozanom," : diplomsko delo univerzitetnega študijskega programa, Maribor: [S. Tominc], 2013. XII, 59 f., ilustr. http://dkum.uni-mb.si/IzpisGradiva.php?id=41881. [COBISS.SI-ID 17478678

Biography

The author of this thesis, Sara Tominc, was born on April 28th, 1989 in Maribor, Slovenia. After grammar school graduate in 2008, she enrolled the Chemical Engineering studies at the Faculty of Chemistry and Chemical Engineering at the University of Maribor, Slovenia. She completed her bachelor studies in September 2013, with the focus on immobilization of enzyme cholesterol oxidase onto maghemite nanoparticles. In October 2014, she enrolled in a doctoral study programme of Nanosciences and Nanotechnologies at the Jožef Stefan International Postgraduate School in Ljubljana, Slovenia. With a growing interest in research work in the field of crystal growth and planar defects in minerals, she became a young researcher at the Department for Nanostructured Materials at the Jožef Stefan Institute in Ljubljana. The main tools for her investigations were transmission and scanning electron microscopy techniques, she was also involved in the Slovenian Society for Microscopy. The main goal of her work was to study the crystal growth and twinning in SnO_2-based varistors ceramics. Based on microstructural studies of ZnO ceramics, where grain growth was successfully controlled by the formation of inversion boundaries, she made an attempt to apply the same principle to the SnO_2 ceramic.